# MAGNETIC BUBBLE DOMAIN AND DOMAIN WALL DYNAMICS IN GRADIENT TRANSLATION

Thesis by

Kochan Ju

In Partial Fulfillment of the Requirements

for the Degree of

Doctor of Philosophy

California Institute of Technology

Pasadena, California

1978

(Submitted May 16, 1978)

# ACKNOWLEDGEMENTS

I would like to express my gratitude and deep appreciation to Professor Humphrey for providing the opportunity to perform this research, for his guidance and assistance throughout the course of this research and his patience in combing through the manuscript. I am very grateful to Professor C. H. Wilts, Dr. T. Kobayashi, Dr. G. J. Zimmer and Dr. O. G. Ramer for their helpful discussions and suggestions during the past few years. I gratefully acknowledge the entire Caltech Magnetic Group for providing an excellent homey working environment. Many thanks to Professor H. Huang for initiating my interests in the domain wall dynamics and to Terry Morris for introducing me to the laboratory work.

Special thanks are extended to Mrs. Vere Snell for typing the text and to Tim Gallagher and Kadri Vural for the proofreading.

Financial support received from International Business Machine Corporation and the California Institute of Technology are gratefully appreciated.

Finally, I thank my wife, Jean, for encouragement, devotion and endurance during my stay at Caltech.

## Abstract

The object of this work is to extend both the experimental and theoretical understanding of domain wall dynamics in magnetic bubble translation. Bubble motion in the presence of a bias field gradient has been investigated in detail, using high-speed sampling microscopy with 10 nanosecond laser pulse illumination. Transient bubble translation was observed and overshoot was confirmed. The stored momentum formulation was expanded. Creep was discovered and a qualitative model was formulated to explain the various phases of the translational motion and the mechanism of momentum storage and release. The model was further confirmed by the transverse distortion phenomenon observed in the high impulse gradient experiment. Equation of motion for magnetic domain walls and Bloch lines are also included.

Table of Contents

Chapter 1 Introduction 1

1.1 Bubble Technology and Devices 1

1.2 Bubble Materials 5

1.2.1 Material Requirements 5

1.2.2 Bubble Materials 7

1.3 Domain, Domain Wall and Bloch-line Statics 9

1.3.1 Domain Statics 9

1.3.2 Domain Wall Shape and Energy 19

1.3.3 Bloch-line Shape and Energy 27

Chapter 2 Bubble Dynamics 34

2.1 Introduction 34

2.1.1 Gyrotropic Spin System 34

2.1.2 Modeling 35

2.1.3 Notation 35

2.1.4 Phenomenological Equations of Motion for Spins 36

2.2 Bubble Dynamics 38

2.2.1 General Approach 38

2.2.2 Landau-Lifshitz-Gilbert Equation in Field Form 40

2.2.3 Force Definition and the Force Density Equation 42

2.2.4 Validity of the Force Density Equation 43

2.2.5 Force Density Equation in $\theta$ and $\psi$ Representation 45

2.2.6 Gyrotropic and Dissipative Forces for Spin Structures 46

2.2.7 Translational Motion of Spin Structures 47

2.2.8 Gyrocoupling Vectors and Dissipative Dyadics for Planar Domain Walls and Bloch-lines 49

2.2.9 One Dimensional Planar Wall Motion 56

2.2.10 Lagrangian Formulation for One-Dimensional Planar Wall 59

2.2.11 Ideal Radial Motion of Bubbles with Vertical Bloch-lines 66

2.2.12 Stored Momentum 68

2.2.13 Inplane Pulse Field on a 1-D Planar Wall 73

2.2.14 Summary 74

Chapter 3 Gradient Translation of Magnetic Bubble Domains 75

3.1 Introduction 75

3.1.1 Gradient Propagation Experiment 75

3.1.2 Deflection Angles and Bubble States 77

3.1.3 Translational Forces 79

3.1.4 Translational Velocity and Remnant Effects 89

3.1.5 High Speed Photography 92

3.2 Experimental Apparatus 93

3.3 Observation of the Vertical Bloch Lines 98

3.3.1 Introduction 98

3.3.2 Experimental Observation 100

3.3.3 Discussion 104

3.4 Gradient Transient, Overshoot and Creep 105

3.4.1 Introduction 105

3.4.2 Experiment 105

3.4.3 Results 107

3.4.4 Discussion 122

3.5 Overshoot and Transverse Expansion in the High Impulse Gradient Translation 135

3.5.1 Introduction 135

3.5.2 Experiment 135

3.5.3 Results and Discussion 137

3.6 Bubble Translation in Ion-implanted Garnets 145

3.6.1 Introduction 145

3.6.2 Samples and Experiment 146

3.6.3 Results and Discussion 146

3.7 Conclusion 156

References 158

# Chapter 1 Introduction

## 1.1 Bubble Technology and Devices

Magnetic bubble technology[1-4] has drawn considerable attention as a potential candidate for future memory devices. This new technology incorporates the advantage of high bit density, non-volatility, low power consumption, moderately high speed, absence of moving mechanical parts and ease of fabrication. Magnetic bubbles are actually small cylindrical magnetic domains in thin film material typically 4 microns in diameter in a film of about the same thickness. The material is magnetized perpendicular to the surface with the magnetization of the bubbles opposite to that of the rest of the film in which they are embedded. Those cylindrical bubble domains are statically stable over a wide range of magnetic field normal to the film. In a device, this bias field is applied by a permanent magnet. Bubbles can move inside the magnetic film at relative high speed, about one to ten million times their diameter per second, in the presence of a small bias field gradient. Bit information, represented by the presence or absence of the magnetic bubble domain, can be propagated by applying a rotating inplane field to magnetize a soft magnetic permalloy overlay structure placed on top of the bubble garnet film[5]. The magnetic poles produced by the permalloy overlay provide the small gradient necessary to control the domain motion. Various bubble propagation patterns such as T bar [5], Y bar [6], X bar, chevron [7], and asymmetric half disc [8], have been used in these field access devices.

An example of a T bar arrangement and domain manipulation is

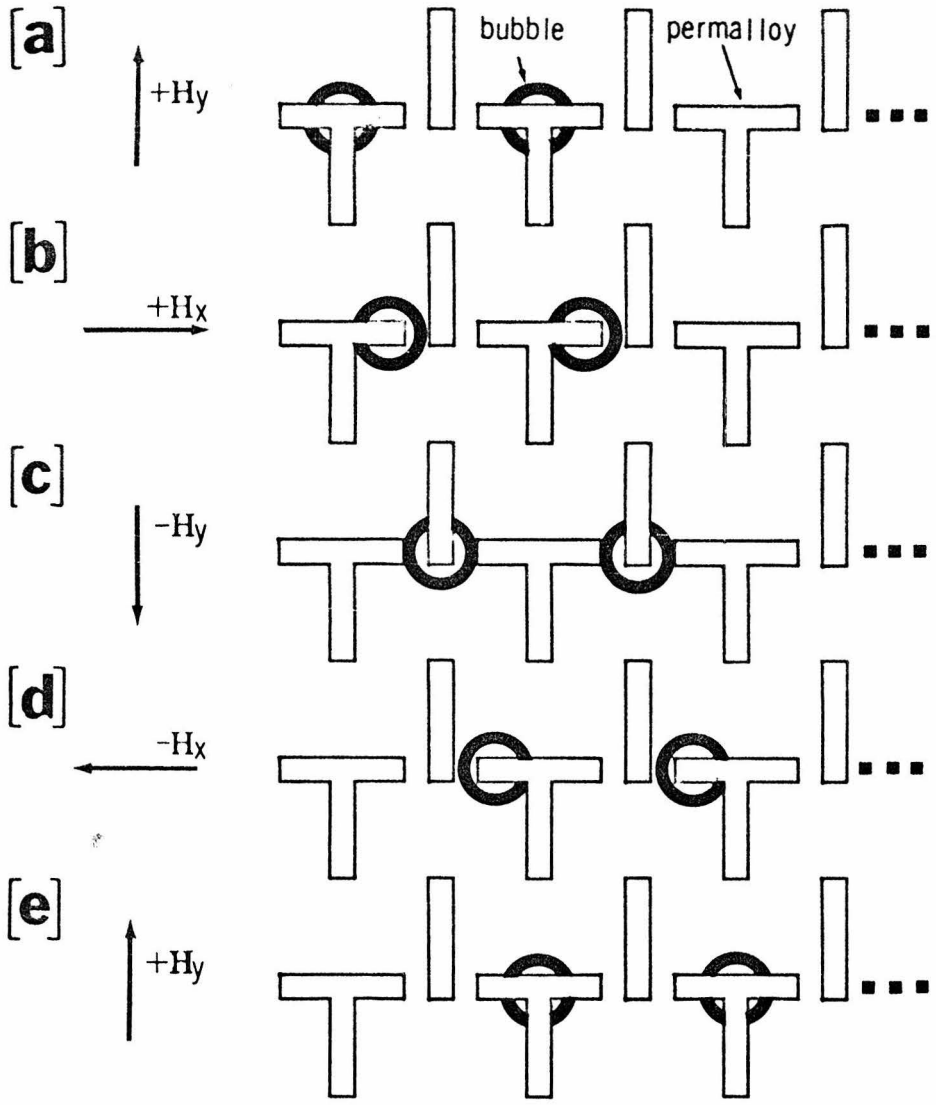


Fig.(1.1) T bar propagation. Cylindrical domains are attracted to + magnetic poles that appear when the inplane field is directed along a long dimension of a T or I bar. As the field rotates clockwise, + pole always appears immediately to the right of the domains, causing them to propagate toward the right. (after Perneski[1.5])

illustrated in Fig. (1.1). Cylindrical bubble domains are assumed to be magnetized downward (in the negative z direction) and the rest of the magnetic film is magnetized up. Bubbles are attracted to the positive magnetic poles that appear when the inplane field is applied along the long dimension of a T or an I bar. As the inplane field rotates clockwise, positive poles always appear immediately to the right of the domains, causing the bit pattern to shift toward the right. Bubbles are actually moved by the local bias field (along the magnetization direction) gradient. A bias field gradient affects the bubble wall differently around the bubble with the result that the bubble is forced to translate. As the magnetic field in the film plane rotates clockwise from y to x direction as is the case from (a) to (b), the permalloy overlay will be magnetized differently. The position of the positive poles, at the top of the T in (a) moves smoothly to the end of the top of the T at (b). The bubble translates, in this case, toward the right and remains underneath the positive poles. As the inplane field rotates further,as in the case (c), the positive poles on the tip of the bar will become strong as those on the T diminish; therefore, a stronger bias field gradient toward the tip of the I bars causes the bubble to move further to the right. As the inplane field rotates by 360°, all bubbles will be shifted to the right by one period. Each TI combination is the cell of a shift register memory. The speed of the bubble in this device is then governed by the frequency of the inplane rotating field. The mobility and the saturation velocity of the bubble directly

limit the maximum operation frequency and, therefore, the data rate of the devices.

The presence or absence of a magnetic bubble in these shift register devices can be detected optically or electronically using the Faraday effect, Hall effect or magneto-resistance effect [9]. The magneto-resistance method, using a permalloy sensor, is the most simple and compatible with the propagation circuit fabrication. The controlled generation of the bubble domains, the write function of the memory, can be achieved by pulsing current through a small hairpin shaped conductor overlay [1] on top of the bubble film. This conductor can be used in conjunction with a disc or rectangular permalloy overlay or a chevron permalloy pattern, depending upon the style of the generator design.

Many binary logic functions of bubbles have been proposed based on the magnetostatic bubble-bubble interaction [2]. These logic functions can again be fabricated using permalloy overlays. The only function to be completely developed at this time is transfer/replicate. This switching ability allows major-minor loop organization [2] and on chip decoding [10], which shortens the access time and the number of interconnections.

At present, at least two bubble memory systems are on the commercial market. One uses bubble chips capable of storing 100 kbit and the other 256 kbit each. Recently, one-mega-bit bubble chips with density of $1.6 \times 10^6$ bits/cm$^2$ have been built and tested success-

fully [11]. The operation temperature of this device is from -25° to 75°C and the data rate is 300 kHz. Today, there is a sizeable worldwide effort, including more than a dozen firms in America, Japan and Europe competing to develop and ready this new technology for an anticipated memory market. High volume bubble memory production is expected to begin in 1980.

Compared to a semiconductor memory device, bubble memory devices are simpler in structure and fabrication; therefore, they must ultimately be lower in production cost. The bubble memory has a higher potential bit density. It is also nonvolatile so that it does not consume power during data storage. Compared to magnetic disc storage, they are faster, more reliable with no moving parts and can be distributed, physically, around the machine. They are expected to compare favorably economically with small discs; however, it will probably be a long time, if ever, before they are more economical than large discs.

## 1.2 Bubble Materials

### 1.2.1 Material Requirements

In a magnetic thin film device, the magnetization normally lies in the plane of the film since this gives a lower demagnetizing energy for the system. In magnetic bubble materials, however, a strong anisotropy normal to the plane causes the material to magnetize normal to the film plane, resulting in cylindrical domains with an

isotropic domain mobility in the film plane. The magnitude of the uniaxial anisotropy normal to the film needed to stabilize the domain is an important material parameter. Stability against coherent rotation of the magnetization into the film plane requires a minimum uniaxial anisotropy of

$$K > 2\pi M_s^2 \tag{1}$$

or in other words,

$$H_k = 2K/M_s > 4\pi M_s \quad , \tag{2}$$

where K is the uniaxial anisotropy constant and $H_k$ is the anisotropy field. The stability against spontaneous nucleation of domains requires the sum of the demagnetizing field and the bias field to be smaller than the anisotropy field [13]. When these two stability conditions are met, reversal only in the form of domain wall motion is expected. Other requirements on the material also exist. Optimum stability of the bubble [13,15] requires that the diameter of the bubble be about

$$d = 2h = (8/\pi)(AK)^{1/2} M_s^{-2} \quad , \tag{3}$$

where A is the exchange constant of the material and h is the thickness of the magnetic film. If smaller bubbles are desired for higher density memories, for example, it requires materials with relatively low exchange constant, low anisotropy and high $4\pi M_s$.

Dynamically, propagation of bubbles at the high speed requires high mobility and low coercivity materials. The mobility of the domain or domain walls, as will be derived later in Chapter 2, is

$$u_b = |\gamma|(A/K)^{1/2}\alpha^{-1} \quad , \tag{4}$$

where $|\gamma|$ is the gyromagnetic ratio and $\alpha$ is the damping parameter of the material. So, high mobility requires relatively high gyromagnetic ratio and low damping materials. As will be shown later, in actual practice, bubble motion is more complicated so that it is not always clear what the materials requirement is for memory operation. Low coercivity requires low defects and good uniformity in the materials.

### 1.2.2 Bubble Materials

Single crystal slices of orthoferrite were first found to have the desired properties for bubble domains [1]. Orthoferrite is a special class of ferrite with a chemical formula of $RFeO_3$ where R represents one or more elements among rare-earth elements and Yttrium. The crystal provides the necessary anisotropy for the magnetization to lie normal to the film. Full memory operation was achieved on orthoferrite with a packing of $6x10^3$ bit/cm$^3$ using 75 μm diameter bubbles. The propagation was done at a bit rate of 147 kHz but the mobility of the orthoferrite, typically 100 m/sec/Oe is sufficiently high to allow a data rate between one to ten MHz. Beside the limit on the film thickness due to the mechanical slicing involved in the fabrication, the material parameters A, K and

$4\pi M_s$ limit the bubble size to a range from a few hundred- to a few tens- of microns.

The necessary control over the bubble material parameters, film quality and the ability to reduce the bubble size to the range from a few microns to a few tenths of a micron came with the introduction of liquid phase epitaxial growth of bubble garnet films[16]. Garnet has a chemical formula of $R_3Fe_5O_{12}$ where R represents one or more elements among rare-earth elements and Yttrium.

Magnetic [14] ordered amorphous films have also been shown to support bubble domains [17]. Films formed by sputtering can be prepared on a great variety of substrates, including glass, polycrystalline metals, silicon and flexible polymers, while preserving their magnetic properties. A completely integrated memory can be imagined in which both the bubble memory and associated semiconductor circuitry would be on the same chip. The material parameters of the amorphous system allow bubbles as small as .1 micron in diameter. Operation of all functions in a 8 kbit bubble device with $1.6 \times 10^6 bit/cm^2$ has been demonstrated on an amorphous film. One MHz operation has been used [18] and the domain velocity data indicate that frequencies in excess of 10 MHz are possible. However, the coercivity in amorphous films is typically five times higher than that of garnet film. Temperature sensitivity,

dielectric breakdown and corrosion are the key factors that limit the device performance of the amorphous materials [19]. It is clear that, for the immediate future, the potentiality of the amorphous materials will not be realized.

## 1.3 Domain, Domain Wall and Bloch-line Statics

### 1.3.1 Domain Statics

Magnetic domain theory was first proposed by Weiss [20] in 1907. He assumed that a ferromagnetic material contains a large number of small regions, called domains, within which the magnetization $\vec{M}$ is a constant in both magnitude and direction. Change in overall magnetization could occur at a relatively low magnetic field through an increase of the volume of those domains whose magnetization direction is closer to the field direction at the expense of the other domains. In bubble garnet material, with a strong uniaxial anisotropy, domains consist of regions of material magnetized in either direction perpendicular to the plane of the film.

The bubble garnet materials are optically transparent, allowing the domains to be observed utilizing the Faraday Effect. The plane of polarization of linearly polarized incident light rotates as the light propagates through the magnetic medium with the rotation dependent on the magnetization $\vec{M}$ and the gyrotropic property of the material. For a typical bubble film thickness, Faraday rotation from 0.25 to 0.75 degree is obtained. Bubble domain observation is usually done by passing light through the sample with the incident

light normal to the plane of the film. Under these conditions, the optical rotation from one domain to the next is twice the Faraday rotation. This rotation is sufficient for domain observation.

Photographs of the Faraday observation of domains in bubble material are shown in Fig.(1.2.) At zero DC bias field, the polarizer analyzer pair is adjusted one way in Fig. (1.2a), the other way in Fig. (1.2c) and exactly crossed in Fig. (1.2b). The black lines in Fig. (1.2b) are caused by diffraction of light by the domain wall. They have a width comparable to the wavelength of the light used. The calculated domain wall width, as will be given in Section 1.3.2, is much smaller, approximately 900 Å. At zero bias field, oppositely magnetized domains are present with about half of the area occupied by each type of domains. As the bias field increases, as shown in Fig. (1.2d), (1.2e) and (1.2f), those domains with the magnetization opposite to the bias field direction contract in size, leaving more volume magnetized in the direction of the field. Short stripe domains finally contract to round domains, called bubbles, in high bias fields. Finally, as the bias field continues to increase, the bubble domains will shrink and eventually collapse, leaving the sample fully magnetized in the applied direction.

The static properties of the bubble domains can be described, using a wall model [1,15] where the domain wall is represented only by its surface energy density, $\sigma_w$, or surface tension. Coordinate z is assumed to be in the direction normal to the magnetic bubble film, and the bubble is assumed to be magnetized in the -z direction.


Fig.(1.2) Faraday photographs of bubble domains. The static bias field is (a), (b) and (c) 0 Oe, (d) 50 Oe, (e) 80 Oe, and (f) 90 Oe. The polarizer analyzer is set one way (a), exactly crossed (b), and the other way (c-f).

Relative to the uniformly magnetized film, the total energy of this isolated bubble domain consists of the Zeeman, demagnetizing and the domain wall energy:

$$E_T = E_H + E_D + E_W$$

$$= 2M_s H_z \pi r^2 h + E_D + 2\pi r h \sigma_w \quad , \qquad (5),$$

where h is the thickness of the bubble film, and r is the radius of the bubble. The applied field energy or Zeeman energy, $E_H$, equals $2M_s H_z$ times the volume of the bubble, $\pi r^2 h$. The wall energy is simply a surface energy density, $\sigma_w$, times the total wall area $2\pi rh$. Unfortunately the demagnetizing energy $E_D$ is more difficult to evaluate.

The demagnetizing energy of the bubble relative to the uniformly magnetized state (magnetized in the direction of the bias field) can be calculated as the work done to the system as the bubble radius grows from zero to r

$$E_D = \int_0^h \int_0^r 2M_s H_{Dz}(r',z)\, 2\pi r' dr'\, dz \quad , \qquad (6),$$

where $2M_s$ is the change in magnetization as the wall passes by. Expression $H_{Dz}(r',z)$ represents the local z component of the demagnetizing field on the bubble wall when bubble is of the size r'. The variation in demagnetizing energy for an infinitesimal change of bubble radius can, therefore, be written

$$\delta E_D = 4\pi M_s r \delta r \int_0^h H_{Dz} dz \quad . \tag{7a}$$

The derivative of the demagnetizing energy with respect to radius is

$$dE_D/dr = 4\pi M_s r h \, \overline{H}_D \quad , \tag{7b}$$

where $\overline{H}_D$ is the average z component of the demagnetizing field in the wall

$$\overline{H}_D = (1/h) \int_0^h H_{Dz} dz \quad . \tag{7c}$$

This average z direction demagnetizing field at the wall, $\overline{H}_D$, has been calculated analytically by Bobeck [1] and Thiele [14] to be

$$\overline{H}_D = +8M_s \left\{ 2r/h - [1 + (2r/h)^2]^{1/2} E \left[ (1+(\frac{h}{2r})^2)^{-1/2} \right] \right\} \tag{8}$$

where E is the complete elliptical integral of the second kind. A simpler approximation for $H_D$ has been derived by Callen et al [21],

$$\overline{H}_D = -4\pi M_s / \, 1+3r/2h \quad . \tag{9}$$

The maximum error of this approximation is only a few percent for $0<r<10h$. The demagnetizing energy of the bubble, $E_D$, can then be calculated by integrating Equation (7) over r

$$E_D = -(4\pi M_s)^2 h^3 \{2r/3h - (4/9)\ln[1+3r/2h]\} \quad . \quad . \quad (10)$$

The integration constant in $E_D$ vanishes since for r=0 it is a uniformly magnetized state that serves as the energy reference. With Equation (10) and characteristic length $\ell$ as defined by

$$\ell = \sigma_w / 4\pi M_s^2 \quad , \quad (11)$$

the total energy of the bubble from Equation (5), can be rewritten as

$$E_T = 8\pi^2 M_s^2 h^3 \{(H_z/4\pi M_s)(r/h)^2 - (4r/3h)$$

$$+ (8/9)\ln(1 + 3r/2h) + (\ell/h)(r/h)\} \quad . \quad (12)$$

Domain size and stability for a strictly circular bubble are characterized by evaluating the first and the second order coefficient in the power series expansion of the total energy with respect to r. It is

$$\Delta E_T = (4\pi M_s)^2 h [r(H_z/4\pi M_s) - r(1+3r/2h)^{-1} + \ell/2]\Delta r$$

$$+ 8\pi^2 M_s^2 h [(H_z/4\pi M_s) - (1+3r/2h)^{-2}](\Delta r)^2$$

$$+ 8\pi^2 M_s^2 (1 + 3r/2h)^{-3} (\Delta r)^3 \quad . \quad (13)$$

The first order coefficient in Equation (13) is the sum of the forces due to the Zeeman energy, domain wall energy and demagnetizing energy of the bubble. The Zeeman force and the domain wall force are always in the sense to reduce the bubble radius while the demagnetizing force is always in the sense to expand the bubble. Equilibrium in bubble size is reached where these forces are balanced, that is, when the 1st order coefficient in Equation (13) vanishes.

$$r(H_z/4\pi M_s) - r/(1+3r/2h) + \ell/2 = 0 \quad . \tag{14}$$

The analytic solution for this force free radius is

$$r_{\pm} = (h/3H' - \ell/4H' - h/3)$$

$$\pm ((h/3H' - \ell/4H' - h/3)^2 - \ell h/3H')^{\frac{1}{2}} \quad , \tag{15}$$

where $H' = H_z/4\pi M_s$ . (16)

The two force free solutions $r_+$ and $r_-$ given in Equation (15) cannot be both stable and correspond to energy minima, since they are the two consecutive roots of zero slope of the energy expression. Reviewing Equation (13), the first order coefficient is positive for both $r \simeq 0$ and $r \simeq \infty$, which implies that the stable solution, if it exists, should be $r_+$, the larger one of the two. Is $r_+$ always a stable solution when Equation (14) has two distinct roots? The positive sign of the first order coefficient in Equation (13) at $r=0$ and $r=\infty$ implies only two possibilities: (1) that the smaller root is a local energy maximum and the second root is a local minimum, or (2) that both roots are inflection points. The second order coefficient in Equation (13) increases monotonically with r, which means the second derivative of the energy will not have two zeros. This is in contradiction to the case of two inflection points, so, it is concluded that as long as the force equation, Equation (13), has two distinct roots, $r_+$, given by Equation (15) will be the stable minimum energy radius and $r_-$ will correspond to a local energy maximum.

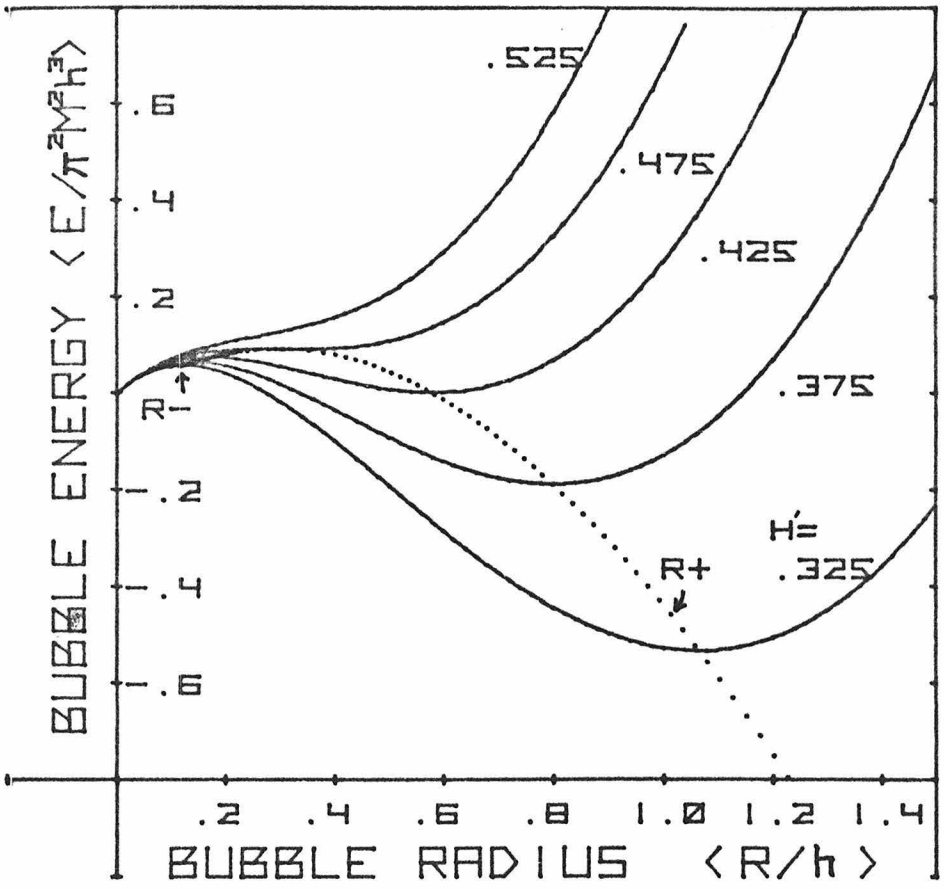


Fig.(1.3) Variation of total bubble domain energy with radius and bias field. Dotted curve showing the energy minimum and maximum at various bias field. Parameter $\ell/h$ in this case is equal to .128.

As $r_+$ and $r_-$ coincide, a double root case for Equation (14), the second order energy derivative will also vanish at that radius. The third order energy derivative, as can be seen from Equation (13), is always positive. This fact implies that this double root in r, where the first and the second energy derivatives vanishes, is an inflection and that the bubble is not stable energetically, so it will collapse spontaneously. The bias field required as well as the solution r for this minimum bubble collapse field can be calculated by setting both the first and second order coefficients of Equation (13) equal to zero. The result is

$$H_{col} = 4\pi M_s(1-(3\ell/4h)^{\frac{1}{2}})^2 \quad . \tag{17}$$

$$r_{col} = h/((3h/\ell)^{\frac{1}{2}} - 3/2) \quad . \tag{18}$$

Subscript "col" stands for collapse, since $H_{col}$ is the maximum bias field in which the bubble is stable.

A plot of the total domain energy, as described in Equation (12), is shown in Fig. (1.3) with bias field as a parameter. A trace of the corresponding energy for the force free bubble radius is shown by the dashed line. For any given bias field below $H_{col}$, which is $.476(4\pi M)$ in this case, bubbles are stable against perturbation in size as long as the perturbed radius is larger than the $r_-$ at that bias field. The bubble will recover to $r_+$ by itself. If the radius is perturbed to be smaller than $r_-$, the bubble will collapse spontaneously.

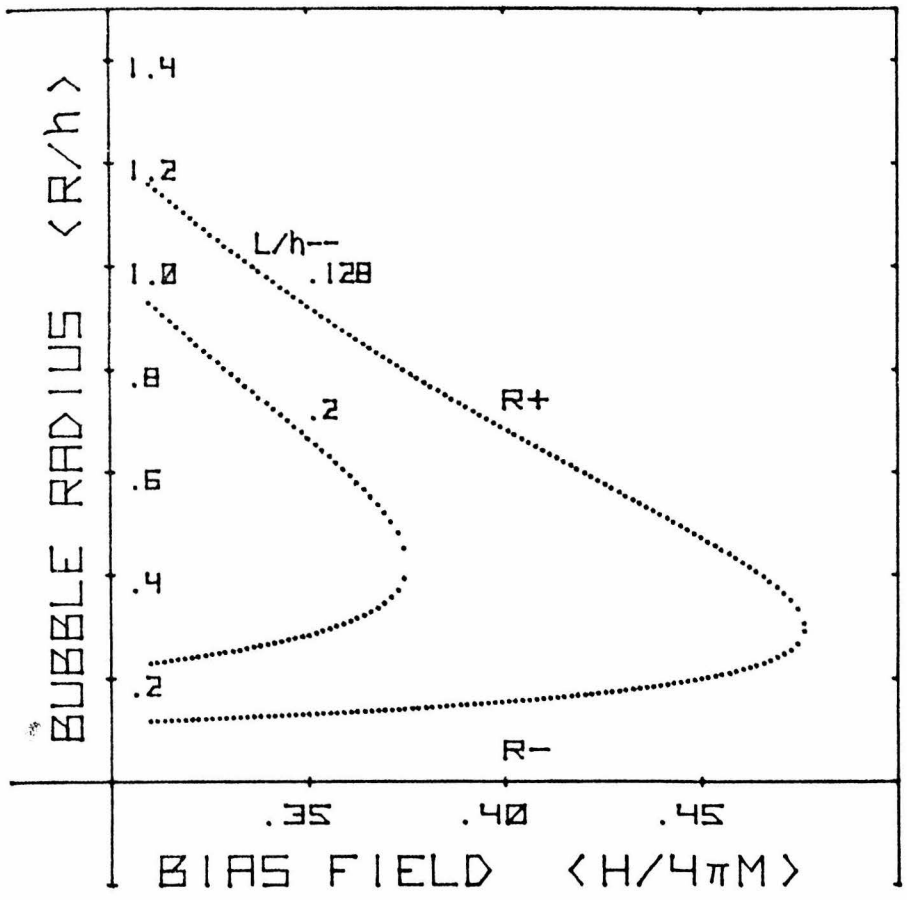


Fig.(1.4) Force free bubble radius as a function of bias field for $\ell/h$ = .128 and .2.

The force free bubble radius as a function of the bias magnetic field, Equation (15), is shown in Fig. (1.4). The normalized characteristic length, $\ell/h$, is used as a parameter. As the bias field increases, the stable equilibrium radius decreases monotonically until the bias field reaches $H_{col}$. It can be seen that bubbles have the large range of stability against bias field fluctuations necessary for devices. Material parameters $\ell$ and $4\pi M_s$ can be determined using static domain theory. The thickness of the film, h, can be measured optically. The static bubble collapse field and the stable bubble radius at various bias fields, given by Equation (17) and Equation (15), can be used to determine $4\pi M_s$ and $\ell$. The film thickness measurement, done optically, normally has an error of about 10%. The collapse field and radius can usually be measured with a scatter of .3% and 4%, respectively. For accurate material characterization, numerical calculations based on the exact formula, Equation (8), instead of the approximate one, Equation (9), is used. The difference between the results, using the two equations, is about 3%. Other static theories for the isolated or periodic stripe domains are also available [1,22,23] for characterizing these static material parameters.

### 1.3.2 Domain Wall Shape and Energy

The energy and the structure of domain walls will be discussed in this section. The surface energy density, which directly relates to the surface tension of the domain, is important in determining

the dynamic characteristics of the wall. These characterisitics, then, directly affect the rate of the magnetic reversal as well as the propagation speed of the free bubble. Both the statically stable and the nonstable solution for the wall structure will be discussed. The latter can exist dynamically in the presence of additional dynamic torques.

Consider a planar wall structure with magnetization described by its polar angle $\theta$ and azimuthal angle $\psi$, as in Fig. (1.5). easy axis of the anisotropy is at $\theta=0$ and is normal to the magnetic film. The magnetization is assumed to be only a function of y such that polar angle $\theta$ varies from $-\pi$ to 0 as y changes from $-\infty$ to $\infty$. The energy density of this one-dimensional planar wall located in the x,z plane consists of exchange, anisotropy and demagnetizing energy. Relative to the uniformly magnetized sample, the energy density can be written as

$$e_T = e_j + e_k + e_m \quad , \tag{19}$$

$$e_j = A[(\partial\theta/\partial y)^2 + \sin^2\theta(\partial\psi/\partial y)^2] \quad , \tag{19a}$$

$$e_k = -K\cos^2\theta + K = K\sin^2\theta \quad , \tag{19b}$$

and

$$e_m = -\tfrac{1}{2}(-4\pi M_s \sin\theta\sin\psi)(M_s\sin\theta\sin\psi)$$

$$= 2\pi M_s^2 \sin^2\theta\sin^2\psi \tag{19c}$$

where A is the exchange constant and K is the uniaxial anisotropy constant.

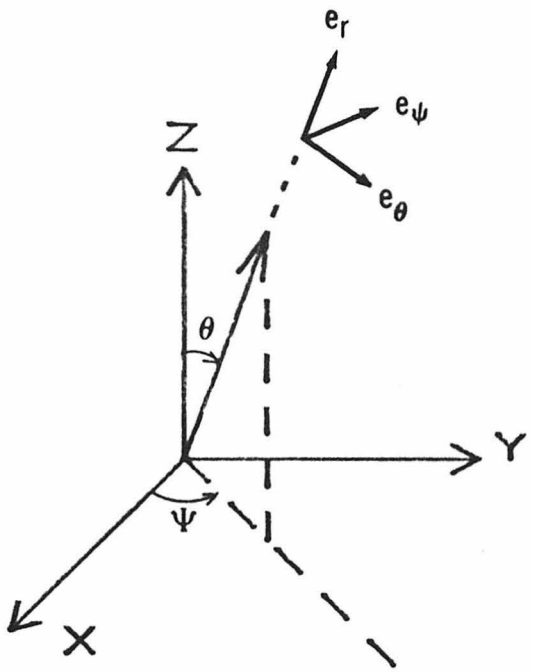


Fig.(1.5) Coordinate axes

The demagnetizing energy density here in this one-dimensional planar wall case with material extending to infinity can be expressed explicitly with local spin orientations. Maxwell's equation, $\nabla \cdot B=0$, states

$$\partial(H_y + 4\pi M_y)/\partial y = 0 \tag{20}$$

so that $-4\pi M_y$ and $H_y$ can differ at most by a constant throughout the wall. The boundary condition outside the wall is

$$H_y = M_y = 0 \tag{21}$$

for the perfectly magnetized material with no external inplane fields. Equation (20) with Equation (21) implies the equality

$$H_y = -4\pi M_y = -4\pi M_s \sin\theta \sin\psi \quad , \tag{22}$$

which was used in obtaining Equation (19c).

The wall structure is determined by finding the total wall energy which is given as

$$E_T = \int e_T \, dx \, dy \, dz \quad . \tag{23}$$

and then minimizing it by taking a functional variation with respect to $\theta$ and $\psi$, and setting it equal to zero

$$2A\partial^2\theta/\partial y^2 - [K + 2\pi M_s^2 \sin^2\psi + A(\partial\psi/\partial y)^2]\sin 2\theta = 0 \tag{24a}$$

$$2A\sin^2\theta(\partial^2\psi/\partial y^2) + 2A\sin 2\theta(\partial\psi/\partial y)(\partial\theta/\partial y) - 2\pi M_s^2 \sin^2\theta \sin 2\psi = 0 \tag{24b}$$

These are simultaneous nonlinear differential equations with $A(\partial\psi/\partial y)^2$ and $2A\sin 2\theta(\partial\psi/\partial y)(\partial\theta/\partial y)$, the two cross coupling terms. General analytic solutions are difficult to obtain except in the special case of a slow variation function of y, such that the two equations can be decoupled.

Fortunately, two self-consistent solutions can be obtained by assuming that $\psi$ is a constant so the crossed coupling terms in Equation (24) vanish. These two solutions are the Bloch wall case for $\psi=0$ or $\pi$ and the Neel wall case for $\psi=\pm\pi/2$. The wall shape obtained from Equation (24a) is

$$\cos\theta = \tanh(\pi y/\ell_w) \tag{25a}$$

with $$\ell_w = \pi(A/K)^{\frac{1}{2}} \equiv \ell_{wo} \tag{25b}$$

for the Bloch wall case and

$$\ell_w = \pi[A/(K+2\pi M_s^2)]^{\frac{1}{2}} \tag{25c}$$

for the Neel wall case. It can be shown from Equation (19) that the Bloch wall structure corresponds to an energy minimum in both $\theta$ and $\psi$, therefore, a stable solution. The Neel wall corresponds to a metastable solution which is a minimum energy state in terms of the $\theta$ structure but an energy maximum in $\psi$.

Another shape that will be of interest is the dynamic steady state case [22] for a constant azimuthal angle. In this case $A(\partial\psi/\partial y)^2$ in Equation (24a) vanishes. In this dynamic

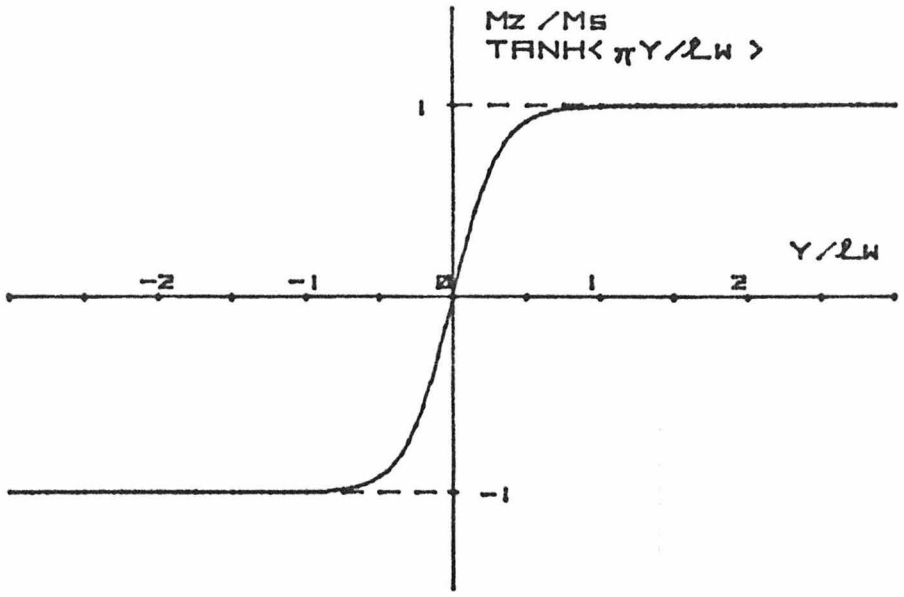


Fig.(1.6) Domain wall structure

case, due to the presence of the kinetic energy which will be explained later, Equation (24b) need not be satisfied. The resultant wall shape is

$$\cos\theta = \tanh(\pi y/\ell_w) \tag{26a}$$

with $$\ell_w(\psi) = \pi\left[A/(K+2\pi M_s^2 \sin^2\psi)\right]^{\frac{1}{2}}$$

$$= \ell_{wo}(1+\sin^2\psi/Q)^{-\frac{1}{2}} \quad , \tag{26b}$$

where Q is defined as

$$Q = K/2\pi M_s^2 = H_k/4\pi M_s \quad . \tag{26c}$$

The Bloch wall and the Neel wall are, of course, special cases of Equation (26), as can be seen by comparing it with Equation (25). The wall width change between the Neel and Bloch walls depends on the relative magnitude of the anisotropy compared to the magnetization. A wall width change of about 11% for Q=3 and 3% for Q=16 is predicted. The typical Q value for the sample used in the later experiment is 16. The domain wall shape, given in Equation (25a) and Equation (26a), is plotted in Fig. (1.6). As can be seen, the wall has a well defined width of $\ell_w$ where most of the change in magnetization occurs.

The wall energy per unit area can be calculated based on Equation (19) and (26)

$$\sigma_w(\psi) = \int_{-\infty}^{\infty} \{A\,\mathrm{sech}^2(\pi y/\ell_w)(\pi/\ell_w)^2 + K\,\mathrm{sech}^2(\pi y/\ell_w) + 2\pi M_s^2[1-\tanh^2(\pi y/\ell_w)]\sin^2\psi\}\, dy$$

$$= 2A\pi/\ell_w + 2K\ell_w/\pi + 4\pi M_s^2 \sin^2\psi\,\ell_w/\pi$$

$$= 4[A(K+2\pi M_s^2\sin^2\psi)]^{\frac{1}{2}} \quad . \tag{27}$$

Compared to the Bloch wall energy, $4(A\cdot K)^{\frac{1}{2}}$ per unit wall area, Neel wall energy is larger by 15% for Q=3 and by 5% for Q=16.

The wall energy density, Equation (27), if expressed in the power series of 1/Q is

$$\sigma_w(\psi) = 4(AK)^{\frac{1}{2}}(1+\sin^2\psi/2Q-\sin^4\psi/8Q^2+\dots)$$

$$= \sigma_w(0) + 4\pi M_s^2 \sin^2\psi(\ell_{wo}/\pi) - \dots \tag{28}$$

Notice that the first term is the Bloch wall energy and the second term is the demagnetizing energy of the wall assuming a Bloch wall width, since

$$\int_{-\infty}^{\infty} 2\pi M_s^2 \sin^2\psi\sin^2\theta\, dy = \int_{\infty}^{\infty} 2\pi M_s^2 \sin^2\psi\,\mathrm{sech}^2(\pi y/\ell_{wo})\, dy$$

$$= 4\pi M_s^2 \sin^2\psi(\ell_{wo}/\pi) \quad . \tag{29}$$

So, if only the first two terms of the power series are chosen from Equation (28), it is the equivalent of having a first order perturbation by adding the demagnetizing energy while assuming the wall width is unchanged. This first order perturbation result agrees

quite well with the analytic one with an error of 8.7% for Q=3 and 1.6% for Q=16. The perturbation approach is very useful in more complicated practical problems where analytic solutions are difficult to find.

### 1.3.3 Bloch-line Shape and Energy

A Bloch line [23,24,25] is defined as the transition region between sections of a Bloch wall of opposite chirality, i.e., $\psi=0$ or $\psi=\pi$. It separates wall sections in a way similar to the way a wall separates domains. The Bloch line is modeled as a $180^{o}$ wall twist. The domain wall shape is governed by the anisotropy and exchange energy of the spins while the Bloch-line shape is governed by the demagnetizing energy and the exchange energy. In the film used, the anisotropy field is more than an order of magnitude higher than $4\pi M_s$. The presence of the Bloch line, therefore, should not deform the wall structure very much. However, in a low Q material, where the anisotropy is not as dominant, a complicated two-dimensional wall structure is expected.

Consider a planar wall in the x,z plane with the wall normal in y direction and a Bloch line centered on the z axis. The azimuthal angle of the spin in the center of the wall is assumed to precess from $-\pi$ to 0 as x changes from $-\infty$ to $\infty$, as shown in Fig. (1.7). The spin structure which describes the wall with a Bloch line is generally two-dimensional. The energy of the spin structure can be written similar to Equation (19) as

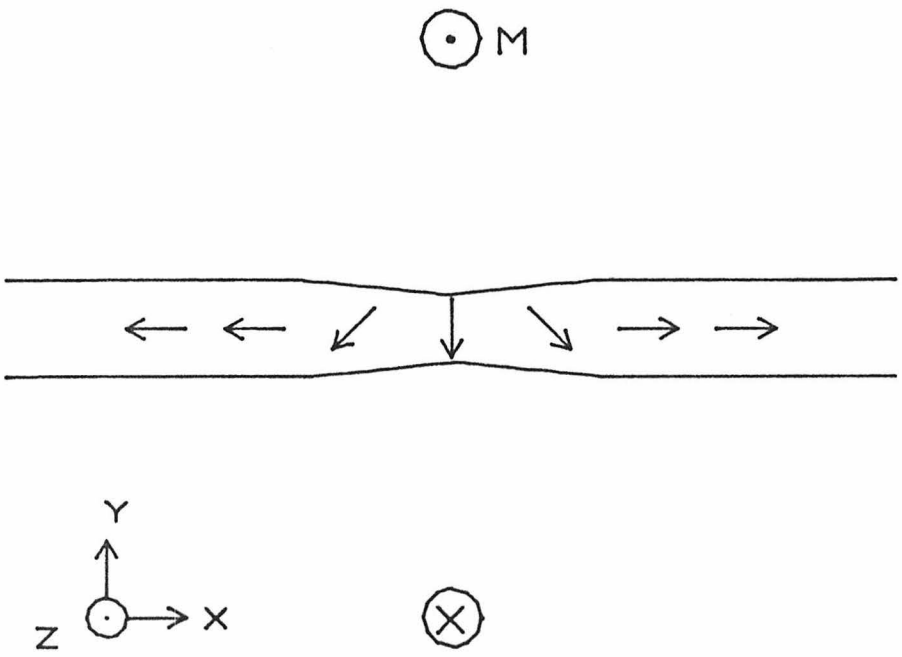


Fig.(1.7) Bloch line configuration

$$E_T = \int (e_J + e_k + e_m)\, dy\, dx\, dz \tag{30}$$

and $$e_j = A((\partial\theta/\partial y)^2+(\partial\theta/\partial x)^2+\sin^2\theta((\partial\psi/\partial y)^2+(\partial\psi/\partial x)^2)) \tag{31a}$$

$$e_k = K\sin^2\theta \tag{31b}$$

$$e_m = 2\pi M_s^2 \sin^2\theta\sin^2\psi \quad . \tag{31c}$$

This approximate expression for demagnetizing energy $e_m$ is useful only for the case where the Bloch-line width is much wider than the wall width.

The equations for the minimum energy spin structure are obtained by setting the functional variation of the total energy to zero. The following equations result

$$2A(\partial^2\theta/\partial y^2+\partial^2\theta/\partial x^2)-\left[K+2\pi M_s^2\sin^2\psi+A[(\partial\psi/\partial y)^2 + (\partial\psi/\partial x)^2]\right]\sin2\theta = 0 \tag{32a}$$

$$2A\sin^2\theta(\partial^2\psi/\partial y^2 +\partial^2\psi/\partial x^2)+2A\sin2\theta[(\partial\psi/\partial y)(\partial\theta/\partial y) + (\partial\psi/\partial x)(\partial\theta/\partial x)]-2\pi M_s^2\sin^2\theta\sin2\psi =0 \quad . \tag{32b}$$

The general solution for Equation (32) is very difficult to obtain. An iterative method can be used to obtain a self-consistent appropriate solution suitable for high Q samples. In the first round of the iteration, $\theta$ is assumed to be a function of y only and $\psi$ is a function of x only. Equation (32) can then be simplified to

$$2A(\partial^2\theta/\partial y^2)-(K+2\pi M_s^2\sin^2\psi+A(\partial\psi/\partial x)^2)\sin 2\theta = 0 \qquad (33a)$$

$$2A\sin^2\theta(\partial^2\psi/\partial x^2)-2\pi M_s^2\sin^2\theta\sin 2\psi = 0 \quad . \qquad (33b)$$

Matching the boundary conditions for $\theta$ and $\psi$ results in

$$\psi = \cos^{-1}\tanh(\pi x/\ell_{\ell o}) \quad , \qquad (34a)$$

and $$\theta = \cos^{-1}\tanh(\pi y/\ell_w) \quad , \qquad (34b)$$

where $$\ell_{\ell o} = \pi(A/2\pi M_s^2)^{\frac{1}{2}} = \ell_{wo}Q^{\frac{1}{2}} \qquad (34c)$$

and $$\ell_w = \pi\{A/[K+2\pi M_s^2\sin^2\psi+A(\partial\psi/\partial x)^2]\}^{1/2}$$

$$= \pi[A/(K+4\pi M_s^2\sin^2\psi)]^{1/2}$$

$$= \ell_{wo}(1+2\sin^2\psi/Q)^{-\frac{1}{2}} \quad . \qquad (34d)$$

In deriving Equation (34d), equalities,

$$\partial\psi/\partial x = -(\pi/\ell_{\ell o})\sin\psi \qquad (35a)$$

and $$A(\partial\psi/\partial x)^2 = A(\pi/\ell_{lo})^2\sin^2\psi = 2\pi M_s^2\sin^2\psi \quad , \qquad (35b)$$

are used which are obtained directly from Equation (34a) and (34c). Here, $\ell_{\ell o}$ is the Bloch-line width parameter which, as shown in Equation (34c), is a factor of $Q^{\frac{1}{2}}$ larger than the wall width parameter.

As can be seen from Equation (34), $\theta$ is a function of $\ell_w$ and therefore a function of x, which is inconsistent with the previous assumption that $\theta$ is a function of y only. The x dependence of $\theta$ can be included in the second round of the iteration by adding a term of $2A\sin 2\theta(\partial\psi/\partial x)(\partial\theta/\partial x)$ into

Equation (33b), i.e.,

$$2A\sin^2\theta\,\frac{\partial^2\psi}{\partial x^2} + 2A\sin 2\theta(\partial\psi/\partial x)(\partial\theta/\partial x) - 2\pi M_s^2\sin^2\theta$$

$$\sin 2\psi = 0 \quad . \tag{36}$$

The truncation error of the first iteration can be estimated by evaluating the truncation term $2A\sin2\theta(\partial\psi/\partial x)(\partial\theta/\partial x)$, using the results of Equation (34). Calculation from Equation (34) results

$$\partial\ell_w/\partial x = \ell_{wo}(-\tfrac{1}{2})(1+2\sin^2\psi/Q)^{-3/2}(2\sin2\psi/Q)(\partial\psi/\partial x)$$

$$= \pi(\ell_{wo}/\ell_{\ell o})(\sin\psi\sin2\psi/Q)\,(1+2\sin^2\psi/Q)^{3/2} \tag{37a}$$

$$\partial\theta/\partial x = \sin\theta(\pi y/\ell_w^2)(\partial\ell_w/\partial x)$$

$$= \sin\theta\sin\psi\sin2\psi(\pi y/\ell_{wo})(\pi/\ell_{\ell o})\cdot Q^{-1}\cdot(1+2\sin^2\psi/Q)^{1/2} \tag{37b}$$

and the truncation error

$$2A\sin2\theta(\partial\psi/\partial x)(\partial\theta/\partial x) = -2A(\pi/\ell_{\ell o})^2\sin\theta\sin2\theta\sin^2\psi\sin2\psi$$

$$(\pi y/\ell_{wo})\,(Q(1+2\sin^2\psi/Q)^{\frac{1}{2}})^{-1}$$

$$= -(4\pi M_s^2/Q)\sin\theta\sin2\theta(\pi y/\ell_{wo})\sin^2\psi\sin2\psi/(1+2\sin^2\psi/Q)^{\frac{1}{2}} \tag{38}$$

Notice the presence of the factor 1/Q in the truncation error which means the error goes to zero as Q tends to infinity. In other words, Equation (34) is an approximate solution for high Q materials.

The expression $(\pi y/\ell_w)\sin\theta\sin2\theta$ is zero for y=0, reaches a maximum at $y=1.01\ell_{wo}/\pi$, and then converges to zero as y increases further.

The truncation term, $2A\sin2\theta(\partial\psi/\partial x)(\partial\theta/\partial x)$, in general, is a factor of $2\sin^2\psi/Q$ times smaller than the two other terms in Equation (36), except in the case where $\pi y/\ell_{wo}>>1$. For this case, all three terms in Equation (36) converge to zero exponentially. For Q>>1, the correction term in the second iteration is negligible and the first iteration gives a good approximation for a Bloch line. For Q<2, the second iteration will result in a function of both x and y, which again means other truncation terms like $A(\partial\psi/\partial y)^2$, $2A\sin^2\theta(\partial^2\psi/\partial y^2)$ and $2A\sin2\theta(\partial\psi/\partial y)(\partial\theta/\partial y)$ should be taken into account in the higher order iteration. The convergence of the iteration might be slow; however, it can be concluded that the Bloch-line shape in low Q materials will be two-dimensional and cannot be approximated by simply a twist of a planar wall.

The Bloch-line energy is the added wall energy due to the presence of the Bloch line. For high Q materials, it can be calculated by evaluating Equation (30), using the Bloch-line shape in Equation (34) and subtracting the energy in the absence of the Bloch line. The resultant Bloch-line energy per unit line length is

$$E_{BL}/\text{unit length} = \int_{-\infty}^{\infty}\left[\int_{-\infty}^{\infty} A\{(\partial\theta/\partial y)^2+(\partial\theta/\partial x)^2+\sin^2\theta(\partial\psi/\partial x)^2\}\right.$$

$$\left.+K\sin^2\theta+2\pi M_s^2\sin^2\theta\sin^2\psi dy-4(AK)^{1/2}\right]dx$$

$$= \int_{-\infty}^{\infty}\left[2A\pi/\ell_w+2\{K+2\pi M_s^2\sin^2\psi+A(\partial\psi/\partial x)^2\}\ell_w/\pi-4(AK)^{1/2}\right]\,dx$$

$$= 4(AK)^{1/2}\int_{-\infty}^{\infty}(\sin^2\psi/Q - 1/2\sin^4\psi/Q^2 + \ldots)\,dx$$

$$= 8(AK)^{1/2}\ell_{\ell o}/(\pi Q) = \sigma_w(0)(2\ell_{\ell o}/\pi Q) \quad . \qquad (39)$$

Most of the Bloch-line energy is distributed over the wall area of width $\ell_{\ell o}$. The Bloch-line energy is a factor of $2/\pi Q$ times smaller than the energy of the wall occupied by the Bloch line.

# Chapter 2

# Bubble Dynamics

## 2.1 Introduction

### 2.1.1 Gyrotropic Spin System

One of the special characteristics of the magnetic materials is the gyrotropic nature of the magnetic moment; angular momentum is found proportional to the magnetic moment in the material. The ratio of the magnetic moment to the angular momentum is called the magnetomechanic ratio or more often, the gyromagnetic ratio. Strictly speaking, however, the gyromagnetic ratio should be the reciprocal of the magnetomechanic ratio. The gyromagnetic (magnetomechanic) ratio for the orbital electron is e/2mc while the ratio for the intrinsic electron spin is e/mc, where e and m are the charge and the mass of the electron, respectively, and c is the speed of light. The gyromagnetic ratio for magnetic materials, normally denoted by $\gamma$, can be obtained from the Einstein de Haas experiment or the Barnett experiment. Values are found that are very close to the ratio for intrinsic electron spins [1]. This result suggests that the magnetization of ferromagnetic materials originates largely from the electron spins rather than from the orbital moment. This gyrotropic effect is the base for the magnetic resonance experiment and is responsible for the Faraday effect and Kerr effect in the magnetic materials.

### 2.1.2 Modeling

The magnetic spin system can be modeled by a spinor field. The magnetic moment is assumed to be a continuous spatial vector function with its magnitude, denoted by $M_s$, a constant in space and time. The angular momentum of the magnetic spin is $-\vec{M}/|\gamma|$, which is in the direction opposite to the magnetization and has a magnitude of $M_s/|\gamma|$. The magnetic system, the domains and the domain walls, is described by the spatial structures of spin orientation. Inside the domains, the spins are pointed in the same direction due to the strong exchange energy within the material. Across the domain boundary or wall, the exchange interaction requires that the spin change direction smoothly. The system, then, is made of regions of smoothly changing spin structures imbedded in areas of uniformly directed spins. The dynamics of the bubble domains can, therefore, be described by the time evolution of a spin structure in motion.

All domain walls in bubble materials cannot possibly have the same structure. The observed complexities in both the static and the dynamic experiments indicate the existence of structure within the wall. The dynamics of the domain wall as well as the dynamics of Bloch-lines, a class of finer wall structures, will be investigated in this chapter.

### 2.1.3 Notation

To formulate the equation of motion of the spin structure, tensor notation or double vector notation is needed. The latter instead of the

more compact tensor notation will be used because the geometric meaning of the vector operation and the orthogonal properties of the vectors are better known. These vector properties will be very helpful in the later discussions. The two types of vectors will be distinguished by the notation, "→" on the top of the characters for one vector field and "~" underneath the characters for the other. These two vectors represent the same thing except that the vector operators, scalar and cross products, are defined to operate only on the vector denoted by "→".

2.1.4 Phenomenological Equations of Motion for Spins

a) Landau-Lifshitz Equation

The first phenomenological equation to describe the motion of the noninteracting spins was proposed by Landau and Lifshitz [2] in 1935. They proposed that the equation of motion is:

$$\dot{\vec{M}} = -|\gamma|\vec{M}x\vec{H} - (\lambda/M_s^2)\vec{M}x(\vec{M}x\vec{H}) \quad , \qquad (1)$$

where $\vec{M}$ is the magnetization with magnitude $M_s$, $\vec{H}$ is the effective magnetic field acting on $\vec{M}$, $\gamma$ is the gyromagnetic ratio and $\lambda$ is an adjustable scalar quantity called the Landau-Lifshitz damping constant.

Equation (1) reduces to the classical torque equation of a massless top when the damping constant is zero. The change in the angular momentum, which is $-\dot{\vec{M}}/|\gamma|$, equals the torque, $\vec{M}x\vec{H}$, on the spin. Spins, in this case, precess around the $-\vec{H}$ direction but will not align to the applied field. The last term of the Equation (1), which is normally called the damping term, was introduced artifically to give $\vec{M}$ a com-

ponent in the applied field direction. The spin could then ultimately align to the applied field direction. It was well known that the magnetization can be aligned into the direction of an applied external field.

The damping term is constructed in such a way that it preserves the magnitude of the magnetization at all times. As can be seen from Equation (1), $\dot{\vec{M}}$ is orthogonal to $\vec{M}$ which means $d(\vec{M}\cdot\vec{M})/dt=0$. The amount of damping is proportional to the torque on the spin along the magnetic field direction. This form of damping is contrary to common experience from other branches of mechanics where damping is usually proportional to the total velocity.

b) Landau-Lifshitz-Gilbert Equation

A modified phenomenological equation for spins was later proposed by Gilbert [3] in 1955. The equation is commonly called the Landau-Lifshitz-Gilbert equation (LLG equation) or Gilbert equation. Given in torque form it is:

$$\frac{1}{|\gamma|}\dot{\vec{M}} + \vec{M}\times\vec{H} - \frac{\alpha}{|\gamma|M_s}\vec{M}\times\dot{\vec{M}} = 0 \qquad (2)$$

where $\alpha$ is the Gilbert damping constant. The damping now is a function of the overall spin motion. This damping can be described by a Rayleigh dissipation function of $\frac{1}{2}\alpha M^2$, which is similar in form to the dissipation function of a viscous fluid. The scalar product of $\vec{M}$ with Equation (2) yields

$$\vec{M}\cdot\dot{\vec{M}} = 0 \qquad (3a)$$

which shows the LLG equation again preserves $M_s$. For a spatial distribution of spins, the equation

$$\vec{M}\cdot\underset{\sim}{\nabla}\vec{M} = 0 \quad , \tag{3b}$$

where $\underset{\sim}{\nabla}$ is the gradient operator, describes the property that $M_s$ is a constant spatially as well.

To describe the motion of the local spins using the LLG equation, the effective field $\vec{H}$ should include contributions from the external applied field as well as uniaxial anisotropy of the magnetic film and the exchange interaction among the neighboring spins. Since all these energies are reversible, the effective field is named the reversible effective field and denoted by $\vec{H}_r$. As a definition of the effective field, the i-th component of the reversible effective field can be written as

$$H_{ri} = -(\delta\rho_E/\delta M_i) \tag{4}$$

where $\rho_E$ denotes the reversible energy density and $\delta$ denotes the functional variation.

## 2.2 Bubble Dynamics

### 2.2.1 General Approach

In the bubble dynamics, we are dealing with the motion of spin structures instead of local or individual spins. To generalize the LLG equation from an equation of motion for a local spin to an equation of

motion for a spin structure, the coupling between spins must be included. Spins are coupled through the demagnetizing field and the exchange interaction. Either the Lagrangian formulation [4,5,6] or the force formulation [7,8] can be used to include this interaction and formulate the generalization.

In the Lagrangian formulation, the Lagrangian density function and the Rayleigh dissipation function are constructed from the LLG equation. These functions are constructed in such a way that maximizing the Lagrangian density function, using Hamilton's principle [9], will result in equations that are identical to the LLG equation. The Lagrangian function for the spin structure is then obtained by integrating the Lagrangian density function spatially over the structure. The generalized coordinates of the Lagrangian function of the system are the parameters or functions used in describing the spin structure. The equation of motion of the spin structure can then be obtained by maximizing the Lagrangian function with respect to the generalized coordinates again using Hamilton's principle. The coupling of the spins is included by adding the exchange and the demagnetizing energy of the structure into the Lagrangian function. A detailed example of this approach for a simplified one dimensional planar wall case will be given in Section (2.2.9). Unfortunately, most structures of interest result in complicated equations of motion, usually nonlinear coupled partial differential equations that require many approximations to solve.

In the force formulation, an equivalent force density can be derived from the LLG equation. The equivalent forces for the overall

spin structure are obtained by integrating the force densities over the structure. The force integrals for the planar wall or the Bloch-line case can be done easily. The force equation, in general, is only a sufficient condition for the LLG equation and is not equivalent to the LLG equation. Therefore, the force equation does not generally guarantee a unique solution.

Force formulation has the advantage of simplicity, both in concept and in expression. It can be easily applied to cases where additional constraints are imposed on the system such as the steady state motion of the domain wall or bubble, the deflection angle of the bubble in translation or the role of the Bloch-lines in the moving wall. The force formulation is especially useful in determining the internal structure of the wall. It is of help in identifying the cause of the remnant effects observed in the gradient translation experiment. The force formulation will be derived and discussed in detail in this chapter.

2.2.2 Landau-Lifshitz-Gilbert Equation in Field Form

The equivalent field form of the Landau-Lifshitz-Gilbert equation serves as an intermediate step in obtaining the force density equation, although the equivalent field concept itself is often useful. Using the orthogonal relation between $\vec{M}$ and $\dot{\vec{M}}$ that $\dot{\vec{M}} = -\vec{M}x(\vec{M}x\dot{\vec{M}})/M_s^2$, the LLG equation, Equation (2), can be written in the field form as

$$\vec{M}x(\vec{H}_g + \vec{H}_r + \vec{H}_\alpha) = 0 \quad , \tag{5}$$

where the gyrotropic field is

$$\vec{H}_g = -(1/|\gamma|M_s^2)\,\vec{M}\times\dot{\vec{M}} \quad , \tag{5a}$$

the dissipative equivalent field is

$$\vec{H}_\alpha = -(\alpha/|\gamma|M_s)\dot{\vec{M}} \tag{5b},$$

and the reversible effective field is still $\vec{H}_r$. The gyrotropic equivalent field is in the direction normal to both the direction of $\vec{M}$ and $\dot{\vec{M}}$ while the dissipative equivalent field is in the direction opposite to $\dot{\vec{M}}$. Equation (5) is equivalent to the statement that the resultant equi lent field $(\vec{H}_g+\vec{H}_r+\vec{H}_\alpha)$ is parallel to $\vec{M}$, in other words

$$\vec{H}_g + \vec{H}_r + \vec{H}_\alpha = C\vec{M} \tag{6a}$$

where C is a scalar quantity. Since the gyrotropic field and the dissipative field, $\vec{H}_g$ and $\vec{H}_\alpha$ as given in Equation (5a) and (5b), respectively, are both normal to $\vec{M}$, the scalar C can be found by dotting $\vec{M}$ to Equation (6a). Substituting this value of C into Equation (6a) yields a pure field equation

$$\vec{H}_g + \vec{H}_r + \vec{H}_\alpha - \vec{M}(\vec{M}\cdot\vec{H}_r)/M_s^2 = 0 \tag{6b}$$

or

$$\vec{H}_g + \vec{H}_r + \vec{H}_\alpha + \vec{H}_m = 0$$

where

$$\vec{H}_m = -\vec{M}(\vec{M}\cdot\vec{H}_r)/M_s^2 \tag{6c}$$

is called the self field of the spin. It is no surprise that the equivalent field equation set no constraint in the direction of $\vec{M}$, since this equivalent field equation was derived from the torque on M while the field in the $\vec{M}$ direction does not contribute any torque. The Landau-Lifshitz-Gilbert equation is a vector equation in the two directions orthogonal to the magnetization and so is the field equation.

### 2.2.3 Force Definition and the Force Density Equation

To deal with the movement of the spin structures, force is more intuitive and convenient than torque. The force on a spin structure is defined as the rate of change of energy as the structure undergoes an infinitesimal linear movement.

Consider a spin of an arbitrary function form, $\vec{M}=\vec{M}(\vec{x}-\vec{X})$, in the volume v, where $\vec{x}$ is the spatial coordinate and $\vec{X}$ denotes the location of the structure. The potential energy of this spin structure in the presence of an arbitrary magnetic field, $\vec{H}_a$, is

$$E_a = \int_v -\vec{H}_a(\vec{x})\ \vec{M}(\vec{x}-\vec{X})\ d^3x \qquad (7)$$

The force on the structure because of the field, $\vec{H}_a$, is equal to the spatial derivative of energy with respect to the location of the structure, i.e.,

$$\int_v \underset{\sim}{f}_a\ d^3x = -\underset{\sim}{\nabla}_X E_a = \int_v \vec{H}_a(\vec{x})\cdot\underset{\sim}{\nabla}_X\vec{M}(\vec{x}-\vec{X})\ d^3x$$

$$= \int_v -\vec{H}_a(x)\cdot\nabla_v\vec{M}(\vec{x}-\vec{X})\ d^3x \quad . \qquad (8)$$

The equality of Equation (8) must hold for an arbitrary volume v chosen, which implies that the two integrands must be equal,

$$\underset{\sim}{f}_a = -\vec{H}_a \cdot \underset{\sim}{\nabla}\vec{M} \quad , \tag{9}$$

if both integrands are spatial continuous functions [10].

The Landau-Lifshitz-Gilbert equation in the field form, Equation (6), can now be rewritten in the force form by transforming each field using Equation (9). The force form of the LLG equation is

$$\underset{\sim}{f}_g + \underset{\sim}{f}_r + \underset{\sim}{f}_\alpha = 0 \quad , \tag{10}$$

where the gyrotropic force density is

$$\vec{f}_g = (1/|\gamma|M_s^2)\vec{M}x\dot{\vec{M}}\cdot\underset{\sim}{\nabla}\vec{M} = (1/|\gamma|M_s^2)\vec{M}\cdot(\dot{\vec{M}}x\underset{\sim}{\nabla}\vec{M}) \tag{10a}$$

the reversible force density is

$$\underset{\sim}{f}_r = -\vec{H}_r \cdot \underset{\sim}{\nabla}\vec{M} \tag{10b}$$

and the dissipative force density is

$$\underset{\sim}{f}_\alpha = (\alpha/|\gamma|M_s)\dot{\vec{M}}\cdot\underset{\sim}{\nabla}\vec{M} \tag{10c}$$

The self field $\vec{H}_m$ does not contribute to the force since it is in the direction of $\vec{M}$ which is always orthogonal to $\underset{\sim}{\nabla}\vec{M}$, as was given in Equation (3b).

2.2.4 Validity of the Force Density Equation

The force density equation, Equation (10), can also be derived directly from the Landau-Lifshitz-Gilbert torque equation, Equation (2). If the left side of the LLG equation is crossed with $\vec{M}/M_s^2$ and

then the dot-product with $\underset{\sim}{\nabla}\vec{M}$ taken, the result is

$$\vec{M}/M_s^2 \text{x Equation (2)} \cdot \underset{\sim}{\nabla}\vec{M} = \text{Equation (10)} \quad ,$$

the force density equation, Equation (10), results. This equality shows that the force equation is consistent with the LLG equation.

It can also be shown that the force density equation is equivalent to the LLG equation if, and only if, $\underset{\sim}{\nabla}\vec{M}$ is of rank two. It can be seen that $\underset{\sim}{\nabla}\vec{M}$ cannot be of rank three because $\vec{M}\cdot\underset{\sim}{\nabla}\vec{M}=0$ (Equation (3b)), i.e., $\underset{\sim}{\nabla}\vec{M}$ has an eigenvector $\vec{M}$ with eigenvalue 0; therefore, $\underset{\sim}{\nabla}\vec{M}$ is singular. If $\underset{\sim}{\nabla}\vec{M}$ is of rank two, it will span all the subspace orthogonal to $\vec{M}$. Since all of terms in $\vec{M}/M_s^2$ x Equation (2) are orthogonal to $\vec{M}$, they are in the subspace spanned by $\underset{\sim}{\nabla}\vec{M}$. Taking a dot product with $\underset{\sim}{\nabla}\vec{M}$, therefore, will not cause any information in $\vec{M}/M_s^2$ x Equation (2) to be lost. Since $\vec{M}$ is orthogonal to all of the terms in Equation (2), $\vec{M}/M_s^2$ x Equation (2) carries exactly the same amount of information as does Equation (2). So, the force density equation, Equation (10), is equivalent to the LLG equation, Equation (2). If $\underset{\sim}{\nabla}\vec{M}$ is of rank one or zero, the force density equation will have only one, or no, linear independent scalar equation, respectively. Obviously the force equation is not equivalent to the LLG equation which has two linear independent scalar equations.

As a trivial example, consider a structureless case, where all of the spins align in the same direction spatially, i.e., $\underset{\sim}{\nabla}\vec{M}=0$, $\underset{\sim}{\nabla}\vec{M}$ is of rank zero. The force equation, Equation (10), becomes

$\dot{\theta}=0$, a case which is consistent with the LLG equation although it carries no information. On the other hand, the force density is defined as the rate of change of the energy as the local spin structure goes through an infinitesimal movement. Since no spin structure is present in this case, the force is zero. The motion of the spins here can only be described by the torque equation or the equivalent field equation. An example for the case when $\underset{\sim}{\nabla}\vec{M}$ is rank one, a planar domain wall, will be given later in Section 2.2.9.

### 2.2.5 Force Density Equation in $\theta$ and $\psi$ Representation

The force density equation can be expressed explicitly by using the polar and the azimuthal angles $\theta$ and $\psi$, respectively, to describe the direction of the local magnetization. Since the gyrotropic force and the dissipative force in Equation (10a) and (10c) are both in a certain closed form of $\vec{M}$, they are insensitive to the vector basis used. The simplest local orthogonal basis $(e_r, e_\theta, e_\psi)$ gives

$$\vec{M} = M_s \hat{e}_r \tag{11a}$$

$$\dot{\vec{M}} = M_s(\dot{\theta})\hat{e}_\theta + \sin\theta\dot{\psi}\hat{e}_\psi \tag{11b}$$

$$\underset{\sim}{\nabla}\vec{M} = M_s(\underset{\sim}{\nabla}\theta)\hat{e}_\theta + \sin\theta(\underset{\sim}{\nabla}\psi)\hat{e}_\psi \tag{11c}$$

Substituting these expressions into the force equation, Equation (10), the gyrotropic force and the dissipative force become

$$\underset{\sim}{f}_g = (M_s/|\gamma|)\sin\theta(\dot{\theta}\underset{\sim}{\nabla}\psi - \dot{\psi}\underset{\sim}{\nabla}\theta)$$

$$= (M_s/|\gamma|)\,(\dot{\psi}\underset{\sim}{\nabla}\cos\theta - (\cos\theta)\underset{\sim}{\nabla}\psi) \qquad (12a)$$

and

$$\underset{\sim}{f}_\alpha = (\alpha M_s/|\gamma|)\,(\dot{\theta}\underset{\sim}{\nabla}\theta + \sin^2\theta\dot{\psi}\underset{\sim}{\nabla}\psi) \qquad (12b)$$

The reversible force density is not included here because the overall reversible force for the spin structure can easily be obtained from the total energy of the structure.

2.2.6 Gyrotropic and Dissipative Forces for Spin Structures

The overall force on a spin structure, which can be either a magnetic bubble or portion of the domain wall, can be obtained by integrating the force densities, Equation (12), over the spin structure. This property was previously used in defining the force densities, as described in Section 2.2.3. The total gyrotropic force can then be written as

$$\underset{\sim}{F}_g = \int \underset{\sim}{f}_g dv = (M_s/|\gamma|)\int \dot{\psi}\underset{\sim}{\nabla}\cos\theta - (\cos\theta)\underset{\sim}{\nabla}\psi \; dv \qquad (13a)$$

and the total dissipative force of the structure is

$$\underset{\sim}{F}_\alpha = \int \underset{\sim}{f}_\alpha dv = (\alpha M_s/|\gamma|)\int(\dot{\theta}\underset{\sim}{\nabla}\theta + \sin^2\theta\dot{\psi}\underset{\sim}{\nabla}\psi)\; dv \quad . \qquad (13b)$$

The purpose of having a force equation is to solve for the magnetization as a function of time. The expressions, Equation (13a) and (13b), are not very useful except in the case where $\theta$ and $\psi$ have a special

dependence such that they can be taken out of the integral. The overall force of the spin structure in general cannot be evaluated since the integrands are yet to be solved.

### 2.2.7 Translational Motion of Spin Structures

In the case of translational motion of spin structures, where the whole structure is translating with a velocity $\vec{V}$ while the shape of the structure remains unchanged, the force functions can be greatly simplified. The velocity, $\vec{V}$, of the structure is assumed to be a constant spatially throughout the structure considered and is allowed to change as a function of time. The magnetization, in this case, is a function of $\vec{x}-\vec{V}t$, i.e., $\vec{M} = \vec{M}(\vec{x}-\vec{V}t)$, where $\vec{x}$ denotes the spatial location of the magnetization. Time derivative operator becomes d/dt $= -(\vec{V}\cdot\vec{\nabla})$. The gyrotropic force density becomes

$$\begin{aligned}\vec{f}_g &\overset{*}{=} (M_s/|\gamma|)(-\vec{V}\cdot\vec{\nabla}\psi)\vec{\nabla}\cos\theta + (\vec{V}\cdot\vec{\nabla}\cos\theta)\vec{\nabla}\psi \\ &= (M_s/|\gamma|)(\vec{\nabla}\cos\theta x\vec{\nabla}\psi)x\vec{V} \quad .\end{aligned} \tag{14}$$

The gyrotropic force density can then be described by a vector $\vec{g}$, called the gyrocoupling vector, such that

$$\vec{f}_g = \vec{g}x\vec{V} \quad . \tag{15a}$$

The gyrocoupling vector is defined as

$$\vec{g} = (M_s/|\gamma|)\ (\vec{\nabla}\cos\theta x\vec{\nabla}\psi) \quad . \tag{15b}$$

The dissipative force density, Equation (12b), becomes

$$\underset{\sim}{f}_{\alpha} = (\alpha M_s/|\gamma|)(\nabla\theta\vec{\nabla}\theta + \sin^2\theta\underset{\sim}{\nabla}\psi\vec{\nabla}\psi)\cdot\vec{V} \quad , \tag{16}$$

which can again be written as

$$\underset{\sim}{f}_{\alpha} = \underset{\sim}{\vec{d}}\cdot\vec{V} \tag{17a}$$

where $\underset{\sim}{\vec{d}}$ is called the dissipative dyadic, which is defined as

$$\underset{\sim}{\vec{d}} = (\alpha M_s/|\gamma|)(\underset{\sim}{\nabla}\theta\vec{\nabla}\theta + \sin^2\theta\underset{\sim}{\nabla}\psi\vec{\nabla}\psi) \quad . \tag{17b}$$

The gyrotropic and the dissipative force densities as well as the gyrocoupling vector and the dissipative dyadic are now only functions of the spatial derivatives of the magnetization.

The overall gyrotropic force of the spin structure can then be written as

$$\vec{F}_g = \int \vec{f}_g dv = \int \vec{g}x\vec{V}\ dv = \vec{G}x\vec{V} \tag{18a}$$

where the total gyrocoupling vector of the spin structure, $\vec{G}$ is

$$\vec{G} = \int \vec{g}\ dv = (M_s/|\gamma|)\int \vec{\nabla}\cos\theta x\vec{\nabla}\psi\ dv \quad . \tag{18b}$$

The gyrocoupling vector, $\vec{G}$, is a function of the Jacobians of $\cos\theta$ and $\psi$. Equation (18b) becomes

$$G = (M_s/|\gamma|)\int \frac{\partial(\cos\theta,\psi)\hat{x}}{\partial(y,z)} + \frac{\partial(\cos\theta,\psi)\hat{y}}{\partial(z,x)} + \frac{\partial(\cos\theta,\psi)\hat{z}}{\partial(x,y)}$$

$$\cdot\ dx\ dy\ dz \quad . \tag{19}$$

This special property of the gyrocoupling vector makes the evaluation of $\vec{\underset{\sim}{G}}$ trivial.

The dissipative force of the spin structure can similarly be written as

$$\underset{\sim}{F}_{\alpha} = \int \vec{\underset{\sim}{d}} \cdot \vec{V} \, dv = \vec{\underset{\sim}{D}} \cdot \vec{V} \tag{20a}$$

where the dissipative dyadic of the spin structure, $\vec{\underset{\sim}{D}}$, is

$$\vec{\underset{\sim}{D}} = \int \vec{\underset{\sim}{d}} \, dv = (\alpha M_s/|\gamma|) \int \underset{\sim}{\nabla}\theta\vec{\nabla}\theta + \sin^2\theta \underset{\sim}{\nabla}\psi\vec{\nabla}\psi \, dv \quad . \tag{20b}$$

The evaluation of the integrals of the dissipative dyadic and the gyrocoupling vector for the planar wall as well as for Bloch-lines will be given in the next section.

### 2.2.8 Gyrocoupling Vectors and Dissipative Dyadics for Planar Domain Walls and Bloch-lines

The dynamic forces for planar domain walls in translation will be discussed here. Planar walls and walls with Bloch-lines represent two of the most common idealized spin structures. The two dynamic forces, the gyrotropic force and the dissipative force, are represented by the gyrocoupling vector, $\vec{G}$, and the dissipative dyadic, $\vec{\underset{\sim}{D}}$, respectively. They will be evaluated by taking the spatial integration of Equation (19) and (20b) over the spin structure. The structures selected will be the idealized planar wall and a wall with a Bloch-line. More realistic structures are much more complicated but are not very different from

the ideal ones. Previously in Section 1.3.2, it was shown that the static wall shape in high Q material changes only slightly in the presence of the demagnetizing field or an inplane field of the order of $4\pi M_s$. The assumption that these fields are negligible is reasonable. Walls in the bubble domains are curved, but the radius of curvature is large compared to the wall width. The typical radius of a bubble is a factor of 40 times larger than the width of the wall. The simple planar wall model is, therefore, still a good approximation. As an example of a structure within the wall, Bloch-lines were chosen because they represent a class of structures that will be used repeatedly to explain the actual wall dynamics.

To evaluate the integrals, Equation (19) and Equation (20b), for a planar wall, assume a conventional Bloch wall shape, as derived in Section 1.3.2, with the wall in the xz plane and the polar angle of the spins given by

$$\cos\theta = \tanh(\pi y/\ell_w) \quad , \tag{21}$$

where $\ell_w$ is the wall width parameter and is a function of $\psi$.
The azimuthal angle of the spin is constant spatially so that:

$$\nabla\psi = 0 \quad . \tag{22}$$

Therefore, the gyrocoupling vector,

$$\vec{G} = 0 \quad , \tag{23}$$

as can be seen from Equation (18b) that the integrand, $\vec{\nabla}\cos\theta x\vec{\nabla}\psi$, is

zero. The gradient of the polar angle can be calculated from Equation (21) to be

$$\vec{\nabla}\theta = -(\pi/\ell_w)\,\mathrm{sech}(\pi y/\ell_w)\hat{y} \quad . \tag{24}$$

Therefore, the dissipative dyadic, $\overset{\leftrightarrow}{D}$, will have a value since the first of the integrands is nonzero. Since $\vec{\nabla}\theta$ is nonzero only in the $\hat{y}$ direction, where $\hat{y}$ is the direction normal to the wall, only $D_{yy}$ has a value. Substituting Equation (24) into Equation (20b), the dissipative dyadic can be found:

$$D_{yy} = -(\alpha M_s/|\gamma|)\int_{-\frac{\Delta z}{2}}^{\frac{\Delta z}{2}}\int_{-\infty}^{\infty}\int_{-\frac{\Delta x}{2}}^{\frac{\Delta x}{2}} (\pi/\ell_w)^2\,\mathrm{sech}(\pi y/\ell_w)\,dx\,dy\,dz$$

$$= -(\alpha\pi M_s/\ell_w)\Delta x\Delta z\,\tanh(y)\Big]_{-\infty}^{\infty}$$

$$= -2M_s\Delta x\Delta z/(|\gamma|\,\ell_w/\alpha\pi) = -(2M_s/u_b)\Delta x\Delta z \quad , \tag{25}$$

where $\Delta x\Delta z$ describes the area of the domain wall and $u_b$ is the theoretical mobility of the wall

$$u_b = |\gamma|\ell_w/\pi\alpha \quad . \tag{26}$$

The dissipative force per unit area is, therefore,

$$F_\alpha/\text{area} = -2M_s/u_b \quad . \tag{27}$$

The dynamic forces on the Bloch-line can be obtained by calculating

the difference between the forces on a wall containing a Bloch-line and a wall without a Bloch-line. Consider the presence of a single Bloch-line in an infinite Bloch wall. Again the wall is assumed to be in the xz plane with the center of the Bloch-line located along the z axis. The static wall shape and Bloch-line shape, as derived in Section 1.3.3, are assumed. The polar angle and the azimuthal angle, as given in Equation (1.34), are written as

$$\cos\theta = \tanh(\pi y/\ell_w) \tag{28a}$$

and

$$\cos\psi = \tanh(\pi x/\ell_{\ell o}) \tag{28b}$$

where $\ell_w$ is the wall width parameter defined by Equation (1.34d) as

$$\ell_w = \pi(A/K)^{\frac{1}{2}}(1+2\sin^2\psi/Q)^{-\frac{1}{2}}$$

$$= \ell_{wo}(1+2\sin^2\psi/Q)^{-\frac{1}{2}} \quad , \tag{28c}$$

and $\ell_{\ell o}$ is the Bloch-line width parameter defined by Equation (1.34c) as

$$\ell_{\ell o} = \pi(A/2\pi M_s^2)^{\frac{1}{2}} = \ell_{wo}Q^{\frac{1}{2}} \quad . \tag{28d}$$

The gyrocoupling vector for the Bloch-line is calculated by integrating the local g-vector over the Bloch-line structure. Since the g-vector is a function of the Jacobian of $(\cos\theta,\psi)$, the integral of g-vector is trivial. The total G-vector has components only along the z direction, since $\theta$ and $\psi$ are functions of x and y only. Substituting Equation

(28b) into Equation (19) yields

$$\vec{G} = (M_s/|\gamma|)\hat{z}\int \frac{\partial(\cos\theta,\psi)}{\partial(x,y)}\,dx\,dy\,dz$$

$$= (M_s/|\gamma|)\hat{z}\int_0^{\Delta z}\int_{-\infty}^{\infty}\int_{-\infty}^{\infty} -(\partial\cos\theta/\partial y)(\partial\psi/\partial x).dx.dy.dz$$

$$= -(M_s/|\gamma|)\Delta\cos\theta)(\Delta\psi)(\Delta z)\hat{z} = (2\pi M_s/|\gamma|)(\Delta z)\hat{z} \quad . \qquad (29)$$

As can be seen, the G-vector is in the $\hat{z}$ direction since $(\vec{\nabla}\cos\theta)$ is in $\hat{y}$ direction and $(\vec{\nabla}\psi)$ is in $-\hat{x}$ direction so that $(\vec{\nabla}\cos\theta x\vec{\nabla}\psi)$ will be in the $\hat{z}$ direction. The magnitude of the G-vector per unit Bloch-line length is $(2\pi M_s/|\gamma|)$.

The Bloch-line dissipative dyadic, $\underset{\sim}{\vec{D}}'$, which is defined as the added domain wall dissipative dyadic due to the presence of the Bloch-line, can now be evaluated. The change of the wall width in the vicinity of the Bloch-line must be included in the integral. In a way similar to the evaluation of $D_{yy}$ in Equation (25), $D'_{nn}$ can be calculated:

$$D'_{nn} = -(2\pi M_s\alpha/|\gamma|)(\Delta z)\int_{-\infty}^{\infty} (1/\ell_w(\psi) - 1/\ell_{wo})\,dx$$

$$\sim -(2\pi M_s\alpha/|\gamma|\ell_{wo})(\Delta z)\int_{-\infty}^{\infty} \sin^2\psi/Q\,dx$$

$$= -(2\pi M_s\alpha/|\gamma|\ell_{wo})(\Delta z)\int_{-\infty}^{\infty} \mathrm{sech}^2(\pi x/\ell_{\ell o})/Q\,dx$$

$$= -4M_s\alpha(\Delta z)/|\gamma|Q^{1/2} \quad , \qquad (30)$$

where subscript n denotes the direction normal to the wall. Here an approximation up to the lowest order in $Q^{-1}$ is made. The dissipation constant for the Bloch-line moving along the wall, $D'_{tt}$ can be integrated to be

$$D'_{tt} = -(\alpha M_s/|\gamma|)\int_0^{\Delta z}\int_{-\infty}^{\infty}\int_{-\infty}^{\infty} \sin^2\theta(\partial\psi/\partial x)^2 dx\, dy\, dz$$

$$= -(\alpha M_s/|\gamma|)\Delta z\ (\pi/\ell_{\ell o})^2 \int_{-\infty}^{\infty}\int_{-\infty}^{\infty} \mathrm{sech}^2(\pi y/\ell_w)\mathrm{sech}^2(\pi x/\ell_{\ell o})$$

$$\cdot\, dx \cdot dy = -(4M_s\alpha/|\gamma|Q^{1/2})\ \Delta z \quad . \tag{31}$$

It can be seen that the Bloch-line dissipation constant, $D'_{nn}$, if divided by the area occupied by the Bloch-line, $\Delta z \ell_{\ell o}$ or $\Delta z \ell_{wo} Q^{1/2}$, is a factor of $(\pi Q/2)$ times smaller than the dissipation of the wall per unit area.

Experimentally the observed effects of Bloch-lines are usually characterized by a Bloch-line deflection tangential to the wall and a large reduction in the wall mobility in that section of the wall occupied by the Bloch-line. These two effects can be better understood by considering the dynamic Bloch-line forces. These forces include both the gyrotropic force and the dissipative force; however, Bloch-line damping is a factor of $(\pi Q/2)$ times smaller than the damping of the wall occupied by the Bloch-line. For the typical sample, this Bloch-line damping is less than 4% of the wall damping, so, only the

gyrotropic force of the Bloch-line will be discussed here. A more detailed example of the dynamic Bloch-line forces will be discussed in Section 2.2.11.

The most direct approach to the overall gyrotropic force is given by Equation (18a) now that the total G-vector has been obtained in Equation (29). Using the unit vector $\hat{n}$, $\hat{G}$, and $\hat{t}$ as before with $\hat{n}$ in the direction of $\vec{\nabla}\cos\theta$, $\hat{G}$ in the direction of the Bloch-line G-vector, and $\hat{t}$ in the direction of $\hat{G}x\hat{n}$, the domain wall velocity can be written as $V_n\hat{n}$, with $V_n$ either positive or negative. The velocity of the Bloch-line can be decomposed into two parts, the velocity of the wall occupied by the Bloch-line, $V_n\hat{n}$, and the deflection velocity of the Bloch-line along the wall, $V_t\hat{t}$,

$$\vec{V}_{BL} = V_n \hat{n} + V_t \hat{t} \quad . \tag{32}$$

The gyrotropic force on the Bloch-line per unit Bloch-line length, using Equation (18a) and (29), is

$$\vec{F}_g/\text{BL length} = (2\pi M_s/|\gamma|)\ \hat{G}x\vec{V}_{BL}$$

$$= (2\pi M_s/|\gamma|)(V_n\hat{t} - V_t\hat{n}) \quad . \tag{33}$$

The first term in Equation (33) is a force in the direction transverse to the wall, which will cause a deflection of the Bloch-line along the wall. The Bloch-line velocity, velocity components, $V_t$ and $V_n$, therefore have the same sign. The second term in Equation (33) is always in the direction of $-V_n\hat{n}$, i.e., in the direction to oppose the

wall motion. This normal component of the Bloch-line G-force is a factor of $((1/\alpha Q^{1/2})(V_t/V_n))$ larger than the regular damping force of the domain wall occupied by the Bloch-line. The expression $(1/\alpha Q^{1/2})$ is about 10 for the typical sample. The ratio $(V_t/V_n)$ is normally larger than one in radial motion experiments and straight wall motion experiments due to the relatively low damping constant of the Bloch-line in the direction transverse to the wall. Therefore, the gyrotropic forces on the Bloch-line can be used to explain the observed deflection of the Bloch-line and the reduction in the wall mobility.

### 2.2.9 One Dimensional Planar Wall Motion

The equation of motion of a wall can be formulated by assuming a one-dimensional planar wall model. This wall is a good approximation to the structure of a real wall as seen in Section 1.3.2 and the dynamic forces involved are also realistic. The one-dimensional planar wall can be characterized by two variables, the location of the wall center, denoted by q, and the precession angle $\psi$. The precession angle here is defined as the azimuthal angle which describes the plane in which spins precess across the wall. This azimuthal angle is assumed to be spatially constant in the present case, which corresponds to a lower exchange energy state. Other cases where the precession angle is not constant spatially also exist and it is normally included when the curvature of the wall or Bloch-line structure is considered. The shape of the wall will be approximated by

$$\cos\theta = \tanh[\pi(y-q)/\ell_w(\psi)] \quad , \tag{34}$$

where

$$\ell_w(\psi) = [A/(K+2\pi M_s{}^2\sin^2\psi)]^{1/2} \quad . \tag{35}$$

The steady state total force equation, equation (10), becomes

$$\vec{F}_r + \vec{F}_g + \vec{F}_\alpha = 0 \quad , \tag{36}$$

where $\vec{F}_r$, $\vec{F}_g$ and $\vec{F}_\alpha$ are the external force, gyrotropic force and the dissipative force, respectively. The external force on the wall due to the applied field $H_z\,\hat{y}$ is

$$\vec{F}_r = 2M_s H_z \Delta x \Delta z \;\; \hat{y} \tag{37}$$

which is the rate change of the Zeeman energy per unit displacement of the wall. The steady state gyrotropic force, as a result of Equation (18a) and Equation (23), is

$$\vec{F}_g = 0 \quad . \tag{38}$$

The dissipative force, using Equation (20a) and Equation (25), is

$$\vec{F}_\alpha = -2M_s \Delta x \Delta z \; V_y/\mu_b \; \hat{y} \quad , \tag{39}$$

where $\mu_b$ is the theoretical mobility defined in Equation (26). For this case, the total force equation becomes

$$2M_s(H_z - V_y/\mu_b)\Delta x \Delta z = 0 \quad . \tag{40}$$

Therefore,

$$V_y = \mu_b H_z \quad , \tag{41}$$

i.e., the steady state wall velocity is proportional to the external applied field $H_z$ with $\mu_b$ the proportionality constant. This is the classical definition of mobility.

For a more general wall motion, including the nonsteady state case, the gyrotropic force calculated from Equation (12) is

$$\begin{aligned}\vec{F}_g &= \int \vec{f}_g dv = (M_s/|\gamma|)\int \dot{\psi}\vec{\nabla}\cos\theta \, dv \\ &= (M_s \dot{\psi}/|\gamma|)h \, \Delta x \int \frac{\pi}{\ell_w} \operatorname{sech}^2(\pi(y-q)/\ell_w) \, dy \;\; \hat{n} \\ &= (2M_s \dot{\psi}/|\gamma|) \, h\Delta x \, \hat{n} \quad .\end{aligned} \tag{42}$$

The damping force and the reversible force remain the same as those of the steady state case. The force equation reads:

$$(2M_s h\Delta x)(\dot{\psi}/|\gamma| - H_z - v/\mu_b) = 0$$

or

$$\dot{\psi}/|\gamma| - H_z - v/\mu_b = 0 \quad . \tag{43}$$

In the limiting case of the steady state, $\psi$=0 and Equation (43) equals Equation (41). The deviation of the wall velocity from that given by the linear mobility is always accompanied with a precession in $\psi$. Equation (43) cannot provide information about the transient time needed for the wall to reach steady state motion nor can it give the

limit of the drive field beyond which the steady state solution does not occur. An additional equation in $\psi$ is required to obtain this information. As is discussed in Section (2.2.4), $\nabla\vec{\tilde{M}}$ for the one-dimension planar wall case is of rank one so that the force equation is not equivalent to LLG equation. Therefore, the use of the force equation does not guarantee a unique solution. An additional constraint on $\psi$ can be obtained from the torque equation in the z direction.

The detailed construction of the torque equation will be discussed later. For those cases where a strong constraint is imposed on the spins to suppress the $\psi$ precession, such as the case with a strong DC inplane field or a strong inplane anisotropy (inplane hard axis), the motion of the wall can be described by the simple linear mobility equation.

2.2.10 Lagrangian Formulation for One-Dimensional Planar Wall

The Lagrangian formulation can provide the torque equation in addition to a force equation that is needed for solving the nonsteady state planar wall motion and for finding the threshold for the drive field strength beyond which a steady state solution does not exist. A general Lagrangian function approach would normally result in coupled, time dependent, nonlinear partial differential equations for the dynamic wall shape. The approach is greatly simplified by approximating the dynamic wall shape with a static wall structure. This

approximation is good for high Q materials since, in this case, the main energies in determining the wall shape come from the static anisotropy and the exchange interaction. The dynamic terms that are normally proportional to $4\pi M_s$ are not significant.

The Lagrangian density function and the Rayleigh dissipation density function will be constructed here. One constraint on this construction is that the equation of the motion for the local spin should be consistent with the LLG equation. The kinetic energy density for free spins with angular momentum $-M_s/|\gamma|$ can be written as the limit of a massless top:

$$e_{KE} = (M_s/|\gamma|)\psi(\partial\cos\theta/\partial t) \tag{44a}$$

or

$$e_{KE} = -(M_s/|\gamma|)\dot{\psi}\cos\theta \quad , \tag{44b}$$

where the angle $\theta$ and $\psi$ denote the polar angle and the azimuthal angle of the spin. These two expressions differ by a total derivative of time but they result in the same equation of motion. The functional derivative of this kinetic energy density with respect to $\theta$ and $\psi$ give the two components of $\dot{\vec{M}}/|\gamma|$ in the direction normal to $\vec{M}$:

$$\left(\frac{d}{dt}\frac{\partial}{\partial\dot{\theta}} - \frac{\partial}{\partial\theta}\right) e_{KE} = -(M_s/|\gamma|)\,\dot{\psi}\sin\theta = -(\dot{\vec{M}}/|\gamma|)\cdot\hat{e}_{\psi} \tag{45a}$$

$$\left(\frac{d}{dt}\frac{\partial}{\partial\dot{\psi}} - \frac{\partial}{\partial\psi}\right) e_{KE} = -(M_s/|\gamma|)\dot{\theta} = -(\dot{\vec{M}}/|\gamma|)\cdot\hat{e}_{\theta} \tag{45b}$$

with direction vectors $\hat{e}_{\theta}$ and $\hat{e}_{\psi}$ defined in Figure (1.5). The potential energy of the spin is

$$e_H = -\vec{M}\cdot\vec{H} = -M_s(H_z\cos\theta + H_x\sin\theta\cos\psi + H_y\sin\theta\sin\psi) \quad , \qquad (46)$$

where $\vec{H}$ is the effective field at the location of the spin. The Rayleigh dissipation density function is equal to $(\alpha\dot{\vec{M}}^2/2|\gamma|M_s)$, which expressed in terms of $\theta$ and $\phi$ is

$$f_\alpha = \alpha\dot{\vec{M}}^2/2|\gamma|M_s = (\alpha M_s/2|\gamma|)(\dot{\theta}^2 + \dot{\psi}^2\sin^2\theta) \qquad (47)$$

To obtain an equation of motion of local spins, the Lagrangian density function must be written. It is equal to the kinetic energy density minus the potential energy density:

$$L = (M_s/|\gamma|)(\psi\partial\cos\theta/\partial t) + M_s(H_z\cos\theta + H_x\sin\theta\cos\psi + H_y\sin\theta\sin\psi) \qquad (48)$$

Using Hamilton's principle, the equation of motion of a local spin is:

$$\left(\frac{d}{dt}\frac{\partial}{\partial\dot{\theta}} - \frac{\partial}{\partial\theta}\right)L = -\frac{\partial f}{\partial\dot{\theta}}$$

$$\left(\frac{d}{dt}\frac{\partial}{\partial\dot{\psi}} - \frac{\partial}{\partial\psi}\right)L = -\frac{\partial f}{\partial\dot{\psi}} \quad . \qquad (49)$$

Substituting Equation (48) into Equation (49), results in

$$-(M_s/|\gamma|)(\dot{\psi}\sin\theta) + M_s(H_z\sin\theta - H_x\cos\theta\cos\psi - H_y\cos\theta\sin\psi)$$

$$= (-\alpha M_s/|\gamma|)\dot{\theta}$$

$$(M_s/|\gamma|)\sin\theta\,\dot{\theta} + M_s(H_x\sin\theta\sin\psi - H_y\sin\theta\cos\psi)$$

$$= (-\alpha M_s/|\gamma|)\dot{\psi}\sin^2\theta \quad . \tag{50}$$

Equation (50) is identical to the LLG equation.

The Lagrangian function of the wall can be obtained by integrating the Lagrangian density function over the wall. The following two equalities:

$$\int_{-\infty}^{\infty} \operatorname{sech}^2 by\,dy = \frac{2}{b} \tag{51}$$

$$\int_{-\infty}^{\infty} \operatorname{sech}\, by\,dy = \frac{\pi}{b} \tag{52}$$

are used in the later integration. The kinetic energy per unit wall area is

$$E_{KE/area} = \int \frac{M_s}{|\gamma|}\,\psi\,\frac{\partial}{\partial t}\cos\theta\,dy$$

$$= \frac{M_s}{|\gamma|}\int -\frac{\pi}{\ell\omega}\,\dot{q}\psi\sin^2\theta\,dy$$

$$= -\frac{2M_s}{|\gamma|}\,\psi\dot{q} \tag{53}$$

The potential energy of the wall can be divided into that part from the applied field and that part from the energy of the wall itself. The former can be written as

$$E_H/area = 2M_sH_zq \quad . \tag{54}$$

The wall energy, as a result of section (1.3.2), can be written as

$$E_w/\text{area} = 4\sqrt{A(K+2\pi M_s^2 \sin^2\psi)} \quad . \tag{55}$$

The Lagrangian function for the wall per unit area can then be written as

$$L = -\frac{2M_s}{|\gamma|}\dot{\psi q} - 4\sqrt{A(K+2\,M_s^2\sin^2\psi)}$$

$$- 2M_s H_z q \tag{56}$$

The Rayleigh dissipation function is obtained as

$$F/\text{area} = \int \frac{\alpha M_s}{2|\gamma|}(\dot{\theta}^2 + \dot{\psi}^2 \sin^2\theta)dy$$

$$= \frac{\alpha M_s}{2|\gamma|}\int \sin^2\theta\left(\frac{\pi^2}{\ell_w}\dot{q}^2 + \dot{\psi}^2\right) dy$$

$$= \frac{\alpha M_s}{|\gamma|}\left(\frac{\pi}{\ell_w}\dot{q}^2 + \frac{\ell_w}{\pi}\dot{\psi}^2\right) \quad . \tag{57}$$

The first term in the Equation (57) is the dissipation due to the wall motion while the second term describes the damping dissipation due to the precession of the spin in the wall.

The equation of the motion of the system can now be calculated using Hamilton's principle:

$$\frac{d}{dt}\frac{\partial L}{\partial \dot{q}} - \frac{\partial L}{\partial q} = -\frac{\partial F}{\partial \dot{q}}$$

$$\frac{d}{dt}\frac{\partial L}{\partial \dot{\psi}} - \frac{\partial L}{\partial \psi} = -\frac{\partial F}{\partial \dot{\psi}} \tag{58}$$

Substituting Equation (56) and Equation (57) into Equation (58), the

equation of motion is obtained:

$$-\frac{2M_s}{|\gamma|}\dot{\psi} + 2M_s H_z = -\frac{2\pi M_s \alpha}{|\gamma| \ell_w}\dot{q} \tag{59a}$$

$$\frac{2M_s}{|\gamma|}\dot{q} + 4\pi M_s^2 \sin 2\psi \frac{\ell_w}{\pi} = -\frac{2M_s}{|\gamma|}\frac{\alpha \ell_w}{\pi}\dot{\psi} \quad . \tag{59b}$$

Equation (59a) is a force equation which is exactly the same as that obtained from the force formulation. Equation (59b) is a torque equation in the $\hat{z}$ direction. After few algebraic operations, Equation (59) can be rewritten as

$$\frac{\dot{q}}{\mu_b} = \frac{\alpha}{1+\alpha^2}(\alpha H_z + 2\pi M_s \sin 2\psi) \tag{60a}$$

$$\frac{\dot{\psi}}{|\gamma|} = \frac{\alpha}{1+\alpha^2}\left(\frac{H_z}{\alpha} - 2\pi M_s \sin 2\psi\right) \tag{60b}$$

with $\mu_b = |\gamma| \ell_w / \alpha\pi$.

Steady state motion can be achieved if $H_z < 2\pi M_s \alpha$. Under this condition the motion exhibits a linear mobility, $\mu_b$, constant precession angle $(\sin^{-1}(H_z/2\pi M_s \alpha)/2)$. No steady state solution exists when $H_z > 2\pi M_s \alpha$ and the wall spins precess around the $\hat{z}$ direction. The maximum steady state velocity occurs at $H_z = 2\pi M_s \alpha$ and is

$$V_{st\ max} = \mu_b 2\pi M_s \alpha = 2\pi M_s |\gamma| \ell_{wo} / \pi \quad . \tag{61}$$

The presence of a DC inplane field $H_x$ and $H_y$ modifies the wall energy by adding a perturbation term,

$$E'/\text{wall area} = \int_{-\infty}^{\infty} -M_s(H_x\cos\psi + H_y\sin\psi)\sin\theta dy$$

$$= -\ell_w M_s(H_x\cos\psi + H_y\sin\psi) \quad . \tag{62}$$

This added wall energy term assumes that the wall width and shape are unaffected by the inplane field.

The equation of motion of the wall in the DC inplane field case is calculated by adding the functional variation of the perturbed wall energy, Equation (62), to Equation (59)

$$-\frac{2M_s}{|\gamma|}\dot{\psi} + 2M_s H_z = -\frac{2\pi M_s \alpha}{|\gamma|\ell_w}\dot{q} \tag{63a}$$

$$\frac{2M_s}{|\gamma|}\dot{q} + 4\pi M_s^2 \sin 2\psi \frac{\ell_w}{\pi} - \ell\omega M_s(H_y\cos\psi - H_x\sin\psi)$$

$$= -\frac{2M_s}{|\gamma|} \cdot \frac{\alpha\ell_w}{\pi}\dot{\psi} \quad . \tag{63b}$$

Notice that Equation (63a) remains the same as Equation (59a) and Equation (43). This is not a coincidence since the DC inplane field changes only the ease of the $\psi$ precession and does not add any effect in the form of a force. With few algebraic operations, Equation (63) can be transformed into

$$\frac{\dot{q}}{\mu_\beta} = \frac{\alpha}{1+\alpha^2}\left[\alpha H_z + 2\pi M_s \sin 2\psi - \frac{\pi}{2}(H_y\cos\psi - H_x\sin\psi)\right] \tag{64a}$$

$$\frac{\dot{\psi}}{|\gamma|} = \frac{\alpha}{1+\alpha^2}\left[\frac{H_z}{\alpha} - 2\pi M_s \sin 2\psi + \frac{\pi}{2}(H_y\cos\psi - H_x\sin\psi)\right] \quad . \tag{64b}$$

If Equation (64b) is compared with Equation (60), it is seen that the $\psi$ precession threshold changes with the inplane field. The maximum steady state velocity, therefore, is a function of the inplane field.

2.2.11 Ideal Radial Motion of Bubbles with Vertical Bloch-lines

Experimentally, some walls have been observed to move more slowly than others presumably because of structures within the wall, primarily vertical Bloch-lines. The radial motion of an ideal bubble with VBL's is presented here to demonstrate the effect of the VBL's on the domain wall motion. The bubble is assumed to be round at all times. The analysis is made on the basis of the steady motion of two spin structures, i.e., the radial motion of the wall and the translation of the VBL's within the wall.

The force equation for the unichiral bubble in the radial direction is

$$2M_s \cdot 2\pi Rh(\Delta H + \dot{R}/\mu_b) = 0 \quad , \tag{65}$$

where $\Delta H$ is the effective field on the wall in the direction to contract the bubble, R denotes the radius of the bubble, h the thickness of the bubble film and $\mu_b$ the mobility of the wall. The first term in

the equation is the external force normal to the wall and the second term is the damping dissipative force due to the wall translation as given in Equation (25). The wall velocity varies linearly with respect to the drive field similar to that of the planar wall case.

The gyrotropic force in the radial direction from a pair of positive winding VBL's can be calculated from Equation (18a) and Equation (29) to be

$$F_g\hat{e}_r = 2(2\pi M_s h/|\gamma|)V_t\hat{e}_z x\hat{e}_t = -(4\pi M_s h/|\gamma|)V_t\hat{e}_r \quad , \qquad (66)$$

where $V_t$ is the transverse circulation velocity of the VBL moving along the wall and $\hat{e}_r$, $\hat{e}_t$ and $\hat{e}_z$ are the three orthogonal unit vectors. The force equation, Equation (10), in this case can be written as

$$-4\pi M_s h \quad V_t/|\gamma| - 4\pi M_s h \; R(\Delta H + \dot{R}/\mu_b) - 8\alpha M_s h\dot{R}/|\gamma|Q^{\frac{1}{2}} = 0$$

or

$$4\pi M_s hR \; ((V_t/R|\gamma| + \Delta H + \dot{R}/\mu_b + 2\alpha\dot{R}/|\gamma|\pi Q^{\frac{1}{2}}R) = 0 \quad , \qquad (67)$$

where the last term is the additional damping due to the Bloch-lines as calculated from Equation (30) and Equation (20a). The Bloch-line velocity can be calculated from the force equation of the Bloch-line, which is

$$(2\pi M_s h/|\gamma|)\dot{R} - (4\alpha M_s h/|\gamma|Q^{\frac{1}{2}})V_t = 0 \quad . \qquad (68)$$

The velocity of the Bloch-line which balances the gyrotropic force and the dissipative force of the Bloch-line is

$$V_{BL} = \pi Q^{\frac{1}{2}}\dot{R}/2\alpha \qquad (69)$$

Substituting this Bloch-line velocity into Equation (67), the radial velocity becomes

$$\dot{R} = -\Delta H/((\pi Q^{\frac{1}{2}}/2|\gamma|R\alpha) + (1/\mu_b) + (2\alpha/\pi|\gamma|RQ^{\frac{1}{2}})) \quad . \qquad (70)$$

For a typical sample, Q is 16, R is about 3.5 microns, $\alpha$ is .026 and $|\gamma|$ is $1.1\times10^7$ radius/sec Oe. The mobility for the unichiral bubble is 12 m/sec Oe while the mobility calculated from Equation (70) for the bubble with a pair of Bloch-lines is only .16 m/sec Oe. The Bloch-line circulating velocity in this case is 240 times the radial velocity of the wall. This circulation of the VBL around the wall produces the gyrotropic pressure that retards the radial motion.

If the circular stability of the bubble is not infinite as assumed, deformation of the bubble shape will occur. Since the Bloch-line g-force is mostly localized in the region occupied by the Bloch-line, the deformation will result in a slower radial velocity of the Bloch-line, therefore, a smaller Bloch-line circulation velocity and a smaller Bloch-line g-force.

### 2.2.12 Stored Momentum

Stored momentum [10,11] is a useful concept in the interpretation of a number of dynamic effects such as overshoot and creep. The gyrotropic force due to the formation and the propagation of certain spin structures during the driven phase of the domain wall motion consumes part of the input momentum. When the drive is over, the relaxation of the spin structure back to its initial state may cause a reconstruction

of the initial drive force and result in a further motion of the domain. The momentum approach allows a semi-quantitative analysis to be made without knowing the details of the various time dependent force functions or structures involved.

In Newtonian mechanics, momentum is described by the product of the mass and the velocity, in other words the momentum is stored in the form of velocity. In a gyrotropic spin system the momentum is stored in the spin structures. If the structures are statically stable, the momentum can remain stored in the domain even when the system is motionless.

A ring shape Bloch-line [8] is chosen here to demonstrate the momentum storage during the domain wall motion. Figure (2.1) shows the projection of the spin configuration of a Bloch-ring in the xz plane. Only the center spin in the wall is drawn. The magnetization of the domain is assumed changing from the $-\hat{z}$ direction (down) to the $+\hat{z}$ direction (up) moving across the wall in the $+\hat{y}$ direction. The G vector of this Bloch-ring is, therefore, in a sense to circulate the ring in the counterclockwise direction.

When the wall is moved in the $\hat{y}$ direction, the gyrotropic force on the wall plane tends to expand the ring. The Bloch-line deflection velocity is, therefore, normal to the ring in the outward direction. The gyrotropic force acting on the domain wall due to the expansion can be calculated by integrating over the ring,

$$\vec{F}_g = \oint (2\pi M_s/|\gamma|)\hat{g}x\vec{V}_{BL}\, dl \quad , \tag{71}$$

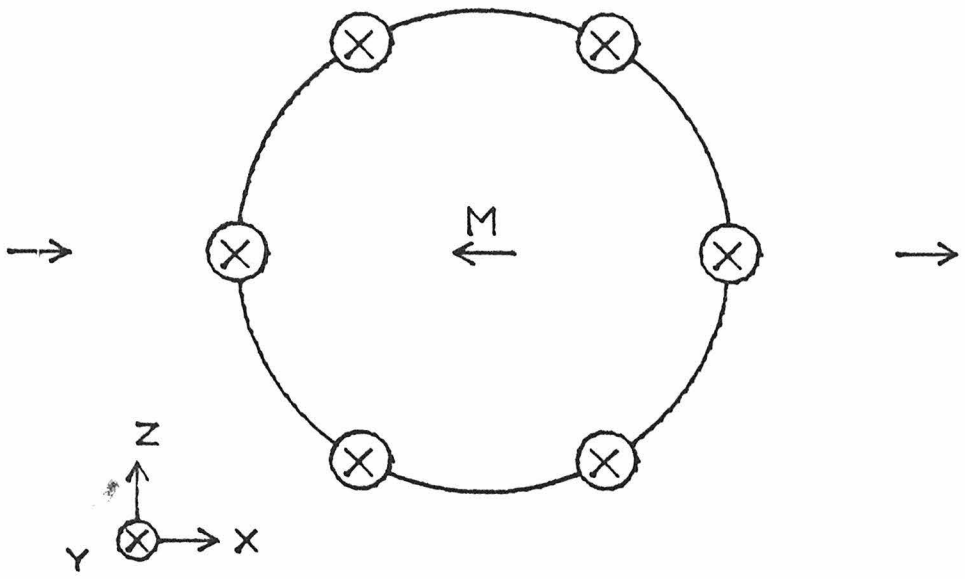


Fig.(2.1) Bloch ring configuration. Arrows describe the spin orientation in the center of the domain wall.

where $2\pi M_s/|\gamma|$ is the magnitude of the G vector per unit line length and $\vec{V}_{BL}$ is the deflection velocity of the Bloch-line tangential to the wall. The y component of the force is

$$F_{gy} = -(2\pi M_s/|\gamma|) \oint V' dl = -(2 M_s/|\gamma|)(dA_y/dt) \qquad (72)$$

where $V'$ is the component of $V_{BL}$ in the xz plane and $A_y$ is the projected ring area in the xz plane. The total momentum in the $\hat{y}$ direction being absorbed by this ring expansion is obtained by taking the time integration of the g force:

$$\Delta P_y = -\int_{t_1}^{t_2} F_{gy} dt = (2 M_s/|\gamma|)\Delta A_y \qquad (73)$$

The contraction of the ring after the driven phase is over will cause the spins in the wall to precess back as the ring passes by. This precession of the wall spins produces a gyrotropic force which will tend to move the wall in the $\hat{y}$ direction. So, a linear momentum of amount $(2\pi M_s/|\gamma|)\ A_y$ was stored in the spin structure during the driven phase. After the driven phase, the release of this moment caused the wall to continue to move.

To obtain a more general formula for the stored momentum, the most general form of the g-force formula,

$$\vec{f}_g = (M_s/|\gamma|)\ [\dot{\psi}\vec{\nabla}\cos\theta - (\dot{\cos\theta})\vec{\nabla}\psi] \quad , \qquad (74)$$

is used as a starting point. The momentum consumed by g-force is ob-

tained by taking the spatial and time integral over the negative of the force density function:

$$\Delta\vec{P} = \iint -\vec{f}_g dv\, dt$$

$$= (M_s/|\gamma|)\iint (\vec{\nabla}\psi(\partial\cos\theta/\partial t) - (\partial\psi/\partial t)\vec{\nabla}\cos\theta)dv\, dt \quad . \quad (75)$$

Since the integrand can be rewritten as

$$\partial(\cos\theta\vec{\nabla}\psi)/\partial t - \vec{\nabla}(\cos\theta(\partial\psi/\partial t)) \quad ,$$

Equation (75) can be written as

$$\Delta\vec{P} = (M_s/|\gamma|)\int_v \cos\theta\vec{\nabla}\psi\, dv \Big]_{t_0}^{t_1} - \oint_s \cos\theta(\partial\psi/\partial t)d\vec{s}\, dt \quad . \quad (76)$$

Similarly the integrand of Equation (74) can also be written as

$$-\partial(\psi\vec{\nabla}\cos\theta)/\partial t + \vec{\nabla}(\cos\theta\dot{\psi})$$

so that the momentum can be expressed as

$$\Delta\vec{P} = (M_s/|\gamma|)\int_v -\psi\vec{\nabla}\cos\theta\, dv \Big]_{t_0}^{t_1} + \oint\psi(\partial\cos\theta/\partial t)\, d\vec{s}\, dt \quad (77)$$

Normally the boundary is chosen such that $\psi$ and/or $\cos\theta$ do not vary with time so that the stored momentum as expressed by Equation (75) and Equation (76) can be evaluated by taking the volume integral only.

The previous Bloch-ring example can be easily calculated using Equation (76). The spatial integral of $\psi\vec{\nabla}\cos\theta$ across the wall gives $2\psi$ times the area with the direction normal to the wall surface in

the increasing $M_z$ direction, where the variation of the $\psi$ in the wall normal direction is neglected (see Section 1.3.9). The precession angle $\psi$ changes by $\pi$ when the ring passes by. So, we have

$$\Delta\vec{P} = (2\pi M_s/|\gamma|)(\vec{A}(t_2)-\vec{A}(t_1)) \tag{78}$$

which is the same as Equation (73).

2.2.13 Inplane Pulse Field on a 1-D Planar Wall

Consider an application of the momentum concept to a case without involving the Bloch-lines. Wall motion caused by a strong inplane pulse magnetic field has been observed experimentally [12]. No conventional forces are involved in the drive of this experiment. The motion can be understood in terms of the gyrotropic force or the momentum.

Without the presence of an inplane field or an inplane anisotropy, the wall will be a Bloch-wall with $\psi$=0 or $\psi$=$\pi$ to lower the demagnetizing energy (Section 1.3.9). Assume that initially $\psi$=0. After the inplane field $H_y$ is applied normal to the wall, the stable precession angle, $\psi'$, will be $\psi' = \sin^{-1}(H_y/8M_s)$ if $H_y<8M_s$ or $\psi=\pi/2$ if $H_y\geq 8M_s$. Using Equation (63a) and Equation (64b) for a planar wall, the precession of $\psi$ from 0 to $\psi'$ will result in a $\dot{\psi}$. This $\ddot{\psi}/\gamma$ is a gyrotropic force and causes the wall to move.

The total stored momentum change per unit wall area as $\psi$ changes is $2M_s \sin^{-1}(H_y/8M_s)/|\gamma|$ while the momentum dissipation through damping is $-D_{nn}\Delta y$. So, conservation of the momentum gives

$$2M_s \sin^{-1}(H_y/8M_s)/|\gamma| = -D_{nn}(\Delta y)$$

$$= 2\pi M_s \alpha(\Delta y)/|\gamma| \ell_w \quad . \tag{79}$$

The total displacement of the wall is, therefore, $\ell_w \sin^{-1}(H_y/8M_s)/\alpha\pi$.

2.2.14 Summary

Gyrotropic force, undetectable in steady state wall motion, has shown to be significant as the steady state wall motion breaks down. Twisted walls or Bloch-line structures, unapparent statically in the bubble materials, can cause a huge gyrotropic drag to retard the wall motion when deflected in the wall. Momentum storage in the form of the static spin structure, a motionless system, provides a new understanding on the remnant effects of the magnetic materials.

# Chapter 3

# Gradient Translation of Magnetic Bubble Domains

## 3.1 Introduction

### 3.1.1 Gradient Propagation Experiment

Gradient propagation of isolated magnetic bubbles is a popular method for bubble device material characterization. It was first proposed by Vella-Coleiro, et al [1] as an alternative to the bubble collapse method [2,3] for the routine characterization of bubble materials. Both methods attempt to measure the dynamic, rather than static, character of bubble domains and hope to relate the measurement to the operating frequency of a propagating device that might ultimately be made from the same material. Compared to the bubble collapse experiment, gradient propagation offers the advantage that the effective drive on the bubble is more constant and that the motion is more closely related to that experienced in a device. Other methods, such as radial expansion [4] and stripe head propagation [5] also exist but lack popularity because of the more sophisticated equipment necessary, in the case of the former, and the newness of the proposal, in the case of the latter. The popularity of the gradient propagation method alone would justify continued investigation into the details of the dynamics of bubbles in a gradient field; however, Malozemoff et al [6] recently found that bubbles moving in a gradient field continue to move even after the gradient pulse is turned off.

This overshoot in translation as well as related bubble translation that occurs without an applied gradient field are the subjects of the present chapter.

In the gradient translation experiment, a pulsed bias field gradient is generated by pulsing current through a pair of parallel conductors spaced 100-200 μm apart. A constant gradient bias field can be generated near the center of the parallel conductors. The magnitude of the field gradient changes less than 10% within a reasonable (15-35 μm) working area. The Zeeman force experienced by the bubble in the gradient field causes the bubble to move. As the bubble moves down the field gradient, it will experience a reduction in the bias field and expand. In order to remove this undesired radial motion and keep the drive force on the bubble constant during the translation, a linearly-rising spatially-uniform bias field compensation pulse is used. In the popular method used by others, the velocity of the bubble is obtained by dividing the total distance travelled by the bubble by the gradient pulse width used.

For wall velocity measurements, the ideal situation is to have a constant drive on the wall for an easily detectable distance, since this is the simplest situation which can be solved theoretically. As was pointed out by Cape [7] and Vella-Coleiro [8], the drive for bubbles in gradient translation is more constant than in radial motion experiments. For the latter class of experiments the effective drive changes considerably for a noticeable motion due to the changing demagnetizing

field as the size of the bubble changes. A typical value for this drive change for 6 μm bubble material is about 6 Oe per micron of radial wall displacement. This change in drive is even more significant in the expansion or contraction of the width of stripe domains. For typical materials about 15 Oe per micron of wall displacement for an isolated stripe and about 25 Oe/μm for periodic stripes can be expected. In the single straight wall experiment [9], due to the strong bias gradient field needed to stabilize the wall, the effective drive change is about 3 Oe per micron of wall displacement. The effective drive field on the bubble in the gradient translation experiment is a function of the bubble size and the magnitude of the field gradient, therefore, not a function of the displacement explicitly. With proper bias compensation, bubbles can be translated for 35 μm with less than 10% change in drive field. This corresponds to a maximum drive change of .02 Oe/μm. Properly done, the gradient experiment is the most appropriate one for studying the steady state motion of the magnetic domain walls.

### 3.1.2 Deflection Angles and Bubble States

Gradient translation of bubbles at angles to the gradient was first observed by Vella-Coleiro *et al* [10] in near perfect liquid phase epitaxy (LPE) garnet films. Bubbles were found to translate at certain angles, both left and right, to the field gradient direction. Such bubbles had not been observed in orthoferrites and rarely in bulk-grown garnet platelets. Slonczewski *et al* [11] studied low damping LPE films and observed a pronounced quantization in the deflection angle.

This strange dynamic behavior was attributed to vertical Bloch lines [11,12]. The quantized angles were explained by assuming a different number of the VBL pairs in the bubble. A simple and compact force formulation was made later by Thiele [13,14], where the deflection was described in terms of the gyrotropic effect of the wall structure.

The analysis showed that the unichiral bubble, i.e., the bubble with a pure Bloch wall, translates at the first discrete angle whereas the bubble with one pair of clockwise winding VBL's translates along the gradient direction. Due to the curvature of the wall, unichiral bubbles have a nonzero gyrocoupling vector which is equivalent to a pair of counterclockwise winding VBL's. It, therefore, translates at an angle to the gradient. Bubbles with one pair of clockwise-winding VBL's have zero net gyrocoupling vectors and move along the gradient direction. In orthoferrite bubble films, due to their strong inplane anisotropy, all bubbles have a wall structure equivalent to that of a bubble with one pair of clockwise winding VBL's, hence, there is no net winding in the wall. The absence of the deflection angle for bubbles in orthoferrites is, therefore, understandable in terms of VBL models. The knowledge that a strong inplane anisotropy in orthoferrites can suppress VBL's leads to methods for their suppression in other materials. Thin permalloy coated garnet films reported by Suzuki et al [15] showed only two types of bubble domains corresponding to the two lowest-number Bloch-line states. With proper dosage, ion-implantation will also suppress VBL's [16]. In practice, this method of hard bubble suppression is most popular. In implanted samples, all bubbles either

propagate along the gradient or at an angle, indicating that they are unichiral bubbles or ones with one clockwise-winding VBL pair.

This deflection property of bubbles made possible a new approach to bubble memories, called the bubble lattice file (BLF). Voegeli et al[17] proposed that information could be coded in the bubble utilizing the different wall states, i.e., different number of VBL's. Unichiral bubbles and bubbles with one pair of clockwise VBL's were found to coexist statically in both ion-implanted garnets with proper implantation dosage and permalloy coated garnets as reported by Hsu [18]. Controlled generation of these two types of bubbles was also reported. The coded bubbles are stored in a periodic lattice. The principal advantage of the BLF is the sixteen-fold increase in storage density expected when the fabrication process is the limiting factor in normal field-access devices. This type of device is still in the testing stage. All memory functions including data-in, lattice propagation, and data-out have been demonstrated on a single test device [19].

### 3.1.3 Translational Forces

The theoretical translational velocity was first predicted by Thiele et al [20]. The steady state velocity was obtained by balancing the external drive force with the dissipative force due to bubble translation. In a more general formulation, the forces involved in translation are the Zeeman force, gyrotropic force, dissipative force and coercive force. The Zeeman force is a special form of the reversi-

ble force as discussed in the second chapter.

The coordinate system chosen for the force formulation is shown in Fig. (3.1). The bubble translation direction is assumed to be in the direction $\hat{x}$. The angle $\phi'$, which is not necessarily zero, denotes the angle of the bias field gradient direction relative to the bubble translation direction. The radial outward direction is denoted by $\hat{r}$ and $\hat{\phi}$ is tangential to the wall in the increasing $\phi$ direction. The bubble is magnetized in the $-\hat{z}$ direction.

The local Zeeman force per unit wall area, in the presence of a pure bias field gradient across the center of the bubble, can be written as

$$\vec{f}_H = -2M_s r\vec{\nabla}H_z\cos(\phi-\phi')\,\hat{r} \qquad (1)$$

The drive field experienced locally by the wall is $r\nabla H_z\cos(\phi-\phi')$. The total Zeeman force on the bubble is obtained by integrating the force density around the circumference of the bubble, i.e.,

$$\begin{aligned}\vec{F}_H &= \int_0^h \int_0^{2\pi} 2M_s r\cos(\phi-\phi')\,|\vec{\nabla}H_z|\,(\cos\phi\hat{x} + \sin\phi\hat{y})\,r\,d\phi\,dz \\ &= -2\pi M_s h\, r^2\,|\vec{\nabla}H_z|\,(\cos\phi'\hat{x} + \sin\phi'\hat{y}) \\ &= -2\pi M_s h r^2\vec{\nabla}H_z \quad , \qquad (2)\end{aligned}$$

where h is the thickness of the film.

The dissipative force due to wall translation can be calculated by noting that the dissipative dyadic, Equation (2-17b), can have a value only in a direction where $\nabla\theta$ or $\nabla\psi$ is not zero. For the planar wall

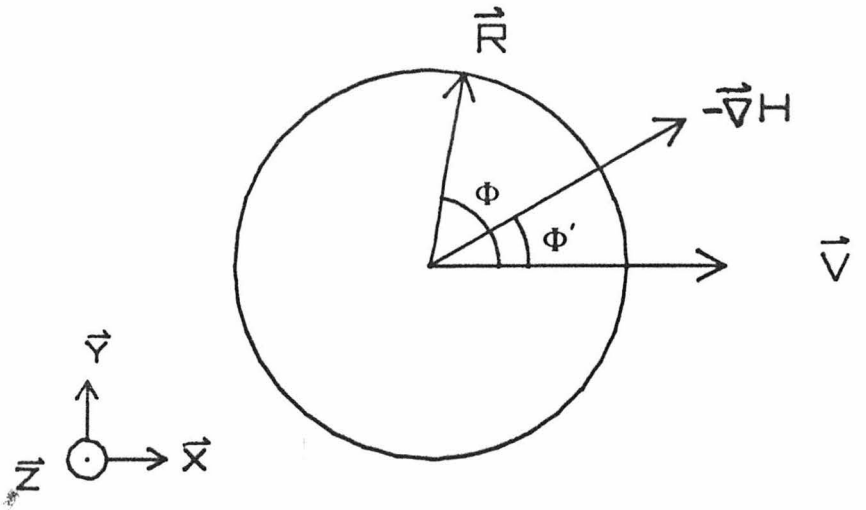


Fig.(3.1) Coordinate system for translational force formulation.

discussed in Section 2.2.8, the dissipative dyadic has only one nonzero term, which is the one in the direction normal to the wall. For bubbles with a simple Bloch wall structure, i.e., the unichiral bubble, $\vec{\nabla}\psi$ is not zero due to the curvature; however, it is normally neglected. Justification for this comes from estimating the relative size of the term. The term $\vec{\nabla}\psi$, of the order of $1/r$, is about 40 times smaller than the $\vec{\nabla}\theta$ term, which is in the order of $1/\ell_w$. As defined earlier in Section 1.3.2, $\ell_w$ is the wall width parameter. The dissipative force for bubble walls then can be approximated by that for the planar wall. The force direction, which is always normal to the wall, varies along the circumference of the bubble. For bubble translating in the x direction, the local dissipative force per unit wall area can be written as

$$\vec{F}_\alpha = -2M_s\vec{V}_n/u_b = -2M_sV_x\cos\phi/u_b\,\hat{r}$$

$$= -2M_s(V_x/u_b)(\cos^2\phi\hat{x} + \cos\phi\sin\phi\hat{y}) \quad , \qquad (3)$$

where $V_n$ is the local velocity normal to the wall. The total dissipative force of the bubble is

$$\vec{F}_\alpha = -\int_0^h \int_0^{2\pi} (2M_sV_x/u_b)(\cos^2\phi\hat{x} + \cos\phi\sin\phi\hat{y})r\,d\phi\,dz$$

$$= -2\pi M_s rh(V_x/u_b)\hat{x} \quad . \qquad (4)$$

For bubbles with n vertical Bloch-line pairs, an additional dissipative force should be taken into account. This added Bloch-line dissipative force can be calculated using Equation (2.17a), Equation (2.30) and

Equation (2.31) to be

$$\vec{F}_{\alpha} = 2n(-4M_s\alpha V/|\gamma|Q^{1/2})h \quad \hat{x}$$

$$= -8n(M_s h\alpha V/|\gamma|Q^{1/2})\hat{x} \quad , \qquad (5)$$

where h is the thickness of the film and is also the length of each Bloch line. As pointed out earlier in Section 2.2.7, the Bloch-line dissipation is normally much smaller than the domain wall dissipation except when the Bloch-line number is high and the Bloch lines are tightly packed. For bubbles with few Bloch lines, this Bloch-line dissipative force is negligible except in determining the circulating speed of the Bloch line as discussed in Section 2.2.11.

The coercive force is a phenomenological threshold in field resulting from the fact that wall motion does not continue for arbitrary small applied fields [21]. Detailed theoretical studies on the origin of coercive force have been made by others[22], but very little is really understood at this time. Here, the coercive force will be treated as a constant drag field, $H_c$, which tends to retard the wall motion independent of the wall velocity. This assumption results in a force

$$f_c = -2M_s H_c \hat{r} \qquad (6)$$

per unit wall area. For bubbles in translation the overall coercive force is then

$$\vec{F}_c = -2M_s \int_0^h \left( \int_{-\pi/2}^{\pi/2} H_c \cos\phi \hat{x}\, r\, d\phi + \int_{\frac{\pi}{2}}^{-\pi/2} -H_c \cos\phi \hat{x}\, r d\phi \right) dz$$

$$= -8M_s H_c r h \hat{x} \qquad (7)$$

The gyrotropic force for the steady state translation is most conveniently calculated from the gyrotropic vector as defined in Section 2.2.9. It is generally nonzero for a curved wall, hence, for bubbles. The gradient of the azimuthal angle of the spin, $\nabla\Psi$, due to the curvature of the bubble wall, is $\hat{\phi}/r$. The G vector of the curvature of the wall without Bloch-lines is obtained by using Eq. (2-19):

$$\vec{G} = (M_s/|\gamma|) \int_0^h \Delta \cos\theta \Delta\psi\, \hat{z}\, dz$$

$$= (2\pi M_s |\gamma|) h\, \hat{z} \qquad . \qquad (8)$$

where the magnetization inside the bubble is assumed to be "down", in the $-\hat{z}$ direction. For a bubble with n pair of counterclockwise-winding VBL's, the total gyrotropic vector of the bubble can be obtained by adding the Bloch-line G-vector, given in Equation (2-34), to the G-vector of the curved wall, given in Equation (8). The result is

$$\vec{G} = (n+1) \cdot (4\pi M_s/|\gamma|) h\, \hat{z} \qquad (9)$$

The total steady state G force of the bubble in translation can now be written as:

$$\vec{F}_g = (n+1)(4\pi M_s/|\gamma|)h\ \hat{z} \times V_x\hat{x}$$

$$= (n+1)(4\pi M_s/|\gamma|)hV_x\ \hat{y} \quad . \tag{10}$$

The total force equation for bubbles in translation is written as

$$\vec{F}_H + \vec{F}_g + \vec{F}_\alpha + \vec{F}_c = 0 \tag{11}$$

where $\vec{F}_\alpha$ and $\vec{F}_c$ are parallel to the velocity direction and $\vec{F}_g$ is normal to the velocity. The gyrotropic force will be zero when n is -1,corresponding to a bubble with one pair of clockwise-winding VBL's. For this bubble, all forces given by Equation (11) are colinear so that

$$2\pi M_s rh(-r\vec{\nabla}H_z - (4H_c/\pi)\hat{x} - (V_x/\mu_b)\hat{x}) = 0 \quad . \tag{12}$$

The translation of this type of bubble is in the direction of $-\vec{\nabla}H_z$, which is the $\hat{x}$ direction,so that

$$-\vec{\nabla}H_z = -\nabla H_z\ \hat{x} \quad , \tag{13}$$

where $\nabla H_z$ denotes the modulus of $\vec{\nabla}H_z$. The velocity can be calculated from Equation (11) and (12) to be

$$\vec{v} = V_x\hat{x} = [-r\ \nabla H_z - (4/\pi)H_c]/\mu_b\ \hat{x}$$

$$= (\Delta H - H_c')/\mu_b\ \hat{x} \tag{14}$$

where

$$\Delta H = -r\ \nabla H_z \quad , \tag{15}$$

is the effective applied field on the bubble, and $H_c'$ is

$$H_c' = (4/\pi)H_c \tag{16}$$

the equivalent coercivity for translational motion. Choosing the effective drive field in this way gives an equation in the same form as that of the planar wall case when the same mobility is used.

The more general force equation for bubbles, where the G-vector is not necessarily zero, is obtained by substituting Equation (2), (4), (7) and (10) into Equation (11). For the general case, the force equation becomes

$$2\pi M_s rh[\Delta H\cos\phi' - (V_x/\mu_b) - H_c'] = 0 \tag{17a}$$

$$2\pi M_s rh[\Delta H\sin\phi' - 2(n+1)(V_x/|\gamma|r)] = 0 \quad . \tag{17b}$$

An expression for the deflection angle of the bubble with the number of the VBL's as a parameter, can be obtained from Equation (17b):

$$\phi' = \sin^{-1}[2(n+1)V_x/|\gamma|r\Delta H] \quad . \tag{18}$$

This expression is generally used instead of a more general solution that does not include the translation velocity $V_x$ because both the translational velocity and the deflection angle can normally be measured at the same time during the experiment. In addition to this, the expression in Equation (18) does not depend on the coercivity explicitly, which is advantageous since usually the coercivity is not known.

The force equation can be solved algebraically for the translational

velocity as well as the deflection angle of Equation (17) with the coercivity as a parameter:

$$V_x = \{[\Delta H^2(1/\mu_g^2 + 1/\mu_b^2) - (H_c'/\mu_g)^2]^{1/2} - (H_c'/\mu_b)\} / (1/\mu_g^2 + 1/\mu_b^2) \quad , \tag{19}$$

where $\mu_g$ is an equivalent transverse wall mobility due to the G force of the bubble, defined as

$$\mu_g = -|\gamma| r/(2n+2) \quad . \tag{20}$$

If the coercivity is small compared to $V_x/\mu_b$, the translational velocity $V_x$ in Equation (19) can be reduced to a linear function of drive field:

$$V_x = \Delta H/(1/\mu_g^2 + 1/\mu_b^2)^{1/2} \quad , \tag{21}$$

with a reduced mobility of $1/(1/\mu_g^2 + 1/\mu_b^2)^{1/2}$. Unfortunately, for most garnet materials, the relatively low saturation velocity makes the ratio $V/\mu_b$ comparable to $H_c'$, so that the more complicated Equation (19) should be used instead of the simplified Equation (21)

The deflection angle equation deduced from Equation (17) is

$$\mu_g = \mu_b[\cot\theta' - (H_c'/\Delta H)\csc\theta']$$

or

$$n = -(\pi r\alpha/2\ell_{wo})[\cot\theta' - (H_c'/\Delta H)\csc\theta']^{-1} - 1 \quad . \tag{22}$$

The deflection angle can be obtained from Equation (22) for

an arbitrary number of Bloch-line pairs, n.

Notice that Equations (10) through (22) are based on the assumptions that the whole spin structure is translating at a steady state velocity, Bloch lines are motionless relative to the bubble and the added wall damping due to the presence of VBL's is negligible compared to the regular wall damping. If VBL's are in motion with respect to the bubble, an additional Bloch line gyrotropic force should be considered. For a bubble in translation, there is a location for VBL's on the bubble circumference where they remain stationary. This position is called the Bloch line riding point. It can be obtained from the force equation as was first pointed out by Thiele [14]. Since Bloch lines are confined in the wall, they can only move laterally. The Bloch line riding point is a location where the net Bloch line forces have no tangential component. The position of the Bloch line riding point which is at an angle $\phi_B^*$ to the propagation direction can be calculated from the condition that the tangential component of the sum of the Bloch line gyrotropic force and the dissipative force equals zero:

$$(\vec{F}_g' + \vec{F}_\alpha') \cdot (-\sin\phi_B \hat{x} + \cos\phi_B \hat{y}) = 0 \qquad (23)$$

Using the gyrotropic vector and the dissipative dyadic given in Equations (2-29), (2-30) and (2-31), the gyrotropic and dissipative forces for each vertical Bloch-line are

$$\vec{F}_g' = \pm 2\pi M_s h V/|\gamma| \hat{y} \qquad (24a)$$

and

$$\vec{F}_{\alpha}' = -4M_s h\alpha V/|\gamma| Q^{1/2}\,\hat{x} \qquad (24b)$$

where the positive and negative signs in Equation (24a) are used for counterclockwise and clockwise winding VBL's, respectively. Equation (23) reduces to

$$\tan\phi_B = \pm\pi Q^{1/2}/2\alpha$$

$$\text{or} \quad \phi_B = \pm\left[\frac{\pi}{2} + \tan^{-1}\left(2\alpha/\pi Q^{1/2}\right)\right] \quad . \qquad (25)$$

The angle $\phi_B$ for most low damping garnet samples where Q is high is very close to $\pi/2$. For the standard sample 2-16-44 used in this experiment, $\alpha$ is .026 and Q is 16 which give $\phi_B = 90.24^{o}$.

3.1.4 Translational Velocity and Remnant Effects

Confusion and nonreproducibility have been clearly evident in much of the early work on bubble domain wall velocities. Wall velocities obtained from the gradient propagation experiment and the bubble collapse experiment were first compared by Vella-Coleiro [23]. The velocity information obtained from the two experiments was different. A clear limiting velocity of 10 m/sec was observed in the collapse experiment. On the same sample, gradient translation results showed a velocity linearly increasing with drive field strength to 25 m/sec with no sign of a saturation velocity. As pointed out by Cape [7], variability in bubble translation was evident from pulse to pulse. Extensive measurements of the bubble translation velocity by Vella-Coleiro [24] in high mobility LuGd iron garnet epitaxial films showed a large scatter in velocity at high driving fields. Confirming results on this erratic

scatter in translation velocities were observed by Josephs et al [25], where they also showed more scatter exists when the bias field is near the DC stripe-out region, suggesting that the scatter might be caused by a stripe-out mechanism instead of the more complex dynamic conversion mechanism suggested by Vella-Coleiro [24]. Later a high speed photography study of gradient translation of the bubble, reported by Vella-Coleiro et al [26], showed the presence of the velocity scatter with no sign of bubble stripe-out. The results suggested a dynamic conversion of the bubble wall's spin configuration into a less mobile state when the translation velocity exceeded a critical value. Other peculiar observations were reported. Turning phenomena during sequential propagation was observed by Malozemoff [27] and Josephs et al [28]. Bubbles were found not to move back directly after the gradient pulse was reversed. Sometimes the bubble continued to move as it did in the previous gradient field after the reversal. Before settling down to the new propagation direction, bubbles propagating at angles to the gradient made turns with left- (right-) handed bubbles always turning to the left (right) of their original propagation direction.

To make gradient translation easier, a low frequency (60 Hz) bias modulation field, also called a tickle field, of about 2 Oe in magnitude was used by Rosier[29]. Since typical gradient field pulses that are used in translation experiments range from a fraction of a μsec to few μsec long, it is difficult to understand how superimposing such a low frequency bias modulation can cause any significant effect in gradient translation.

Ballistic overshoot of the bubble in translation was first ob-

served by Malozemoff et al [30] using high speed laser photography. Bubbles were found to continue to move after the gradient drive pulse was over. The true translational velocity of the bubble was found to be the same value as that obtained from the collapse experiment. The differences previously observed could be accounted for by the ballistic overshoot. It made the gradient propagation have a greater total displacement and hence a higher apparent velocity. A Bloch-curve winding model was used [31] to explain this ballistic effect assuming that momentum was stored in the form of stacking of Bloch curves.

Overshoot was confirmed by Vella-Coleiro[32,33], again using high speed photography; however, a different model was proposed to explain the observation. The study focused on the length (pulse width) of the translation. The average velocity was found to increase as the pulse width decreases, consistent with a high initial velocity seen in other experiments[34]. A correlation was found between the amount of driven motion and the amount of overshoot; however, the correlation did not appear at low drives. These results were interpreted in terms of a dynamic conversion model. This model is based on the assumption that the number of horizontal Bloch-lines (HBL's) that are generated varies from pulse to pulse. A similar overshoot was found below the threshold velocity for dynamic conversion, which was attributed to defects in the sample.

The discovery of ballistic overshoot made clear why confusion had existed between bubble collapse experiments and gradient propagation experiments. There was disagreement, however, over the mechanism on

of momentum storage. Only qualitative attempts to explain the other anomalies had been made. This chapter will present a detailed study of the gradient translation and relate it to a new vertical wall twist model.

### 3.1.5 High Speed Photography

Observation of transient domains was first done by Rossol [35], using a shuttered He-Ne laser to stroboscopically observe the dynamic bubble. The domains were propagated periodically around a closed path formed by a permalloy film T bar overlay. Observation of the domain was achieved by using an electro-optic modulator [36] to gate the He-Ne laser for a small fraction of the period of the motion. Due to the low light level, multiple exposure with a strobing rate of 20 kHz was used so that only the average dynamic shape of the bubble was observed. Random distortion could not be seen.

A slightly different technique was described by Vella-Coleiro [37] using a continuous light source and strobing the transient bubble motion by using a gated image intensifier tube. The image intensifier used provided an optical gain in the range of 10,000 to 20,000 which allowed a great control over the illuminating power. This technique is particularly useful for those samples where the magnetic parameters are strongly sensitive to temperature. The high gain of the image intensifier allows the experiment to be done in either a strobing mode or a single exposure sampling mode, but the resolution of the intensifier output is normally poor.

The transient shape of stripe domains in a bubble garnet was first photographed with a single high intensity laser flash by Morris et al [38]. Ten nanosecond long laser flashes were triggered at a specific time delay after the application of a magnetic field pulse. The true displacement of the domain wall at any instant after the onset of the magnetic field pulse could then be measured. A much more versatile high speed optical sampling microscope was developed for the dynamic measurements of bubble and stripe domains and was reported by Zimmer et al [39] and Humphrey [40]. Single 10 nanosec laser pulse illumination was used to photograph the transient shape of bubble domains during a magnetic field pulse. During such a short exposure, the motion of the domain wall is negligible ($<.3$ μm) for most garnet samples. The laser flash has been incorporated into an optical sampling microscope as part of a sampling system in such a way that time scans of the transient bubble shape are possible through a clock cycle, for bubbles in a field access device, or during translation, expansion or contraction of free bubbles. This system allows the observation of not only the transient position of the free bubble or stripe but also of the transient shape. This latter observation provides a method of probing the domain wall structure [41].

## 3.2 Experimental Apparatus

The optical sampling microscope consists of a pulsed laser,

a polarizing microscope, a movie camera or a video recording system, a sampling delay unit, current pulse generators, and a main trigger control unit. The experimental apparatus provides synchronized trigger signals to trigger both the laser and magnetic field pulses. A delay unit controls the relative time between the magnetic field and the laser light used to observe the transient shape of the bubble. The time of the laser flash is sensed by a fast PIN photo-diode. By controlling the delay, the laser can be set to flash at any specific time during or after the magnetic field pulse. Time scan sampling experiments can be done by increasing the laser delay systematically.

A block diagram of the optical sampling system using TV recording is shown in Fig. (3.2). The trigger amplifier, which is a custom-made main control unit, is initiated by the vertical synchronization signal of the TV camera or by the opening of the shutter of the movie camera if photographic recording is desired. The output from the trigger amplifier triggers the pulse generators and the sampling oscilloscope horizontal sweep as indicated. The sweep unit then triggers the laser, after adding a delay appropriate to the position in the sweep, instead of the vertical deflection sampling gate as is normally done. The Tektronix 3T77 sampling sweep unit is used here as the delay control unit. A portion of the light from the laser shines on a fast PIN photo-diode giving a pulse that triggers the vertical sampling gate coincident with the light pulse. The time of the laser flash can then be adjusted in relation to the applied field pulse by observing the field pulse on the sampling oscilloscope. Time sweeps of events can be taken by

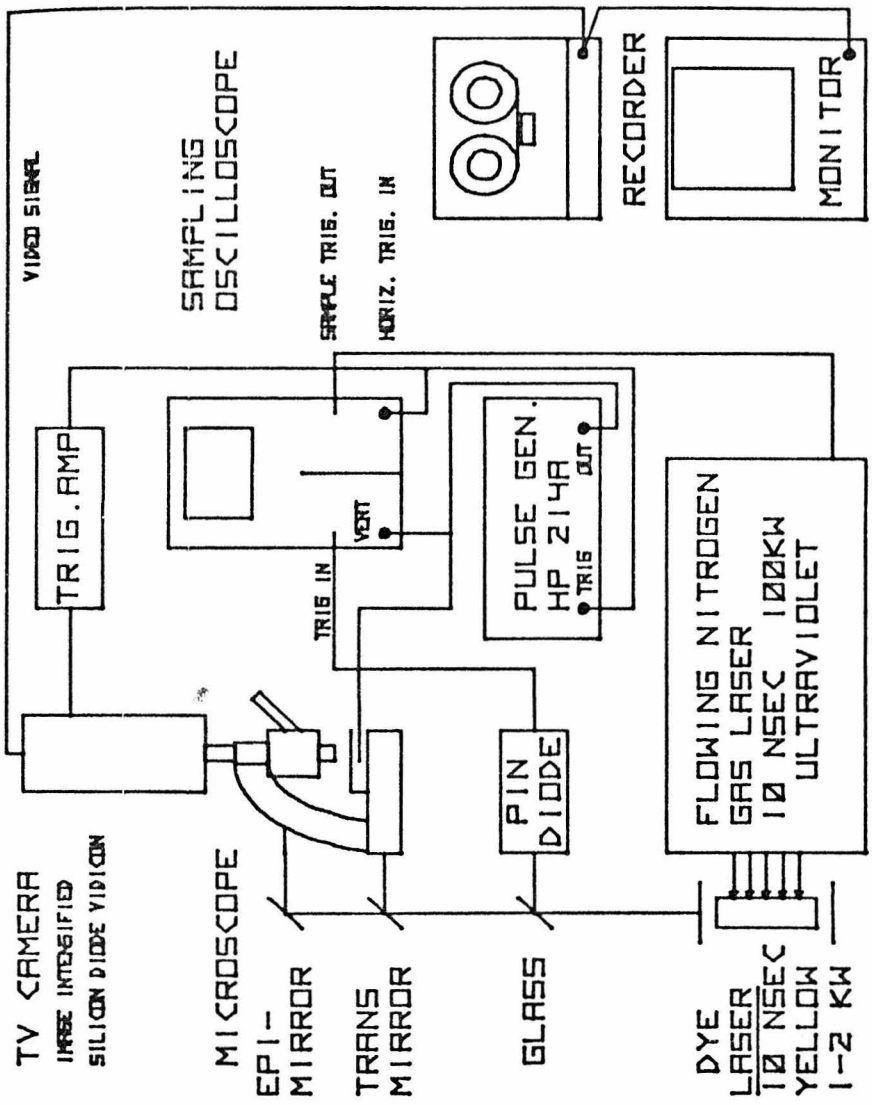


Fig.(3.2) Block Diagram of the Optical Sampling System

using the horizontal sweep generator of the oscilloscope and TV recording with each TV frame a single exposure of the transient bubble shape at that time.

The single 10-nsec laser flash is bright enough to expose Kodak 4X photographic film or to expose the Cohu 4400 silicon intensified target (SIT) TV camera, or for direct visual observation. The light source consists of two lasers, one pumping the other. A triggerable flowing-$N_2$ ultraviolet laser with 3371Å wavelength, 100 kw peak power for 10 nsec is used as a pump. The output of this Nitrogen laser is focused onto the dye cell of a Rhodamine 6G dye laser. The output from the dye laser has a peak power of about 1.5 kw. Rhodamine 6G was chosen because it is stable and has a high output at a convenient wavelength of 5800 Å. This wavelength has a relatively low absorption and high Faraday rotation for most bubble garnets. A standard Leitz Ortholux-Pol polarizing microscope with a long-focal-length x32/0.30 objective lens is used for the investigation. All of the lenses have been removed except the objective lens, eye piece, condenser, and a single lens before the eyepiece. A prism polarizer and sheet analyzer are used.

Magnetic field pulses are generated using HP214A current pulse generators driving a tiny bias field spiral coil or parallel conductor stripe lines. For uniform bias-field pulsing, a spiral coil with an inner diameter of 1 mm and five turns is used, which generates a uniform field with less than 1.5% variation across a 150 μm diameter viewing area. The gradient field is obtained from a pair of parallel evaporated copper stripe conductors with a 1 x 30

Table 3.1 Material Parameters of Garnet Films

| Sample Number | 2-16-44 | 2-12-63 | 206 |
|---|---|---|---|
| Composition | $Y_{1.57}Eu_{0.78}Tm_{0.65}Ga_{1.05}Fe_{3.95}O_{12}$ | | Ca, Ge |
| h (μm) | 6.8 | 6.9 | 4.1 |
| $4\pi M_s$ (G) | 184.4 | 205 | 180 |
| $\ell$(μm) | 0.87 | 0.93 | 0.77 |
| $H_{col}$ (Oe) | 90.5±0.2 | 95 | 72.7 |
| $H_k$ (Oe) | 3082 | 3399 | 1520 |
| $\gamma$(Rad/sec/Oe) | $1.1\times10^7$ | $1.1\times10^7$ | $1.83\times10^7$ |
| $\alpha$ | 0.026 | 0.029 | 0.14 |
| Implantation | no | $2\times10^{14}Ne^+/cm^2$ 80keV | unknown |

μm cross section and a 130 μm center to center separation, which gives a bias gradient field of about 8900 Oe/cm/amp. The rise time of the magnetic field pulses are about 7 nsec, which is mainly limited by the current pulse generator used. Current is monitored using a Tektronix CT-2 current transformer, which has a sensitivity of 1 mV/mA with response time of .5 nsec.

The characteristics of the garnet samples are listed in Table 3.1. The thickness of the films is measured by optical interferometry. The characteristic length $\ell$ and saturation magnetization $M_s$ are measured from the static bubble collapse field and bubble size measurements. The anisotropy field $H_k$, gyromagnetic ratio $\gamma$ and the Gilbert damping constant are measured by microwave parallel and perpendicular resonance. Unless otherwise specified, the film reported is the as-grown version of the 2-16-44 sample.

## 3.3 Observation of the Vertical Bloch Lines

### 3.3.1 Introduction

Chirality changes in the Bloch wall, called vertical Bloch lines (VBL), have been used to explain the extraordinary size and collapse field of "hard" magnetic bubble domains. Repulsion between the many VBL's inhibit the contraction of the wall area and result in a larger equilibrium bubble size and a higher DC collapse field. The first direct observation of VBL's was made by Grundy *et al*[42,43], using Lorentz electron microscopy on Co foil and $PbFe_{12}O_{19}$ films. Vertical Bloch lines were identified by the abrupt reversal in the image contrast along the domain walls, corresponding to a change in wall chirality. For magnetic bubbles in mixed rare-earth garnet

films, transmission microscopy is impossible, therefore, more indirect methods must be devised for the investigation of VBL's. For static bubbles, Suzuki et al [15] observed characteristic Bitter domain wall patterns near bubbles in permalloy-coated garnet films which were identified as arising from the VBL structure within the bubble. A much more versatile dynamic technique was used by Morris et al [41] by observing bumps in expanding or collapsing stripe domains in garnet material using high-speed sampling microscopy. These transient shapes were explained by the low longitudinal mobility of walls with VBL bundles that locally slowed sections of the moving wall causing a bump or indent to appear. Both left- and right-hand deflection VBL bundles, relative to the wall propagation direction, were reported.

For bubbles in translation, as shown in Section 3.1.4, the overall gyrotropic and damping force due to the presence of VBL's causes the bubble to skew with an angle

$$\theta' = \sin^{-1} 2(n+1)v/|\gamma| r\Delta H_z \qquad (26)$$

from the gradient direction, where n is the net number of VBL pairs in the bubble circumference, v is the translation velocity, $\gamma$ is the gyromagnetic ratio, r is the radius of the bubble, $\Delta H_z$ is the field difference across the radius. The gyrotropic force also tends to squeeze VBL's into clusters. The stable Bloch-line riding point is located on the bubble circumference at an angle

$$\phi_B = \pm[(\pi/2) + \tan^{-1}(2\alpha/\pi Q^{\frac{1}{2}})] \quad . \qquad (27)$$

from the velocity direction, depending on the sense of the VBL's, where $\alpha$ is the Gilbert damping constant and again $Q = H_k/4\pi M_s$.

Confirming experimental evidence was given by Pattern et al [44] using high-speed photography. They observed a transverse elliptical distortion of hard bubbles during the gradient propagation that indicated a hard wall section at the higher side of the gradient at about $90^{o}$ to the velocity direction.

### 3.3.2 Experimental Observation

In order to observe the effects of wall structure generated during gradient propagations, double-exposure photographs with a 10 nsec exposure time of a bubble at rest after a translation and at the end of a bias field expanding pulse are taken and shown in Fig. (3.3). The down gradient direction and the translation direction are indicated by arrows G and V, respectively. This particular bubble has a $40^{o}$ skew in the 2.9 Oe/radius, 1 μsec gradient pulse. Based on Equation (22), this bubble has 12 positive-winding VBL pairs. It can be seen that the geometric center of the bubble moved during the radial expansion. Some sections of the wall had a high radial velocity during the expansion than other parts of the wall. The direction of this shift in geometric center, transverse to the propagation direction, is reversed in Fig.(3.3b), where the direction of the velocity is reversed. Left skew bubbles always expand to the right (as in Fig. (3.3)) and right skew bubbles always expand to the left of the propagation direction. Symmetric expansion with no shift in geometric center was observed after a few expansion pulses.

The observed expansion shape can be explained by the clustering of the VBL's during the translation. The Bloch-line gyrotropic force

on the clockwise (positive) winding VBL's force them to cluster to the left of the bubble translation direction. During the expansion, the deflection of FBL's causes a gyrotropic force to slow the movement of the wall sections occupied by the VBL cluster. This velocity anisotropy causes the shift in geometric center during expansion. The symmetric expansion shape after the application of several bias field pulses shows that the VBL's are no longer clustered.

Low angle propagators, i.e., bubbles with zero or one pair of VBL's, typically expand symmetrically after propagation with a low drive field. However, if the gradient drive field is higher than a threshold, the bubble will develop a longitudinal asymmetry on expansion as shown in Fig. (3.4). During the uniform expansion pulse, the bubbles expanded much more rapidly in the original propagation direction than in the opposite direction and the flanks are pinned. Figure (3.4a) is typical such an expansion shape for a bubble that had previously translated at zero skew angle corresponding to one Bloch-line pair and Fig. (3.4b) for a bubble that translated at a small skew angle corresponding to the unichiral bubble. It can be seen that the axis of symmetry follows the propagation direction (indicated by arrow V). The pinning and asymmetric expansion shape disappeared after several expansion pulses.

The wall velocity for various parts of the bubble can be measured. For a bubble previously translated by a 15 Oe/radius pulse for .5 μsec and expanded with a bias field pulse of 45 Oe, the hard sections had a radial velocity of about 1 m/sec; this is the same velocity as reported

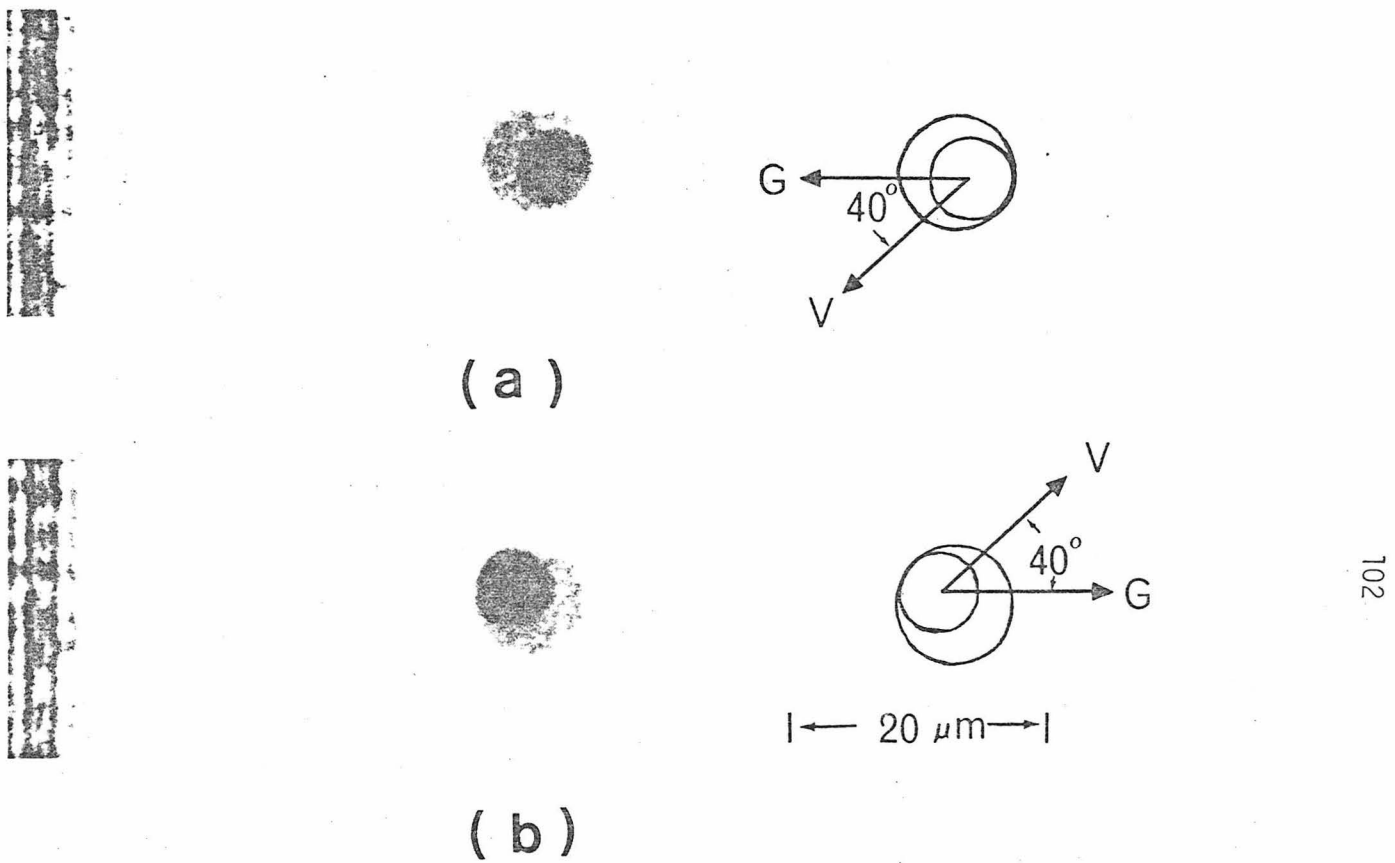


Fig.(3.3) Double-exposure photograph of magnetic bubble. First exposure (smaller) is static shape after the completion of a gradient field pulse of 2.9 Oe/radius, 1 μsec. Second exposure (larger) is the transient shape at the end of a bias field pulse of 20 Oe, 1 μsec. Arrows G and V indicate the previous (down) gradient and propagation directions, respectively. The black bars on the left are due to the light scattered from the edge of the conductor.

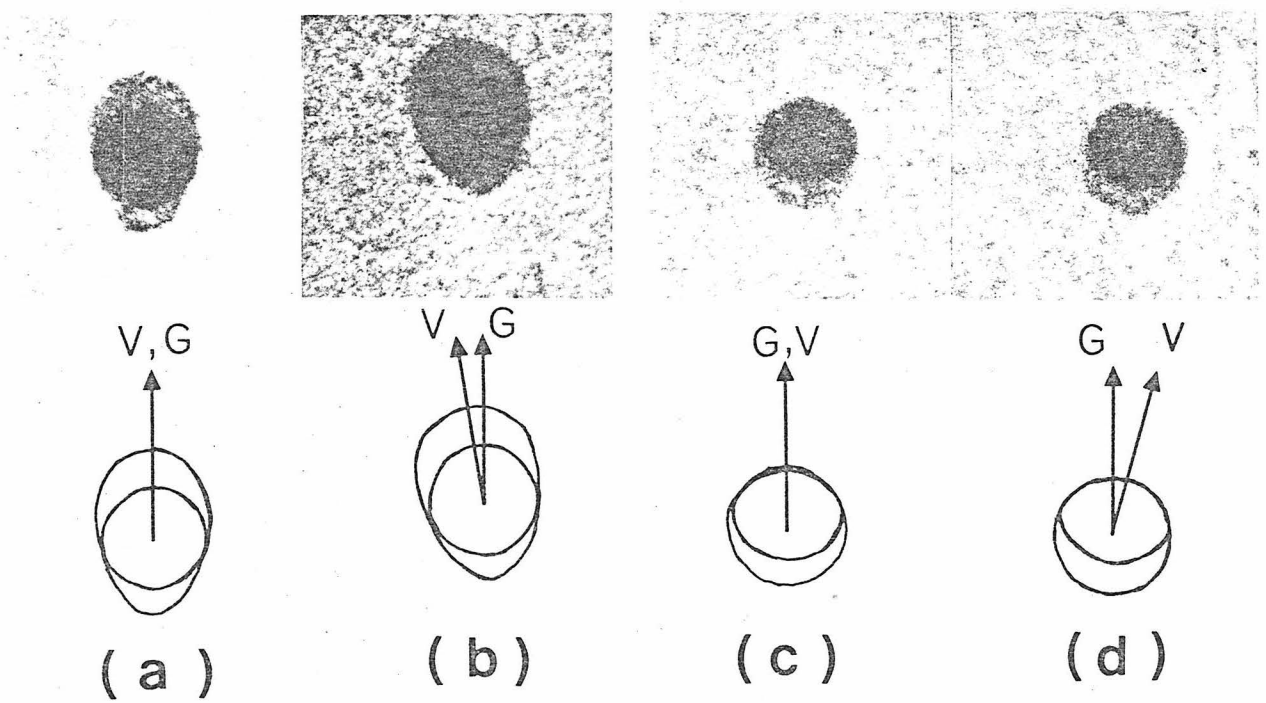


Fig.(3.4) Double-exposure photograph of magnetic bubble. (a) and (b) First exposure (smaller is the static shape after the completion of a high-amplitude gradient field pulse of 15 Oe/radius, 0.5 μsec. Second exposure (larger) is the transient shape at the end of a bias field expanding pulse of 20 Oe, 0.6 μsec. (c) and (d) First exposure (larger) is the static shape after the completion of a high-amplitude gradient field pulse of 15 Oe/radius, 0.5 μsec. Second exposure (smaller) is the transient shape at the end of a bias field collapsing pulse of 9 Oe, 0.6 μsec. Arrows G and V indicate the previous (down) gradient and propagation directions, respectively.

by Morris et al for a hard wall of a stripe domain. The velocities of the front and rear walls of the bubble in this case were about 7 and 4 m/sec, respectively.

Instead of an expansion pulse, positive bias-field pulses that tend to collapse the bubble were applied after the gradient propagation. Double-exposure photographs before and during the collapse pulse are shown in Fig. (3.4c) and (3.4d). It can be seen that the rear section moved faster than the front section and the two sides again appeared pinned. Fig. (3.4c) is typical of a bubble that translates along the gradient and Fig. (3.4d) is typical of one that translates at a small skew angle. Again, it is clear that the location of the hard and soft wall sections is related to the translation direction rather than to the gradient direction.

### 3.3.3 Discussion

The observation that low angle propagators have hard wall sections characteristic of high density VBL's leads us to conclude that VBL's of opposite sense are involved. As a result of the Bloch-line gyrotropic force during the translation, VBL's will cluster on the flank so that those clustering on the left must be positive and those on the right must be negative. When the expansion field is on, walls are pushed outward. The left- (right-) handed VBL's which are on the left (right) flank of the bubble will move to the left (right) of the radial direction, i.e., both VBL bundles move toward the rear of the bubble. The front wall section is free of VBL's and moves with a normal wall velocity. The rear section is initially free but then slows

as the VBL's move in. The two sides of the wall show a pinning until the whole VBL bundle has passed. Hence, most of the time during the expansion the pinned section of the wall is hard. For the collapsing pulse (Fig. 3.4c) and (3.4d), the radial motion is inward so that now the gyrotropic force drives both types of VBL's to the front. The rear wall moves fastest, resulting in the shapes shown in Fig. (3.4c) and (3.4d). This high density of VBL's of the opposite sense must be generated during the gradient propagation when the gradient field is high enough. They can be brought together and annihilated by bias field pulses.

## 3.4 Gradient Transient, Overshoot and Creep

### 3.4.1 Introduction

Free bubble gradient translation is very complicated because it must account for movement and changing structure within the wall as well as movement of the bubble domain. The experiments just discussed showed clearly that structure within the bubble wall will move and that this motion can affect the motion of the bubble domain. They also showed that opposite-winding vertical Bloch-lines are formed during translation. These observations must all be consistent with any model explaining gradient translation.

### 3.4.2 Experiment

Multiple and sequential single-exposure photographs of bubble domains were taken at various times during and after a gradient translation. To be compatible with the sampling optical microscope, experi-

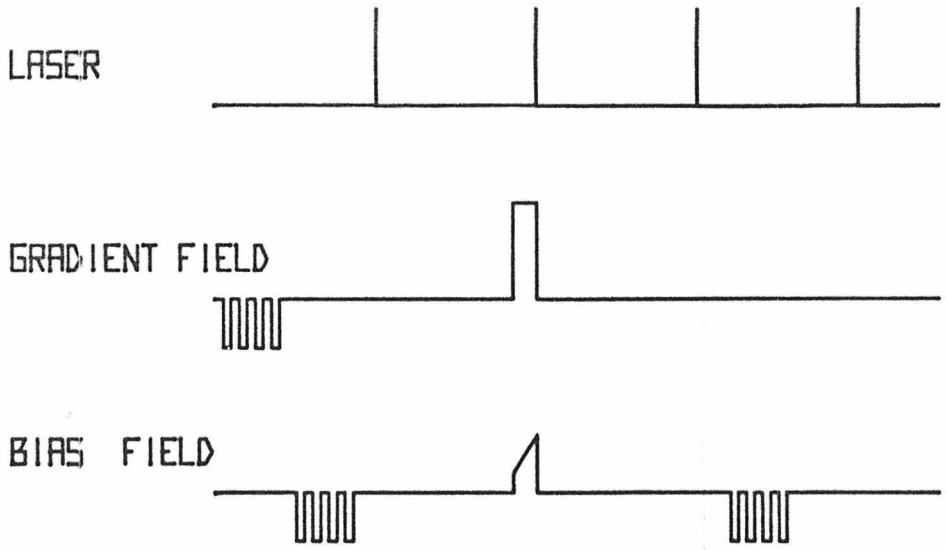


Fig.(3.5) Pulsing sequence for the sampling gradient translation experiment.

ments were done in a repetitive manner which required only one transient exposure per cycle. Typically, bubbles were first brought to the center of the gradient stripe lines by a series of weak, just above coercive limit, gradient pulses. Several uniform expansion pulses were then used to remove possible wall winding structure in the bubble. A single gradient field pulse was then applied with the bias compensation pulse (ramp pulse) synchronized to it. Several bias field pulses then followed. The bubbles were photographed before, at the end of, and then a long time (several seconds) after the gradient pulse and again after the bias field pulsing. This pulsing sequence is depicted in Fig. 3.5. If not otherwise specified, four 10-Oe, 0.5 μsec-long expanding bias field pulses were used as indicated. When the bubble displacement was large, such as for the high field gradient and/or long gradient pulse, multiple exposure photographs were taken. When the gradient field was low such that the driven displacement, overshoot, or creep were small, sequential single exposure photographs were taken and the different bubble locations were found by measuring from fixed points on the stripe conductor line. Generally, the translation was repeated 10 to 15 times with all parameters fixed; error bars will be found on the data that represent twice the standard deviation from the mean of these independent measurements. Where the error bar does not show, it is smaller than the symbol.

### 3.4.3 Results

Overshoot can be clearly seen by observing the bubble with high-

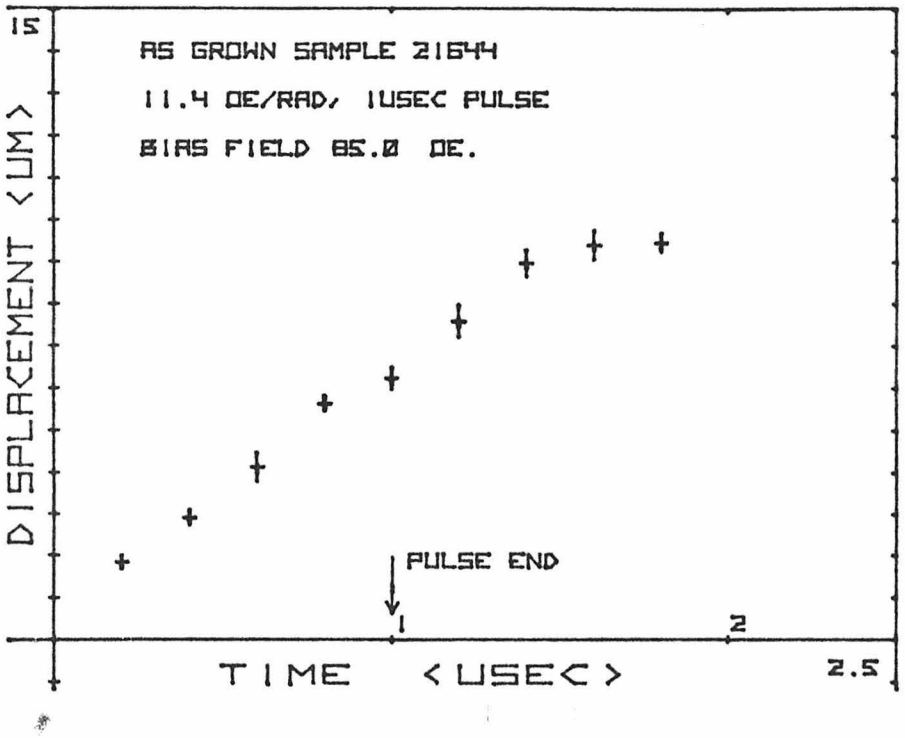


Fig.(3.6) Displacement of magnetic bubble center as a function of time after the application of an 11.4-Oe/radius 1-μsec gradient field pulse with an 85-Oe bias field. A 21-Oe peak 1-μsec-long linear-rise bias ramp pulse is used for the bias-field compensation.

speed photography during and after the application of a gradient field pulse. The transient position of the bubble as a function of time after the beginning of a 11.4 Oe/radius, 1 μsec-long gradient-field pulse is shown in Fig. (3.6). Bias compensation was provided by a 1 μsec-long, 21-Oe-peak linear-rise bias-field ramp pulse. The DC bias field was 85 Oe. It can be seen that the bubbles move in the gradient field and continue to move after the end of the gradient pulse with no apparent change in velocity even though there are no applied fields except the uniform DC bias field. This continued motion of the bubble is called overshoot. The slope of a straight line from the origin to each data point in Fig. (3.6) is the average velocity during that time interval. For the condition shown, the bubbles have an average velocity of about 9.2 m/sec in the first 200 nsec and then slow to about 5.8 m/sec until about 0.5 μsec after the termination of the gradient pulse. This translation velocity observed during most of the translation is the same as the saturation radial velocity obtained for the same sample. [39] Similar overshoot results have been reported by Malozemoff et al with the same consistency in saturation velocity between the bubble translation and the radial motion.

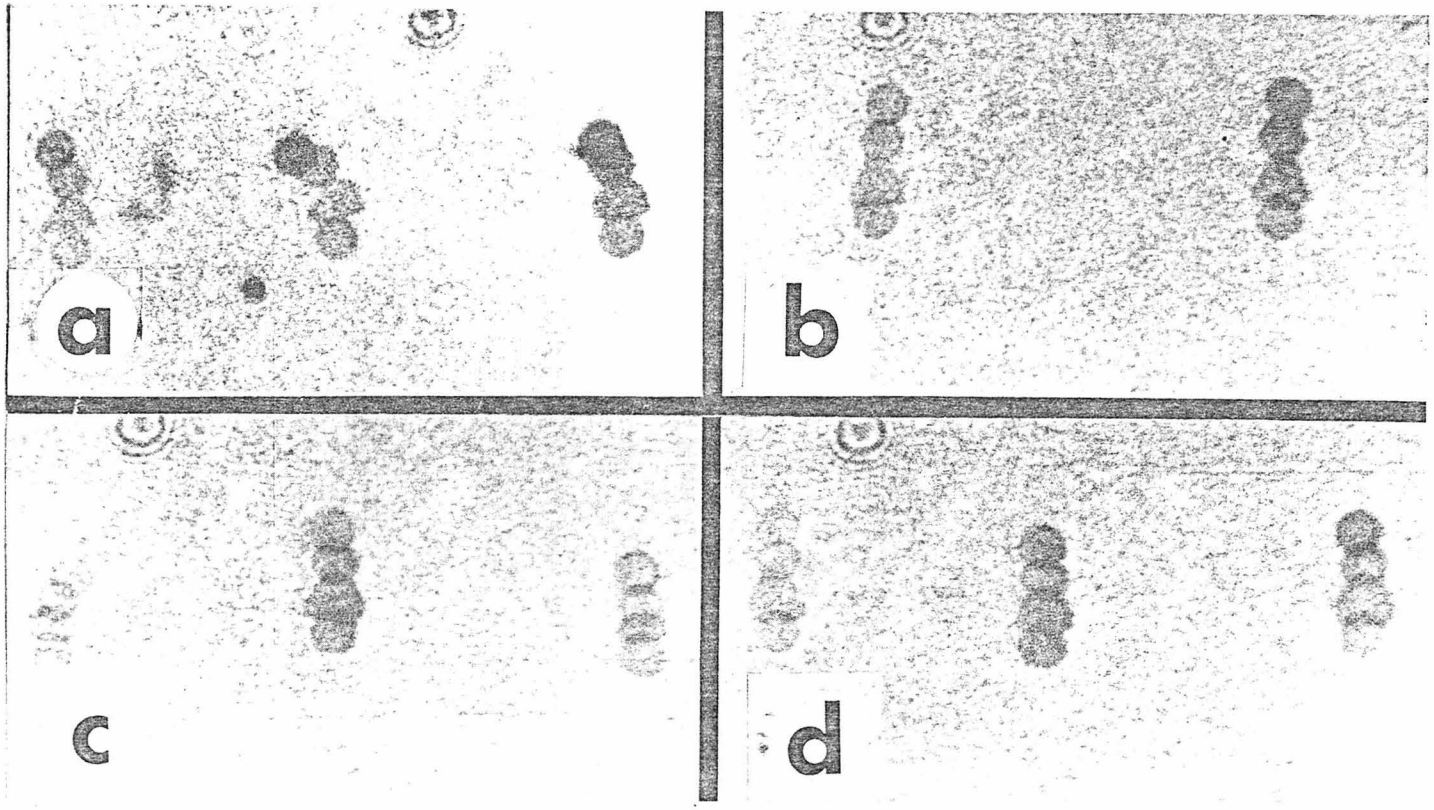


Fig.(3.7) Multiple exposures of bubbles being translated by (a) and (b) a 16-Oe/radius and (c) and (d) a 12-Oe/radius 1-usec gradient field pulse with a 75-Oe bias field. The four exposures are as follows: before the propagation (lowest), at the end of the gradient field pulse (second from the bottom), after overshoot (third), and after induced creep (top).

Transient pictures of the translating bubble are shown in the multiple-exposure photographs in Fig. (3.7). An exposure (the lowest in each picture)was made prior to the application of the gradient and compensation field pulse, another at the instant these two pulses are terminated, then, one well after (60 msec) the translation has stopped and, finally, after the application of a train of four uniform bias-field pulses. In this final train of pulses, each pulse has a magnitude of 10 Oe for 0.5 μsec and is in the direction to reduce the 75-Oe bias field, hence, temporarily expand the bubble. It can be seen that the bubble moves under the influence of the gradient pulse field and continues to move after the pulse is terminated. This is the overshoot referred to above. It is clear, however, that the four expansion pulses also result in a net translation. This latter motion is called creep. The amount of creep depends on the conditions of the previous translation, as will be discussed in the following. Figure (3.7) shows the total translational motion discussed here; however, for quantitative measurements, single rather than multiple exposureswere used to increase the measurement accuracy, and even greater bubble spacing was used to avoid mutual interteraction. The various sequences were chosen to illustrate the reproducibility, with Figs. (3.7a) and (3.7b) for a 16-Oe/radius gradient pulse. The direction of the bias field gradient is pointed from the bottom to the top of each photograph. The overshoot, however, can be either along the driven translation or at an angle to it. If it is at an angle, then the creep is also at an angle or,

more usually, at an even greater angle. For a slightly lower drive, as in Figs. (3.7c) and (3.7d), where the drive is 12 Oe/radius, the overshoot and creep is more usually in line, although not always, as can be seen in Fig. (3.7c) for the left-most bubble. The shape of the bubble (triangular) at the end of the translation pulse is a function of the length of the translation, magnitude of the gradient, and the perfection of the compensation. The shape here is typical of slight undercompensation for this translation. Other conditions yield even more complicated shapes, a result different from others who have reported that the transient bubble shape is always elliptical [45].

Translational creep as a function of the bias-field pulse magnitude is shown in Fig. (3.8). All motion shown is after a translation for 0.5 μsec in a 5.7-Oe/radius gradient field. Each propagation was made under as nearly the same conditions as possible so that only the effect of the magnitude of the 0.5 μsec bias-field expansion pulses were observed. A burst of at least six pulses was used. The number is twice that needed to induce all the translational motion (creep) from the bubble, so that the displacement indicated should be considered as the total motion that can be induced for that particular field. Creep exhibits a clear threshold, then increases rapidly to about 2.5 μm as the pulse amplitude increases from 1.2 to 5 Oe. For amplitudes greater than 5 Oe, the creep displacement is essentially constant. For bias field pulses lower than the threshold (1.2 Oe)

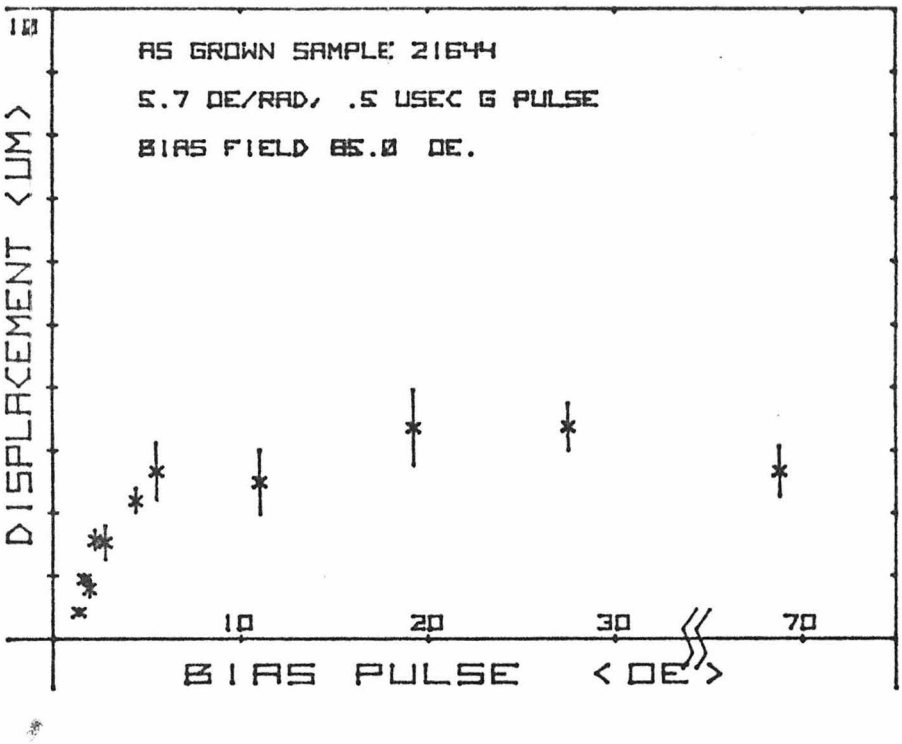


Fig.(3.8) Translational creep as a function of bias-field pulse strength for a bubble previously translated by a 5.7-Oe/radius 0.5-μsec gradient field pulse. More than six 0.5-μsec bias-field pulses were used to induce creep. The dc bias field is 85 Oe.

no observable creep can be observed even after many pulses. However, the bubbles still show the same ability to creep when the bias field pulse amplitude is increased above the threshold. For initial pulse field between 1.2 Oe to 5 Oe, the bubble does not creep more if the amplitude is subsequently increased, even though it would have moved further had the greater amplitude pulses been used initially (as shown in Fig. (3.8).) Since the creep is seen to "saturate", i.e., become essentially independent of the bias pulse amplitude, an amplitude well out into the saturation range (10 Oe) is used in the subsequent observations that relate creep to other parameters.

Total translational bubble displacement, including the displacement at the end of the gradient pulse after the overshoot and after the induced creep, is plotted as a function of the gradient field strength and is shown in Fig. (3.9). Single 1 μsec duration gradient field pulses were used during each propagation to translate bubbles from the center of the conductor stripe lines. The bias field at which the translation is done has a significant effect on the displacement, as can be seen by comparing Fig. (3.9a) and (3.9b), where two different bias fields, 85 and 75 Oe, were used. The displacement during the gradient field pulse is indicated by "+" and is about the same for the two different bias fields. It can be seen that the average velocity increases rapidly from 0 to about 3.4 m/sec when the bias field gradient changes from coercive limit, which is about 0.6 Oe/radius to 2.3 Oe/radius and then slowly increases to 6.5 m/sec for a drive of 16 Oe/radius. The general

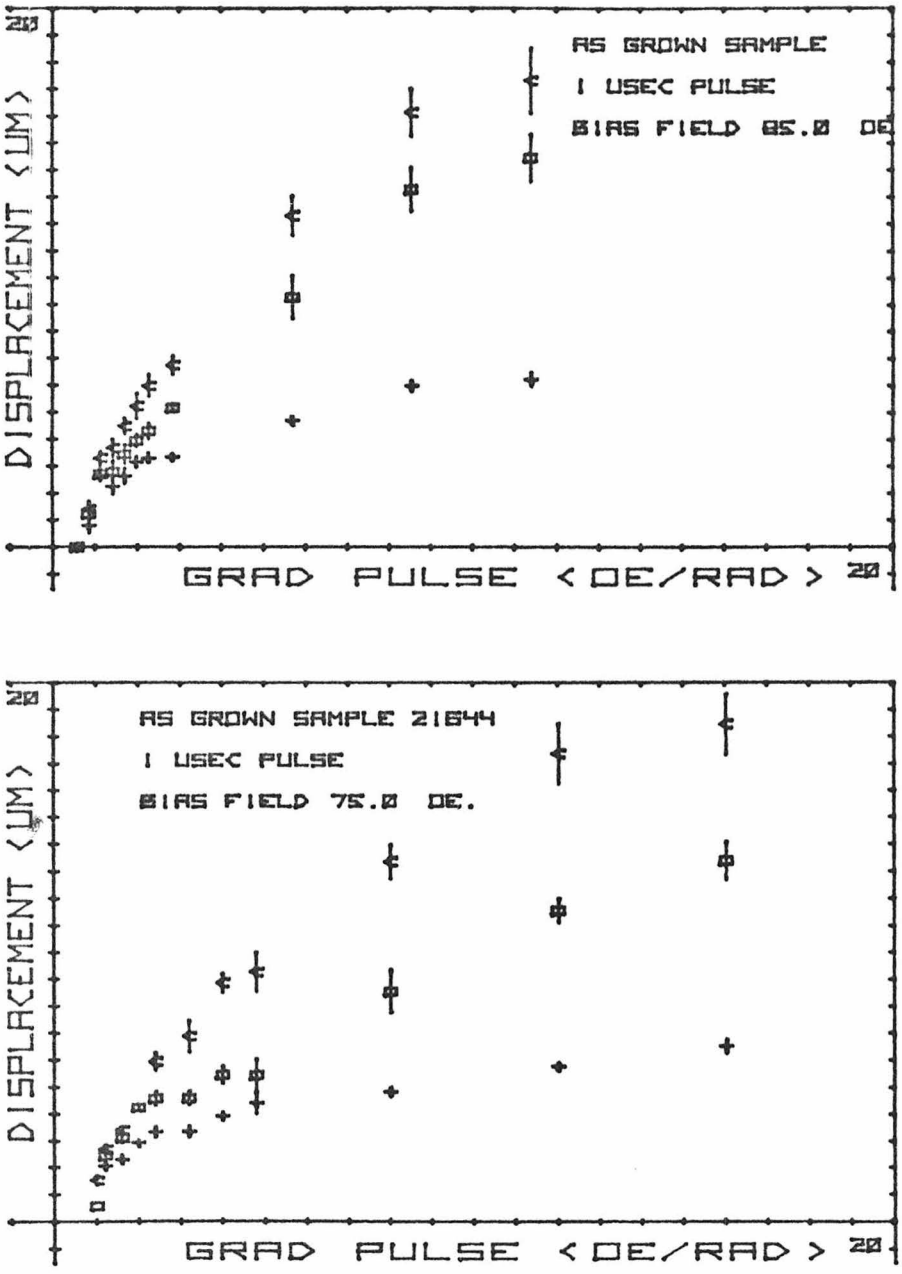


Fig.(3.9) Total translational displacement at the end of a 1-μsec-long gradient field pulse (+) after the overshoot (□) and after the induced creep (<) as a function of the gradient field strength with (a) an 85 and (b) a 75-Oe bias field.

character of the driven translation presented in Fig. (3.9) is similar to that observed by others [31,33] with the exception that the scatter from pulse to pulse is much less. Here, each point represents 10 independent translations, and the error bars represent twice the standard deviation from the mean. It is felt that the good reproducibility obtained here reflects the extra effort used in removing the creep ability so that the bubble is returned to its original state and in carefully repositioning the bubble so that the drive field condition will be nearly the same.

Overshoot and creep involve significant amounts of motion compared to the amount of the displacement during the gradient pulse, as can be seen in Fig. (3.9), where the displacement after the bubble comes to rest is indicated by "□" and after the bias field pulsing by "<". As can be seen by comparing Figs. (3.9a) and (3.9b) the total displacement as well as the displacement during the gradient pulse is essentially the same for the two different bias fields; however, the amount of the overshoot or creep is sensitive to the bias field. They seem to be closely related; one is the complement of the other. For fields greater than 5 Oe/radius, it can be seen that creep has reached a saturation value while the overshoot has not.

It is clear that the saturation creep is bias field dependent. The saturation creep is 3.3 and 5.5 μm for the bias field of 85 and 75 Oe, respectively. The ratio between the two is 1.6, while the ratio between the static bubble radii at these two bias fields is 1.68

Approximately, the saturation creep is proportional to the static equilibrium bubble circumference, about 0.9 μm creep per μm of circumference. The complementary relationship between the overshoot and the creep with the sum of the two appearing to be insensitive to the static bubble size for the various magnitudes of field gradient across the bubble indicates the close connection between the two phenomena. More momentum remained in the larger bubbles when they finally stopped after the overshoot, however, the total momentum generated in the bubble during the driven translation is independent of the bubble size.

The low gradient drive region was investigated in more detail using 3-μsec-long gradient pulses to obtain better accuracy. Displacement, including overshoot and creep, as a function of the amplitude of a 3-μsec gradient field pulse is shown in Fig. (3.10). The bias field is 85 Oe. The bubbles start to move when the drive is in excess of the coercive limit of 0.6 Oe/radius. The average velocity then increases linearly until the drive reaches 1.3 Oe/radius, where the average velocity seems to saturate at about 3.3 m/sec. The mobility measured for this drive interval is 4.7 m/sec Oe,which is only one-third of the theoretical mobility ($\gamma\Delta/\alpha$=12.5 m/sec Oe) using FMR $\alpha$. When the drive increases from 1.1 to 1.45 Oe/radius, the amount of the overshoot and creep relative to the displacement during the gradient pulse increases drastically from 10 and 2% to about 24 and 17%, respectively. The overshoot and creep continue to increase and reach 32 and 36% of the

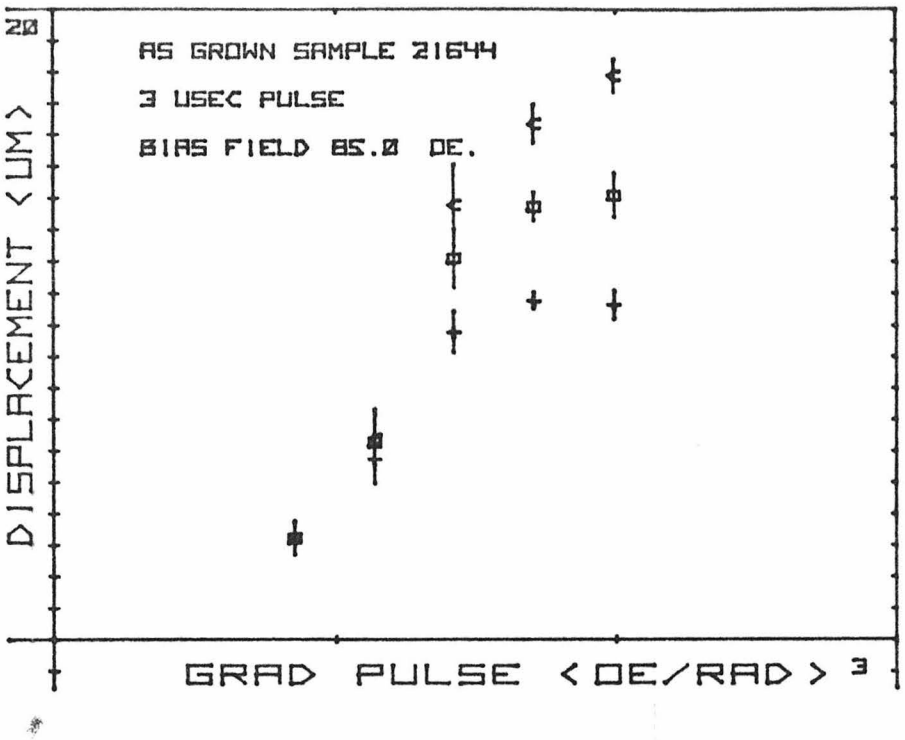


Fig.(3.10) Total translational displacement at the end of a 3-μsec gradient field pulse (+) after the overshoot (□) and after the induced creep (<) as a function of the gradient field strength.

displacement during the pulse when the drive reaches 2 Oe/radius.

The effect of pulse width on overshoot and creep for moderate gradient fields was investigated. Displacement as a function of gradient pulse width for a 4 Oe/radius gradient field amplitude was measured at 85 and 75 Oe bias field, and the results are shown in Figs. (3.11a) and (3.11b), respectively. It can be seen that the displacement during the pulse increases nearly linearly with the pulse width and is essentially independent of the bias field. Again, more overshoot and less creep were observed in higher bias fields, while the total displacement including creep seems to be independent of bias field. The complementary relationship between overshoot and creep discussed previously for 1- μsec pulses seems to be independent of pulse width at least for shorter pulses. The displacement per time of drive (average velocity) decreases slightly for pulses wider than 0.5 μsec. This observation is consistent with similar observations in the radial expansion on the same sample [4], however, it is not nearly the magnitude observed by Vella-Coleiro in a similar experiment with a higher mobility sample [33]. It can be seen that no significant increase in scatter during overshoot is observed over this range.

The effect of pulse width on overshoot and creep for higher gradient fields is shown in Fig. (3.12). Here, displacement as a function of gradient pulse width is shown for a gradient drive field of 11.4 Oe/radius and at bias field of 85 Oe. It can be seen that the displacement during the pulse increases linearly as it did in

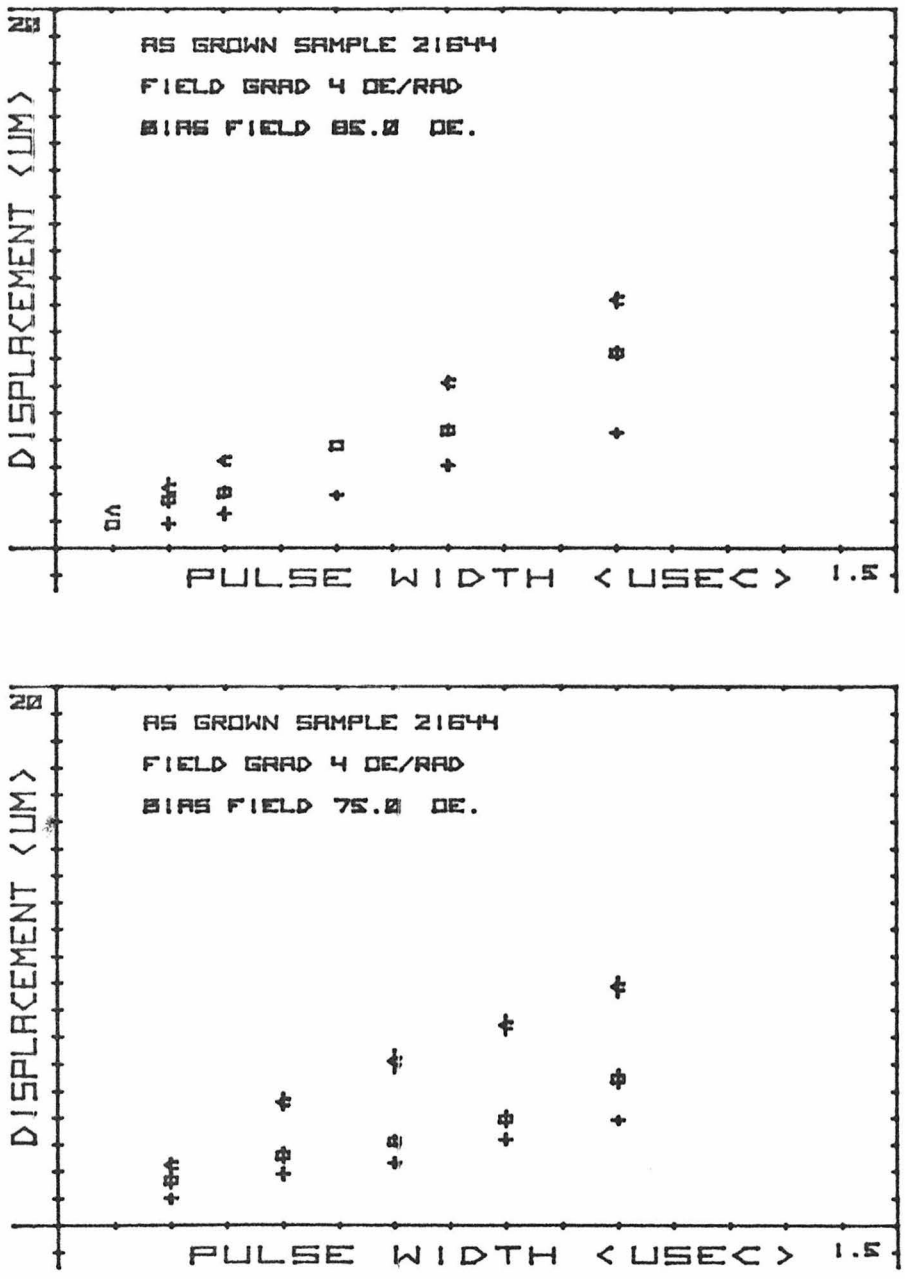


Fig.(3.11) Total bubble displacement at the end of a 4-Oe/radius gradient field (+) after the overshoot (□) and after the induced creep (⊂) as a function of the gradient pulse width for bias field equals to (a) 85 and (b) 75 Oe.

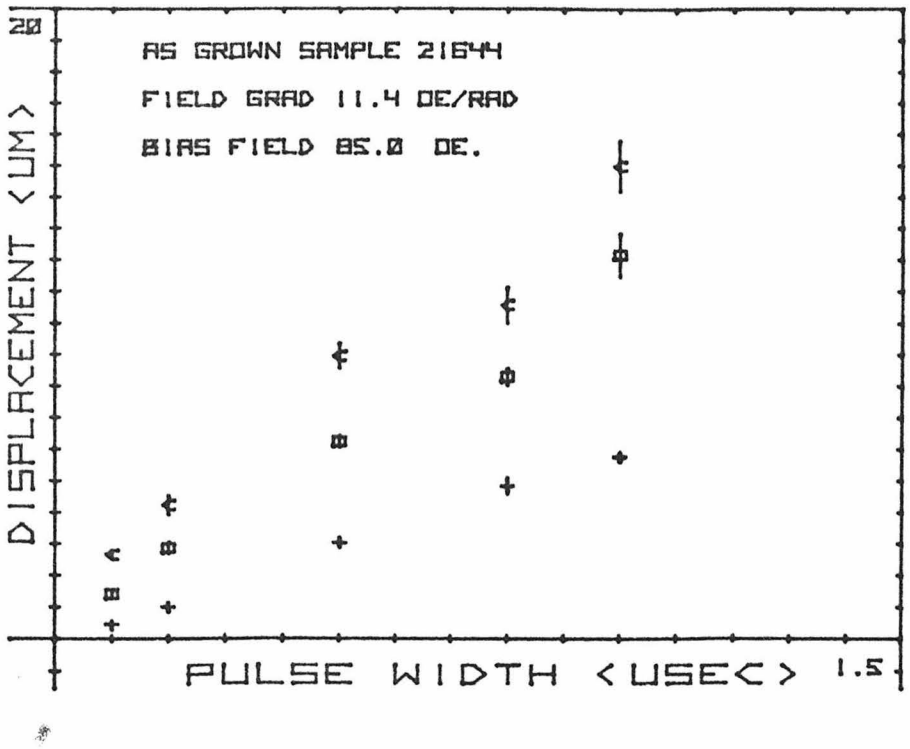


Fig.(3.12) Total bubble displacement at the end of an 11.4-Oe/radius gradient field pulse (+) after its overshoot (□) and after the induced creep (◁) as a function of the gradient pulse width with an 85-Oe bias field.

the lower drive case with an average velocity of 5.8 m/sec for all widths used. Creep reaches a saturation value within 0.5 μsec, as expected, with the same saturation value as in Fig. (3.9a). Overshoot, however, continues to grow and even seems to be growing more rapidly for the longer pulse. This characteristic is related to the shape of the bubble at the end of the pulse which is, in turn, related in a very sensitive way to the bias field compensation.

### 3.4.4 Discussion

A qualitative understanding of overshoot and creep will be presented here that is based on the assumption that a dynamic wall structure that is unstable statically is developed during translation. The dominant feature of this structure is vertical wall twists. Overshoot is a translational motion caused by the relaxation of this dynamic structure into a quasi-stable static structure. Creep is caused by further structural changes as the wall seeks its most stable static configuration. To be consistent with the preceding experimental results, such a model must provide a mechanism for overshoot as well as creep. It must account for the fact that overshoot is bubble size dependent. It must explain the complementary nature of the overshoot and creep. Finally the model must be consistent with the transient bubble shapes discussed earlier in this chapter. There, it was demonstrated that low-mobility hard wall sections exist in the bubble wall after a translation and that their location and the transverse motion in the film plane is consistent with the view that they are bundles of VBL's with opposite winding

sense. The model presented here provides that the wall structure at the end of the gradient pulse be dominated by these vertical wall twists, i.e., VBL pairs with each having a winding direction opposite from the other. This structure is packed by the gyrotropic force during the translation and relaxes after the termination of the pulse to give overshoot. Creep is the result of annihilating the remaining wall twists using bias field pulsing as the wall assumes its most stable state.

A convention is adopted here and presented schematically in Fig. (3.13). The magnetization direction inside the bubble is "down". For such bubbles in translation, the direction of the velocity is shown and the pulsed gradient field is in the same direction. For a bubble defined in this way, a counterclockwise or lefthanded vertical Bloch line (LBL) will be deflected to the left with respect to the wall velocity direction by the gyrotropic force. Similarly, a clockwise or righthanded VBL (RBL) will be deflected to the right. For a bubble containing LBL's, during the gradient propagation the local gyrotropic force of the Bloch lines will move the LBL's to the left flank of the bubble with respect to the wall velocity direction, while the overall gyrotropic force will deflect the bubble to the left of down gradient direction. For a bubble with RBL's, they will collect on the right flank as the bubble is deflected to the right. The direction of the azimuthal precession of the spin within the wall [46] at the front and the rear of the bubble is indicated. This direction is such as to ultimately generate LBL's on

the left and RBL's on the right. For equal number of LBL's and RBL's (vertical wall twists), the local gyrotropic force will move Bloch lines to the respective flank of the bubble with respect to the velocity direction, while the overall Bloch-line gyrotropic force on the bubble will be zero, leaving the bubble undeflected while moving in the down gradient direction.

The mechanism for the generation of vertical wall twists is the least understood part of the model that is presented here to explain the various modes of the translational motion available to the bubble. At least three different generation mechanisms, the Bloch curve model, the Bloch ring model, and the local Walker breakdown model [45], can be used to obtain the necessary vertical wall twist structure. The Bloch loop or Bloch curve model [47,31] was originally proposed to explain the saturation velocity for the uniformly driven straight wall. The static inplane gradient field through the thickness of the film at the wall, caused by the discontinuity of the magnetization at the film surfaces, creates a statically stable horizontal twisted structure for the wall [48]. For a bubble in translation, a nonuniform gyrotropic force proportional to the velocity in the wall normal direction will act on the horizontal twisted wall structure at the front and rear of the bubble. If the translation velocity is high enough, a horizontal Bloch-line will be created in the structure near one or the other film surface, depending on the chirality of the Bloch wall. As the driven motion proceeds,

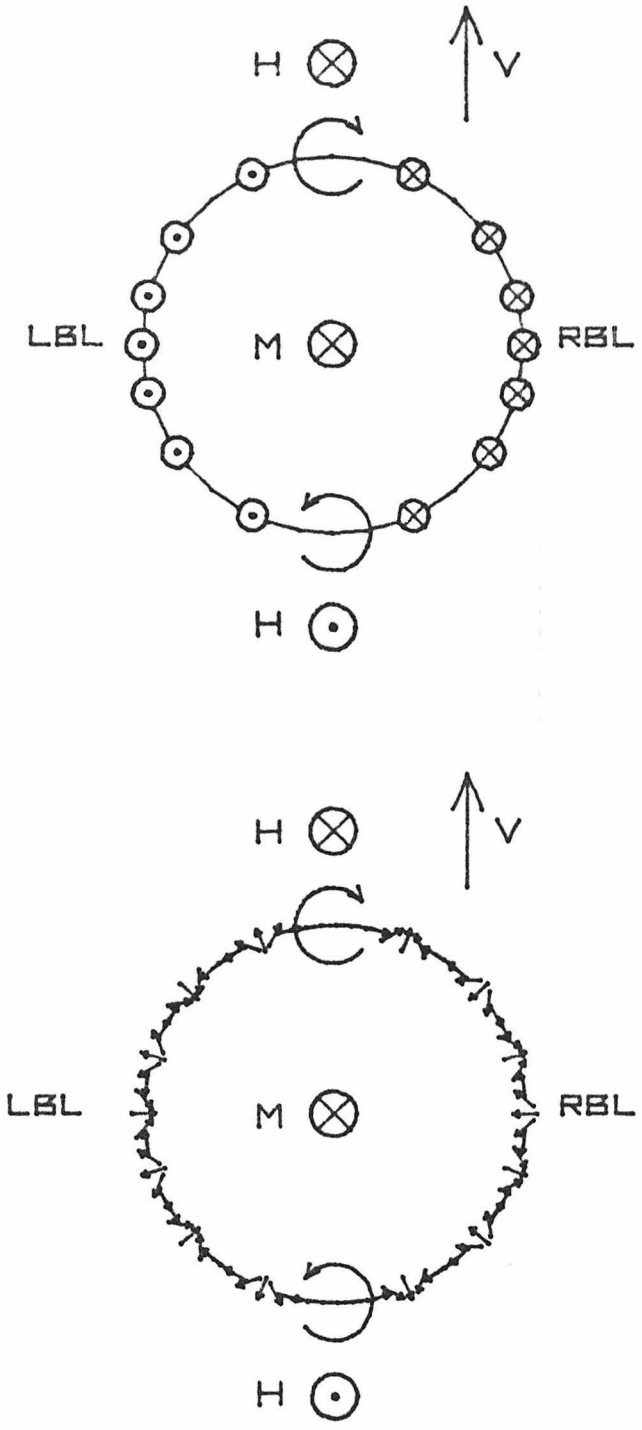


Fig.(3.13) Schematic of a bubble in translation with vertical wall twists.

the gyrotropic force on this nucleated horizontal Bloch line will move it toward the opposite surface. If the Bloch line gyrotropic force causes the Bloch curve to penetrate the opposite surface (punch-through), a pair of oppositely wound VBL's will result one on each side of the punch-through. After the punch-through of the old Bloch curve, the chirality of the Bloch wall is reversed and a new Bloch curve with an opposite sense will be generated at that surface and will propagate back. Punch-through of this new Bloch curve, now at the original surface, will result in another pair of oppositely-wound VBL's with the same winding sense as the previously generated VBL's. As the process continues, more and more vertical wall twists will be created.

The Bloch ring model [14] utilizes a defect to generate a ring Bloch line in the moving wall. The g-force acting on the ring will be in a direction either to expand or contract the ring, depending upon the sense of the twist of the ring with respect to the velocity. If the ring is in the proper sense to expand and if the local wall velocity is high enough to overbalance the Bloch line tension, the ring will grow in size. If the growth continues, eventually the ring will reach the film surfaces. Punch-through results in a vertical wall twist with the wall section between the opposite chirality. For this section of the wall, subsequent ring nucleation and expansion will result in a growing ring with the same winding sense as before. As the process continues, more vertical wall twists will be created.

The local Walker breakdown model [46] is based on a Walker type of oscillatory precession in the nonuniform field around the bubble circumference during the gradient pulsing. A nonuniform oscillatory precession along the circumference of the bubble will occur, where the magnitude of the pulsed field is locally higher than the Walker breakdown threshold. This condition, for gradient propagation, will first occur at the front and rear of the bubble where the pulse field is the largest and generally away from the film surfaces where the influence of the static stray field is the least. The sense of the precession at the front and rear of the moving bubble is shown in Figure (3.13). Large ring type structures will be generated and always with the proper winding sense so that they will grow. After some kind of punch-through at one surface to eliminate the horizontal parts of the ring (horizontal wall twists), the g force will move the RBL's into a bundle on the right flank and the LBL's into a bundle on the left, making room for continued precession to generate more and more vertical wall twists.

All three of the mechanisms discussed above generate the necessary vertical wall twists. They all generate the same sense of winding structure with RBL's on the right flank and LBL's on the left. They all predict the clustering of the VBL's to leave room for further VBL generation. They all have similar uncertainties involving the punch-through or penetration of the Bloch lines to the surface. All models predict thresholds in velocities and/or field for generation of the structure; however, the predicted values are different. The Bloch

curve model[4] predicts a velocity threshold of $V_p$ = 5 m/sec. at a field of 0.4 Oe. The local Walker breakdown model predicts a velocity threshold of $V_w$ = 30 m/sec and at a field of 2.4 Oe. The Bloch ring model predicts a velocity of threshold 48 m/sec. Experimentally, a very clear threshold is seen in Fig. (3.10) at a velocity of 3.3 m/sec and a threshold field of 1.3 Oe/radius. It can be seen that this threshold field is in better agreement with the Bloch curve model than the others, especially if the 0.5 Oe/radius static coercive force is added to the predicted value. The observed velocity clearly lies below the value predicted and well below the velocity threshold of the other models. Such a result indicates that the generation mechanism is much more complicated than any of the models, perhaps a mixture of them. Clearly, more study of the detailed mechanism for generation of the vertical wall twists is warranted.

A gyrotropic effective field can be associated with any spin rearrangement. For bubbles in translation, the important structures are those where the spin precession is in the azimuthal ($\dot{\psi}$) direction, resulting in a gyrotropic effective field $H_{gz} = -\dot{\psi}/|\gamma|$ that is in the $\hat{z}$ direction. Examples of this class of structural motion during the driven translation were considered previously, where the gyrotropic effective field was always in the direction to oppose the applied field. After the driven translation, the dynamic structures relax. For example, consider the vertical wall twists shown in Fig.

(3.13). As mentioned previously, during the translation, they will be packed into tight bundles on each flank of the bubble. During this process LBL's move left and RBL's move right until the g force is balanced by the repulsive force of the packed VBL's. Stated in field terms, as they move into a bundle, they generate an effective field that opposes the applied field, i.e., in the opposite direction to the gradient. When the gradient field is removed, the overpacked VBL's will relax, moving in the opposite direction, i.e., LBL to the right and RBL's to the left. The gyrotropic effective field for this spin precession will be in the direction to restore the original gradient. All of the wall structures, Bloch rings, HBL's and Bloch curves, can be considered in a similar fashion. If an applied drive field forces these structures into a condition of higher energy, as the structures relax back to their original state a gyrotropic effective field will be generated in the direction to restore the original drive.

Overshoot is a self-driven translation of the bubble caused by the spontaneous relaxation of statically unstable wall structures when the gradient field pulse is over. These structures must be of the kind discussed above, where the gyrotropic effective field for the spin precession upon relaxation will be in the direction to restore the original gradient field. The possible structures that contribute to the overshoot are Bloch curves, Bloch rings, overpacked VBL's, and excessive VBL's. Dynamically stable Bloch curves and Bloch rings will collapse due to the existence of the Bloch line tension, providing the necessary gyrotropic effective field for overshoot. Overpacked

VBL's will relax due to the Bloch line repulsion as discussed in the above example, also providing the necessary gyrotropic effective field. Excessive vertical wall twists will unwind at the front and rear of the bubble as the opposite-winding VBL's are pushed together by the VBL repulsion, providing the necessary gyrotropic effective field. In three of these four mechanisms, overshoot is provided by the collapse and the disappearance of the dynamically stable structure. In only one mechanism, overpacked VBL's, does the structure persist to record the history of the previous driven translation.

Creep is the bubble translation that is caused by the induced motion of the loosely packed vertical wall twists within the bubble wall. As was discussed in Section 3.3.3, it can be understood on the basis of low-mobility "hard" wall sections and the annihilation of vertical wall twists. The explanation can also be constructed within the framework of the gyrotropic effective field. At the end of overshoot, the VBL bundles on each flank will have expanded to an equilibrium spacing. The applied uniform bias field moves each bundle, as a unit and in the opposite deflection direction, because of the opposite twist direction of each bundle. Depending upon the direction of the bias field, both VBL bundles will move toward the front (collapsing pulse) or rear (expanding pulse), where the vertical wall twists will unwind. The gyrotropic effective field associated with this VBL bundle motion will reduce the applied field at that wall section occupied by the moving VBL's. This reduction of applied field means that the wall, locally, will move less; hence, it is ob-

served as a low mobility or hard wall section. As the VBL's move on each side, their distribution will become asymmetric between the front and rear and the gyrotropic effective field will cause a gradient field across the bubble, inducing translational motion. This gradient will be in the same sense as the previously applied gradient; hence, it will induce motion in the direction of the previous translation, independent of the polarity of the bias field pulse.

The bubble size dependence of the saturation creep can be understood in terms of stored gyrotropic momentum in the vertical wall twist structure. Opposite-winding VBL's are not stable and will tend to unwind when they are pushed together. The maximum statically stable VWT number can, therefore, be estimated. Using the closest uncompressed VBL separation calculated by Hubert [49], the maximum stored gyrotropic momentum is

$$\begin{aligned}\Delta P_g &= \sum_i (2\pi M_s/|\gamma|)\, Ai \\ &= (2\pi M_s/|\gamma|)\, h\left(4 \int_0^{\pi/2} \frac{r^2 \sin\theta d\theta}{\sqrt{2}\, \ell_{\ell 0}}\right) \\ &= 8\pi M_s r^2 h/|\gamma|\sqrt{2}\ell_{\ell 0} = 8M_s rh(\gamma/\sqrt{2Q}\ \alpha\mu_b \qquad (26)\end{aligned}$$

where the total VWT is $n\pi$ with $n = \pi r/(\sqrt{2}\ \ell_{\ell 0})$.

To estimate the total amount of creep available, knowledge of the momentum dissipation is also required. The momentum dissipation through damping can easily be obtained by taking time integration over the dissipative force:

$$\Delta P_\alpha = \int f_\alpha dt = \int \underset{\sim}{\vec{D}} \cdot \vec{v} dt = \underset{\sim}{\vec{D}}(\Delta \vec{x})$$

$$= -8M_s rh\,[\pi(\Delta x)/4\mu_b]\,\hat{x} \qquad (27)$$

The momentum dissipation due to coercivity can be obtained similarly as:

$$\Delta P_c = \int f_c dt = \int -8M_s H_c rh\, dt\,\hat{x} \cong 8M_s rh H_c(\Delta t)(-\hat{x})$$

$$\cong -8M_s rh(H_c \Delta x/v)\,\hat{x} \qquad (28)$$

where the radius of the bubble is assumed to be roughly the same throughout the induced motion phase as is the case when short bias field pulses are used for inducing creep. Unlike the damping dissipation, the dissipation due to coercivity depends on the time when the motion takes place instead of the total displacement. The travelling time here is roughly $\Delta x/v$, where v is the average translation velocity during the creep. Since the translation time or velocity is normally drive field dependent, this coercive effect term will vary depending upon the bias field pulse used.

Creep can now be estimated from the conservation of momentum equation,

$$\Delta P_H + \Delta P_g + \Delta P_\alpha + \Delta P_c = 0 \quad , \qquad (29)$$

where $\Delta P_H$ is the external momentum input and is zero for uniform bias field pulsing. Substituting Equations (26), (27) and (28) into Equation (29) gives

$$8M_s rh\left(\frac{r}{\sqrt{2Q}\ \alpha\mu_b} - \frac{\pi\Delta x}{4\mu_b} - \frac{H_c\Delta x}{v}\right) = 0$$

or $$\Delta x = (4r/\sqrt{2Q}\ \alpha\pi)\left[1 + H_c'/(v/\mu_b)\right]^{-1} . \qquad (30)$$

As can be seen, the analytic result agrees with the experimental result in that the creep is proportional to the bubble radius.

The calculated saturation creep for sample 2-16-44 at a bias field of 75 Oe, where the radius is 4.6 μm, is 18.1 μm for bubbles translating at 6 m/sec (saturation velocity) and is 11.6 μm if the translation velocity during the creep is 3 m/sec. If the Gilbert damping constant obtained by matching the translational linear mobility at low gradient drive, $\alpha$ =.078, is used instead of using the resonance damping constant, the saturation creep will be 9.6 μm for a translation velocity of 6m/sec and 7.4 μm for velocity of 3m/sec. The observed saturation creep is 5.5 m, which is a factor of 1.4 to 1.7 and 2 to 3.3 smaller than the theoretical expected value depending on the values used. The effect of coercivity on the amount of creep given in Equation (30) is very similar to what had been observed in Fig. (3.8). Smaller creep was observed when drive was close to the coercive limit and creep reached saturation when a saturation velocity was achieved. But the threshold observed (about 2 Oe) is much too high compared to the coercive force of the sample. This result indicates that an additional threshold for the propagation or annihilation VWT's in the bubble exists.

The observation that the total forward motion of the bubble depends only on the pulsed drive field difference across the bubble radius and the applied pulse width, independent of the bubble size (bias field), can also be understood in terms of the stored momentum. The VWT's describe the form and amount of the momentum being stored. The gyrotropic momentum determines the amount of motion during various phases of the translational motion but has no effect on the total amount of motion since all of the momentum stored during the driven phase will be released in the later phases. No net gyrotropic momentum is stored per cycle of propagation. The total momentum input is the time integration of the Zeeman force:

$$P_H = \int -2\pi M_s hr^2 \vec{\nabla} H_z \, dt = 2\pi M_s hr \Delta H_z \Delta t \quad . \tag{31}$$

This input momentum is proportional to the bubble radius but so is the dissipation due to the damping and the coercive force. With both the input and dissipation a linear function of radius, the total translation is, therefore, independent of the bubble size. The total displacement obtained by equating the input momentum to the dissipative momenta is

$$2\pi M_s hr \Delta H_z \Delta t = 2\pi M_s hr \Delta x/\mu_b + 2\pi M_s rh H_c' \Delta x/v$$

$$\Delta x = \Delta H_z \Delta t/((1/\mu_b) + H_c'/v) \quad , \tag{32}$$

independent of the radius.

## 3.5 Overshoot and Transverse Expansion in the High Impulse Gradient Translation

### 3.5.1 Introduction

The vertical wall twist model leads directly to the question of what happens when the circumference of the bubble is filled with VWT's. Should the velocity increase due to the disappearance of the gyrotropic force if further wall winding is prohibited or should the bubble remain with a saturation velocity? Experiments of this type have never been done because the high field gradient and pulse duration involved requires a very accurate bias compensation and detailed velocity information. Complete removal of the VWT's after translational overshoot is also essential to obtain a consistent initial bubble state.

### 3.5.2 Experiment

Multiple-exposure photographs of the bubble domain on this portion of the experiment were recorded on video tape again using an optical sampling microscope with 10-nsec laser-pulse illumination. A Cohu 4400 silicon intensified target (SIT) TV camera was used. A single laser flash is bright enough to leave an image on the silicon target for 60 msec. Multiple exposure recording was made by triggering the laser several times during the image retention time and superimposing the images on the silicon target. Gradient field pulses as well as the bias compensation pulses were applied in the same way as was described in Section 3.4.2. Bubbles were first

propagated toward the center of the parallel gradient conductors by a sequence of weak gradient field pulses,.6 Oe/radius in magnitude. Two bias field pulses of about 10 Oe in magnitude and .5 to 2 μsec in duration were applied to remove possible wall twist structures. After these priming pulses , bubbles were translated by a single gradient field pulse which was synchronized with the strobing laser flash and a bias compensation pulse. Several bias field pulses, again about 10 Oe in magnitude and .5 to 2 μsec in duration,were applied to induce creep. Bubbles were normally photographed before and during the translation, after the overshoot and after the creep. Bubbles were then brought back to the center of the gradient conductor stripes by the weak gradient field pulses to wait for the next sequence. The silicon intensified target offers an order of magnitude more sensitivity than the Kodak 4X photographic film even with the 3 stop forced development previously used. But, the photographic film is 60 times higher in its resolution element density compared to that of the silicon target. So, in terms of comparable resolution the TV camera has only slightly better sensitivity. The TV recording system offers other advantages, however, such as instant replay. Taking measurements with the Video system is easier than measuring from film, especially with the help of electronic circuitry.

The cycling of the bubble propagation is controlled by a specially designed programmable electronic trigger sequencer. This trigger sequencer control provides a trigger to various pulsers

according to a preprogrammed sequence. This enables cycling of the bubble translation at a rate compatible to the framing rate of the TV recording. The trigger sequencer can now be used for bubble translation only because the translational properties of bubbles had been well characterized from previous work so that a routine sequence of pulses is able to propagate bubble consistently and systematically.

### 3.5.3 Results and Discussion

A typical series of the four exposure photographs showing the bubble at various times during gradient propagation and overshoot is shown in Fig. (3.14). For each sequence, the four exposures, from left to right, are the static bubble before the application of the gradient field pulse, the moving bubble at a specific time after the onset of the gradient field pulse, the static bubble after the overshoot and, finally, the static bubble after the creep. The time of the transient exposure after the onset of the gradient field pulse is indicated in the figure caption. The bias was compensated to within ±.8 Oe during the gradient pulse. A 75 Oe bias field was applied that is 9 Oe above stripe-out and 15 Oe below DC collapse. The details of the overshoot and the creep have been discussed previously, however, the overshoot and the creep exposures are included here as a reference while focusing attention on the transient bubble shape.

Transient shape distortion starts as a triangular deformation in the front of the bubble about 0.4 μsec after the onset of the gradient field pulse, as seen in Fig. (3.14a), and continues through the driven phase, seen at 0.7 μsec, 1.3 μsec and 2 μsec in Figs. (3.14b), (3.14c) and (3.14d), respectively. The deformation also occurs in the rear as it first becomes flat and then, as the driven translation proceeds, the rear wall curves forward. The wall sections at the ends of the two flanks can be seen moving outward and lagging behind the center of the bubble. This transverse expansion of the bubble starts at about .5 μsec at essentially the same time as the shape deformation becomes observable. By the end of the pulse, Fig. (3.14b), the tips of the two flanks have fallen well behind the middle portion of the bubble and the transverse expansion, as well as triangular distortion, are well established. During overshoot, the triangular deformation in the front disappears in less than .5 μsec (Fig. (3.4e)) while the transverse expansion can be seen to continue until at least 6 μsec after the end of the pulse (Fig. (3.14i)). During this phase of the motion, the shape of the bubble looks like a short stripe with the two ends bent slightly toward the rear. Finally the recovery after the transverse expansion proceeds at a much slower rate than the expansion.

The quantitative results of the transverse displacement as well as the related translation are shown in Fig. (3.14). Curve (a) shows the longitudinal displacement, in the down gradient direction, of the bubble center as a function of time. Curve (b) shows the

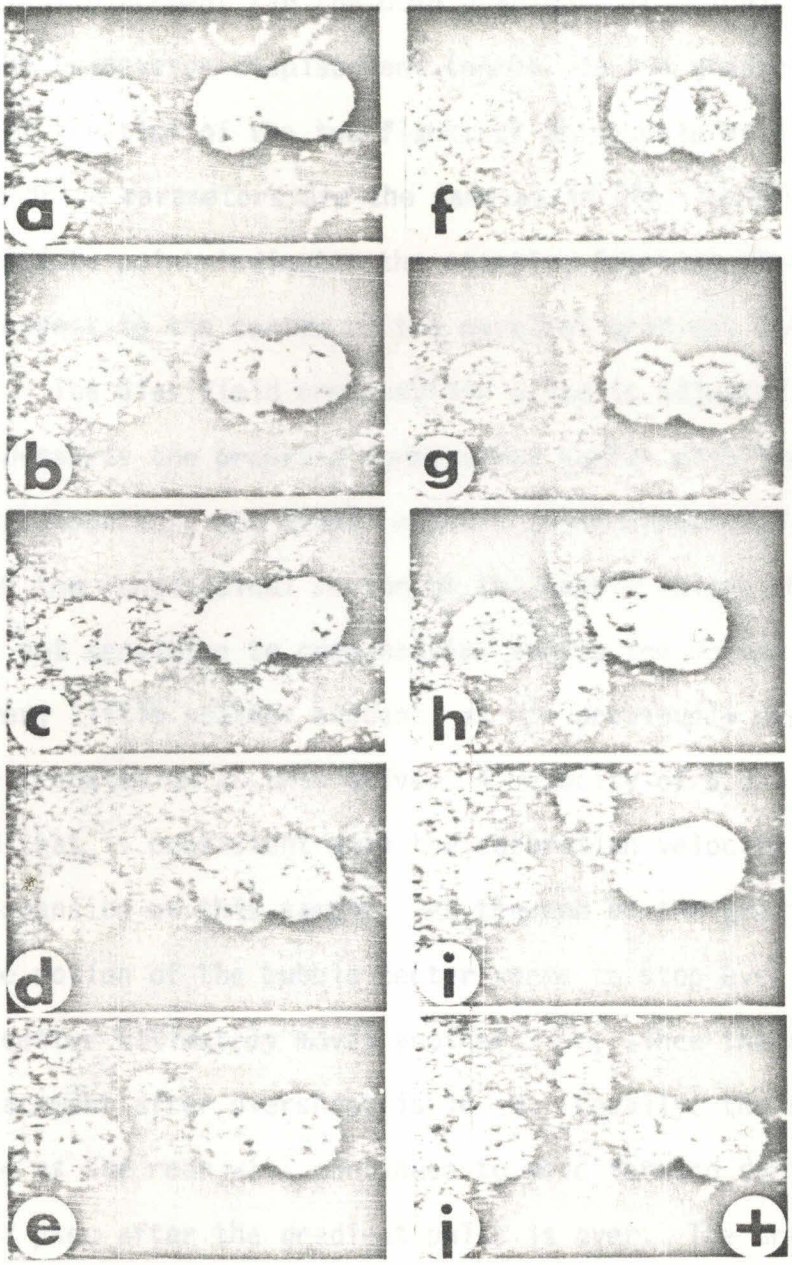


Fig.(3.14) Multiple exposure photographs of the magnetic bubble. First exposure (left most) is the static bubble before the translation; second is the transient bubble shape at (a) 0.4, (b) 0.7, (c) 1.3, (d) 2, (e) 2.6, (f) 3.4, (g) 4.2, (h) 5.5, (i) 8, and (j) 11.3 μsec after the onset of a 7.4 Oe/rad, 2 μsec gradient field pulse; third is the static shape after the end of the translational overshoot; fourth is the static shape after the bias field pulsing. Cross is 4 μm.

longitudinal displacement (in the down gradient direction) and curve (c) the transverse displacement (normal to the gradient direction) of the tips of the two flanks of the bubble as a function of time. The drive parameters are the same as in Fig. (3.14). The number used for the data point indicates the starting location of the translation with respect to the center of the parallel gradient conductors in μm units. The bias field compensation pulse is adjusted so that number 5 represents the properly compensated bubble with lower numbers overcompensated and higher numbers undercompensated. It can be seen that the longitudinal motion of the bubble center (Fig. curve a) is not sensitive to compensation during the driven translation with very little scatter evident, as was previously observed for shorter translation at this drive. A velocity of 5.3 m/sec is observed that is consistent with the saturation velocity measured by radial expansion of this sample. At the end of the gradient pulse, however, the motion of the bubble center seems to stop even though the bubble center ultimately moves another 7 μm, since the average total displacement after overshoot is 16 μm. Locally, the front wall is returning as the rear wall continues to move forward during the first 1 to 2 μsec after the gradient pulse is over. The translation of the bubble center resumes about 8 μsec after the termination of the gradient pulse.

From the observed longitudinal displacement of the bubble flanks (Fig. (3.15) curve b), it can be seen that the flanks lag behind the center, moving at 2.6 m/sec compared to 5.3 m/sec and that their motion

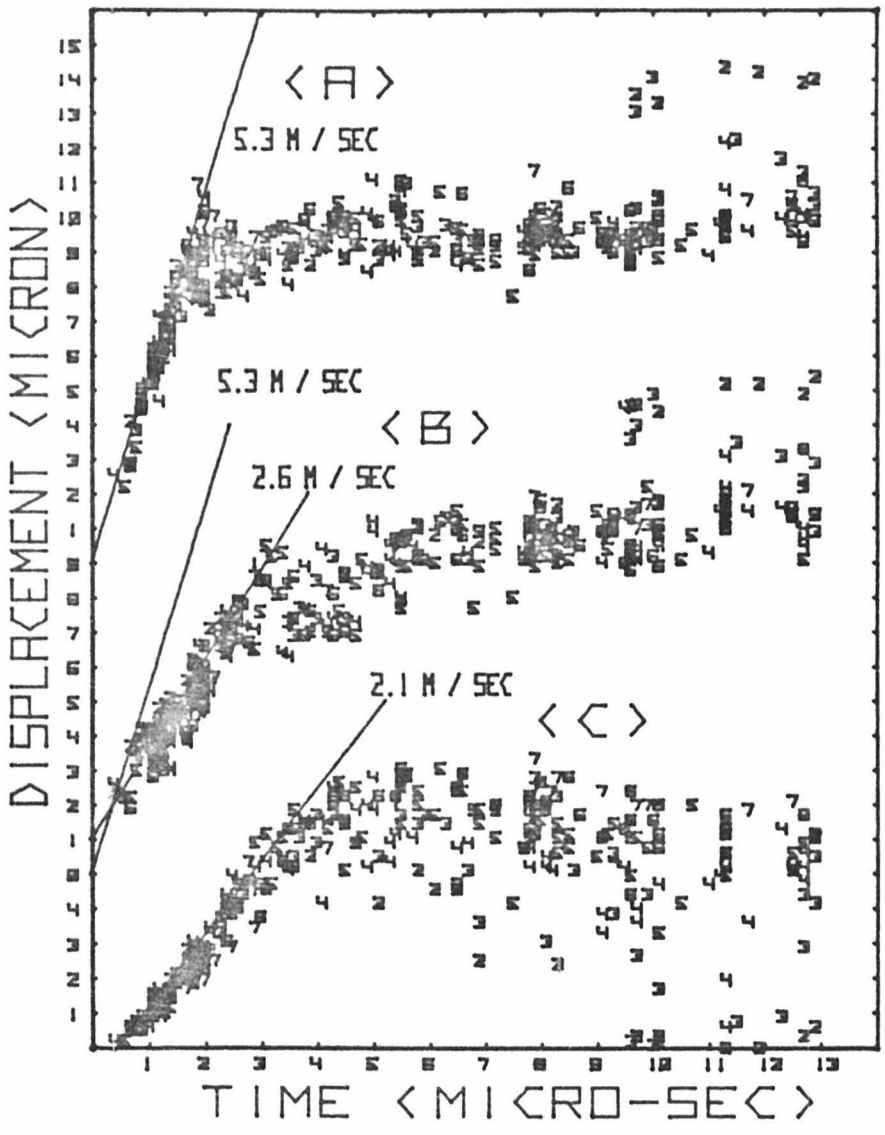


Fig.(3.15) Displacement of (a) average of front and rear bubble wall parallel to the gradient, (b) tip parallel to the gradient, (c) tip normal to the gradient as a function of time after the beginning of a 7.4 Oe/rad, 2 μsec gradient field pulse. Numbers in the curves indicate the degree of compensation with 5 being the properly compensated case; <5 overcompensated; >5 undercompensated.

seems unaffected by the end of the gradient pulse. Transverse expansion can clearly be seen, starting at about .5 μsec after the onset of the gradient field pulse. The flanks expand linearly with respect to time with velocity of 2.1 m/sec and continue after the 2 μsec gradient field pulse with no noticeable change in their expansion rate until reaching the maximum expansion. The recovery rate is much slower with from 4.5 to 16 μsec required for the bubbles to regain their static circular shape. As indicated by the number on the figure, the major factor in the scatter of this recovery is the degree of bias compensation. Overcompensated bubbles (numbers<5) have a smaller maximum transverse expansion and faster recovery rate.

The transverse motion and bubble distortion observed during translation and overshoot can be explained qualitatively by a model involving vertical wall twists, i.e., opposite-winding VBL pairs. It was previously shown (in Section 3.4) that vertical wall twists are a dominant factor in the explanation of creep and overshoot. For bubbles in driven translation, vertical wall twists are continuously generated at the front and rear wall and pushed to the flanks by the g-force, forming a LBL bundle on the left flank and a RBL bundle on the right flank. For long driven translations, these VBL's become overcrowded and seek to find more room by extending the perimeter of the bubble. A rough estimate of the maximum number of VBL's involved in a bundle can be made from the maximum relative oscillatory precession of the azimuthal angle of spins in the front and rear wall

($|\gamma|\Delta H_z t$) with each $\pi$ twist giving a VBL pair. For the present experiment, VBL's would be generated at a rate of 26 VWT's per microsecond at the front and at the rear wall or 52 VBL's/μsec added to the bundle on each flank. Using the equilibrium VBL spacing calculated by Hubert [49], $\ell_\ell = (2)^{\frac{1}{2}} \ell_{\ell o} = 0.5$ μm, a VBL bundle 13 μm long would be on the flank at the time distortion starts (0.5 μsec). This length should be compared to the 15 μm half bubble perimeter for the bubble. At the end of the pulse the bundle would be 52 μm long. The measured half perimeter at this time is 22 μm; of course, such estimates neglect many details but it does show that it is reasonable to have the overcrowded VBL bundles on the flanks become a dominant source for the wall motion during the overshoot.

The vertical wall twist model can account qualitatively for the details of the transient motion seen in Fig. 3.14 and Fig. 3.15. For the bubbles in driven translation, the g-forces tend to compress the cluster of VBL's on the tips of the flanks. The force on these tips increases as more VBL's are generated. As the accumulating g-force becomes comparable to the wall energy per unit circumference, it will push the tip outward and cause the transverse expansion. The low mobility characteristics of the highly compressed VBL bundle will slow the translation velocity of the tips and cause them to lag behind the bubble center. When the gradient pulse is over, the front end, which has few VBL's, is pulled back quickly by wall tension. The tightly-wound VBL's which were trailing behind on the two flanks start to relax to a less compressed, therefore a lower energy struc-

ture. This relaxation results in a forward motion of the VBL's toward the front as well as toward the middle part of the bubble. The forward motion of the VBL's will provide a gyrotropic effective field to continuously expand the two tips outward. The motion of the VBL's toward the middle of the wall will cause the gyrotropic effective field to move the wall forward. Since the transverse expansion of the tips was caused by part of the VBL's moving toward the front, the center of the tight winding section will lag behind the tip and ride on the rear wall. The further travelling of the VBL's to the front of the bubble requires a propagation of the VBL's along the outer edge of the tips which again produces a gyrotropic effective field to expand the tips. As can be seen on Fig. (3.14g), (3.14h) and (3.14i), the size of the two tips are bigger than those in Fig. (3.14f) and (3.14j) which are before and after this mode of motion, respectively. Finally the annihilation of the opposite-sense VBL's in the middle front and back will relieve the overcrowding and allow the stripe to contract back while still providing a motivating source for the translational overshoot, as discussed previously.

The transverse expansion during the overshoot provides direct evidence that only vertical structures are important in bubble overshoot. The total bubble wall length continues to increase during the overshoot so that horizontal structures that might be in the wall would be increasing in length, an impossibility if these same structures are the ones providing the energy necessary to continue the translational motion. It can be clearly concluded that horizontal

structures must play a minor role in the overshoot process.

## 3.6 Bubble Translation in Ion-implanted Garnets

### 3.6.1 Introduction

Ion-implantation in magnetic bubble garnet films has been used to eliminate "hard bubbles. These are bubbles which have abnormal static and dynamic properties[16]. Implantation of $H^+$, $He^+$ or $Ne^+$ with several hundred to a thousand angstroms penetration depth has been used to completely eliminate hard bubbles in garnet materials. The purpose of ion-implantation is to place the crystal in a state of lateral compression. For garnets with negative magnetostriction, this compression induces a planar magnetic anisotropy in the surface layer. Direct observation of magnetic closure domains in the ion-implanted layer associated with magnetic bubbles has been reported by Wolfe, et al [50]. These domains could be seen only on static bubbles since the Bitter pattern method with Ferrofluid was used. The closure domains were found to be very sensitive to the external in-plane magnetic field. The mechanism of hard bubble suppression is not well understood. For a soft bubble, the closure domain reduces the wall energy near the surface of the film and causes an increase in the DC collapse field. Dynamically, the ion-implanted samples show the same saturation velocity as that of the as-grown samples in the radial motion experiment [4]. Less scatter was observed for the ion-implanted sample in the dynamic

bubble collapse experiment,presumably due to the absence of the VBL's in the bubbles. Since the mechanism for overshoot and creep involves VBL's, it is not clear, at the outset, what to expect in the ion-implanted samples.

3.6.2 Samples and Experiment

Two ion-implanted samples are used in this portion of the experiment. The Yttrium-Europium-Thulium sample, number 2-12-63, is the implanted version of the sample 2-16-44 previously investigated. The characteristics of this sample are as follows: $h=6.9$ μm, $4\pi M_s=205$ Gauss, $l=0.93$ μm, $H_{col}=95$ Oe and as measured by microwave resonance, $H_k=3399$ G, $|\gamma|=1.1\times10^7$ rad/sec/Oe, and $\alpha=0.029$. The implantation dosage is $2\times10^{14}$ Ne/cm$^2$ at 80 keV. The other implanted sample is a Calcium-Germanium sample, sample 206, which is a high mobility sample with the material characteristics as follows: $h = 4.1$ μm, $4\pi M_s = 180$ Gauss, $\ell = .77$ μm, $H_{col} = 72.7$ Oe, $H_k=1520$ G, $|\gamma|=1.83\times10^7$ rad/sec/Oe, and $\alpha=0.14$. Both samples show the static suppression of hard bubbles. The experiment that was done is similar to that with the as-grown samples in the previous two sections.

3.6.3 Results and Discussion

Ion-implantation greatly changes the translational character of bubbles. The bubbles seem less erratic in translation and exhibit little overshoot and no observable creep. Multiple exposure photographs of bubbles in the ion-implanted sample 2-12-63 are shown in Fig. (3.16). An exposure is taken of the initial position of the bubble (lower most in the photograph) and again after a 2.25-Oe/

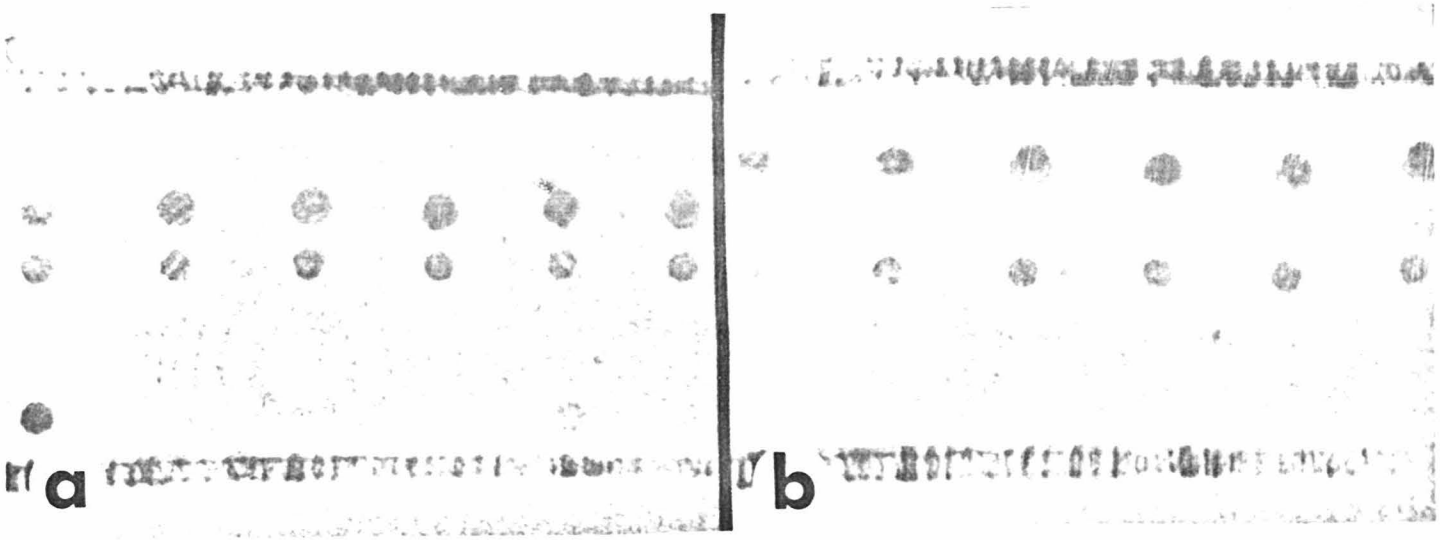




Fig.(3.16) Multiple exposure photographs of bubble translation in the ion-implanted sample. Bubbles are exposed before the translation (in the center of the conductor pair), at the end of a 2.25 Oe/Radius, (a) 3 μsec and (b) 6 μsec long gradient field pulse and after its overshoot. No noticeable creep could be observed in this ion-implanted sample.

radius (a) 3-μsec or (b) 6-μsec gradient field pulse. Finally, an exposure was taken of the bubble long after (60 msec) the end of the gradient field pulse. It can be seen that all bubbles move very uniformly. At the end of the pulse, they are elliptical. At this drive, overshoot is hardly observable. For quantitative measurements, single exposures were used as well as wide (10 diameter) bubble spacing.

Total displacement as a function of the pulse field gradient amplitude for sample 2-12-63 is shown in Fig. (3.17). The gradient pulse width is 1 μsec and the bias field is 85 Oe. These conditions are the same as for the as-grown sample. It can be seen that the driven displacement increases rapidly up to about 5 Oe/radius, then more slowly. Velocity in high drive agrees moderately well with the radial expansion saturation velocity value of 5.6 m/sec. It can be seen that overshoot increases rapidly in much the same way as the as-grown sample 2-16-44 (Fig. (3.9a)). A peak in overshoot is clearly observed. It increases to about 3 μm when the drive is up to 4.5 Oe/radius and reduces rapidly when the drive increases further. There is no observable creep. Three implanted samples with dosage sufficient to suppress most of the hard bubbles all show overshoot after the application of the gradient pulse, but expand symmetrically during the bias field pulsing and fail to show creep.

Displacement as a function of gradient pulse magnitude for the ion-implanted sample 206 is shown in Fig. (3.18a). The symbol (+)

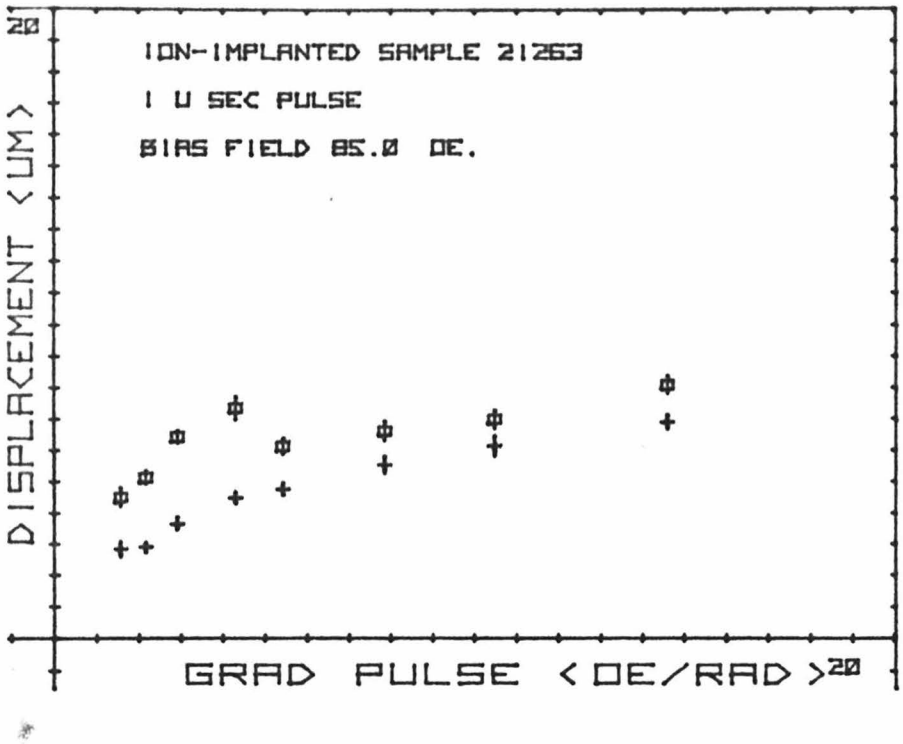


Fig.(3.17) (a) Bubble displacements at the end of a 1 μsec long gradient field pulse (+) and after its overshoot (□) as a function of the gradient field strength for the ion-implanted sample with 85 Oe DC bias field.

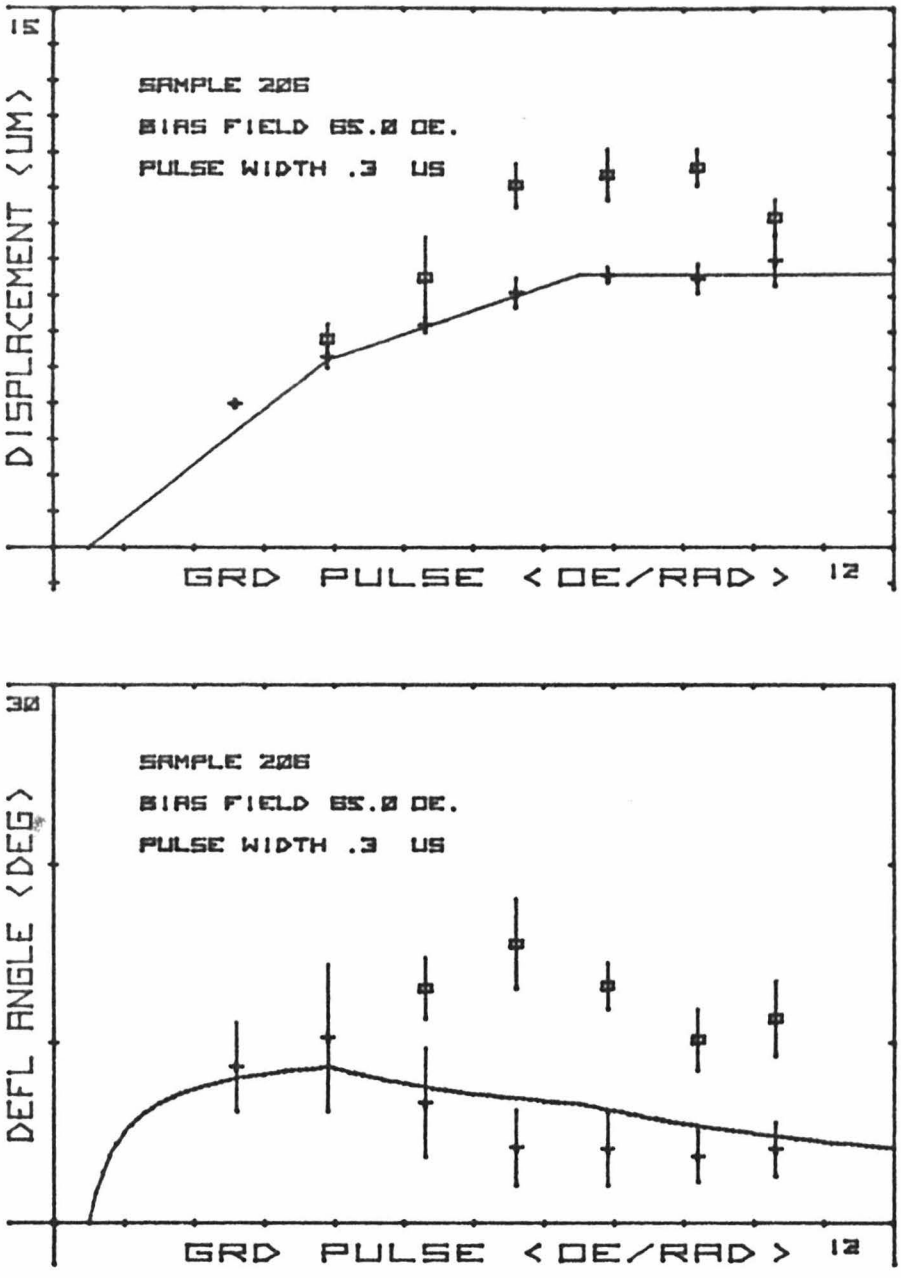


Fig.(3.18) (a) Bubble displacement at the end of a .3 μsec gradient field pulse (+) and after its overshoot (□) for ion-implanted sample 206. (b) Bubble deflection angle during driven translation (+) and overshoot (□).

denotes the displacement at the end of the gradient pulse and (□) denotes the displacement after the end of the overshoot. Compared to the previous results for sample 2-12-63, the linear mobility here is about half while the saturation velocity of 25 m/sec is 4 times higher. Again, the sample shows a peak in overshoot and no noticeable creep.

The angle of the unichiral bubble in translation is investigated here. Sample 2-16-44 and ion-implanted sample 2-12-63 previously used have small deflection angles and are not appropriate for this type of study. The ion-implanted sample 206 has a normal deflection angle in the range from 10 to 14 degrees depending on the bias field used. All bubbles in this sample deflect at the same angle without the presence of the inplane field. Presumably, all bubbles are unichiral bubbles.

The deflection angle of the bubbles in sample 206 as a function of gradient pulse magnitude is shown in Fig. (3.18b). The average angle during the driven translation is denoted by (+) and the average angle between the overshoot direction and the driven translation is denoted by (□). Comparing Fig. (3.18a) and (b), it can be seen that during the driven phase, the deflection angle decreases as the gradient field magnitude increases after the overshoot becomes apparent. During the overshoot phase, bubbles are found to deflect with an angle of between 9 to 17 degrees relative to the driven translation direction.

The theoretical deflection angle for drive fields below the over-

shoot generation threshold has been discussed in Section 3.1.3. The deflection angle will be small when the drive field is close to coercive force limit. As the drive field increases so that $V/\mu_b$ becomes much larger than the coercive force, the deflection angle will increase and converge to a value dependent on the wall mobility. Above the threshold for overshoot, an additional gyrotropic force, $F_g'$, due to VWT generation and deflection, should be considered. This added g-force for the VBL pairs will be in the direction to oppose the translation or the external drive force or will be in between these two directions, depending upon the details of the formation and the ~~motion~~ motion of the opposite-winding VBL's. The average $F_g'$ should be along the symmetry axis of the VBL pairs since that is the direction where a net momentum is being stored. The force diagram for the case where the symmetry axis is along the velocity direction is shown in Figure (3.19a). The gyrotropic force for VWT's is in the same direction as the damping and coercive forces. The force component normal to the translation direction remains the same as that in Section 3.1.3. Equation (18) can then be applicable here, i.e.,

$$\theta = \sin^{-1}(F_g/F_H) = \sin^{-1}(4\pi M_s hV/|\gamma|)/(2\pi M_s hr \cdot r\nabla H))$$

$$= \sin^{-1}(2V/|\gamma| r\Delta H) \quad . \qquad (33)$$

If the symmetry axis of the VWT's is along the field gradient direction, the force $F_g'$ will be colinear to the external drive force, as shown in Fig. (3.19b). The deflection angle can be determined by $F_g$, $F_\alpha$, and $F_c$ alone. This deflection angle is obtained using

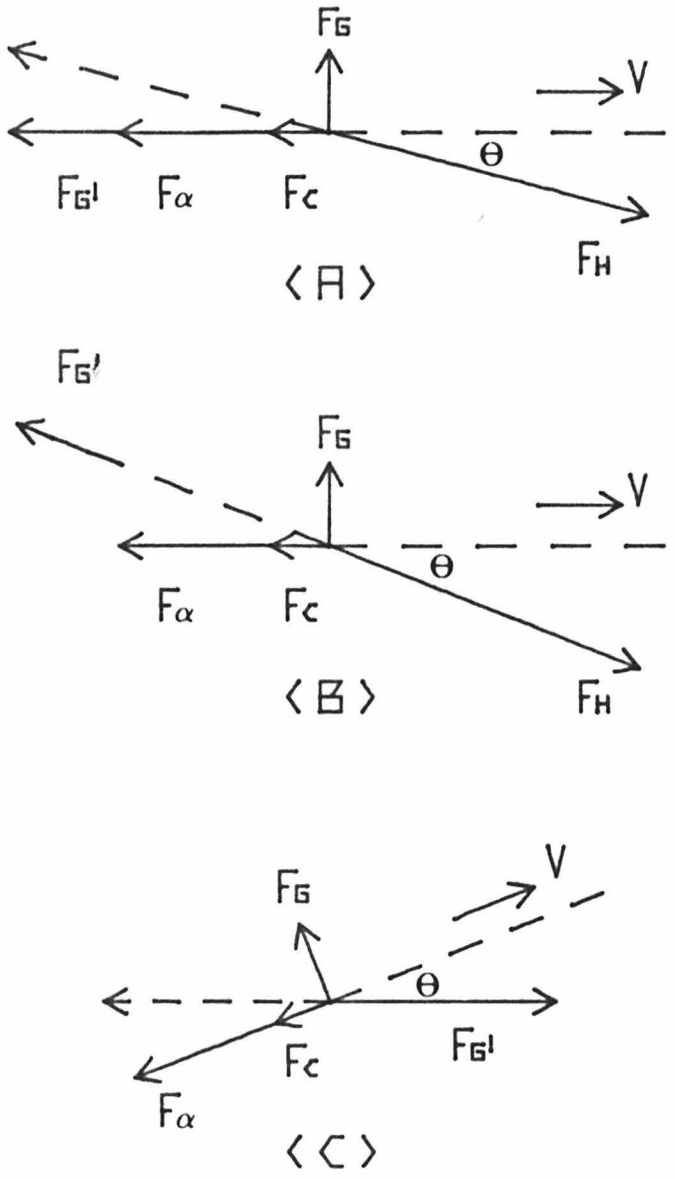


Fig. 3.19 Force diagrams for bubble in driven translation (a) and (b) and overshoot (c) with the symmetry axis of VWT's along the driven translation direction (a) and (c) and along field gradient direction (b).

Equations (4), (7), (10) and (16) as

$$\theta = \tan^{-1}(F_g/(F_\alpha + F_c)) = \tan^{-1}((2V/|\gamma|)/(V/\mu_b + H_c'))$$

$$= \tan^{-1}((2\mu_b/|\gamma|)/(1+(H_c'\mu_b/V)) \quad . \qquad (34)$$

The deflection angle in this case will remain constant with respect to the increasing drive if the translation velocity does not change with drive or if the ratio $V/\mu_b$ is much larger than $H_c'$.

The calculated driven translation angle using Equation (33) is shown as the solid curve in Fig. (3.18b). The velocity values used in this calculation are indicated by the solid curve in Fig. (3.18a). The observed angles are in good agreement with the case where the symmetry VWT axis is along the velocity direction. This result is also consistent with the earlier transient expansion shape observation given in Section 3.3.2, Fig. (3.4).

The enhancement in the deflection angle during the overshoot phase can be understood based on the same assumption that the symmetry axis of the VWT's is along the driven translation direction. The unwinding of the VWT during the overshoot phase results in a self-driving force along the symmetry axis. The bubble should again deflect when translated by this force. The force diagram for this case is shown in Fig. (3.19c). This enhancement in the deflection angle is expected to be about the same as that of the driven translation angle for a drive field below the overshoot threshold, since there will not be any new VWT generation to reduce the deflection angle.

The ion-implanted sample characteristics are consistent with the view that the dominant wall structure is vertical wall twists. Creep is absent in the implanted samples, as expected from the observation that VBL's are not stable statically in the ion-implanted materials. It must be true that all the complexities in the wall are removed before the bubble reaches a full stop from its translational motion. The threshold in drive for the overshoot, the amount of the driven translation, and the total translation per pulse in the low drive region (4 Oe/radius) for the implanted sample 2-12-63 are very similar to those observed in the as-grown sample 2-16-44. The mechanism for overshoot in the low drive region must be similar for the two samples. The transverse expansion during the translation of the bubbles in the implanted sample, as shown in Fig. (3.15b), is consistent with the model that VWT's are being generated as in the as-grown sample. The peak in overshoot at a drive of 4 Oe/radius, and the reduction in overshoot with the increasing drive suggests a breakdown of the initial overshoot structure due to the existence of the ion-implanted capping layer. The breakdown mechanism is not well understood. It probably relates to the conversion mechanism recently reported by Beauliew et al [51], where Bloch-point injection was associated with the static switching of the implanted capping layer. Bloch point injection results in Bloch-line annihilation that removes "stored" momentum without causing translation. The dynamic threshold observed here is compatible with cap switching. At high drive, then, the VBL's are continuously lost during the driven translation,

limiting the overshoot to a small but constant magnitude. Details of these processes need further investigation.

## 3.7 Conclusion

High speed sampling microscopy provides a new way of investigating the structure of walls. Vertical wall twists, undetected by skew angle propagation, can be detected by observing the transient shape of the bubble after the bias field change. Generation of vertical wall twists has been shown to occur when bubbles are translated by a gradient drive field above a threshold.

Induced bubble translation, creep, has been observed, characterized, and related to the overshoot. Overshoot and creep are bubble size, or DC bias field, dependent. They are complementary to each other. Characterization of the various phases of the gradient translation provides enough knowledge to perform the sampling experiment on the bubble translation. Detailed overshoot investigations reveal the transverse expansion which prolongs the overshoot phase and enhances the scatter. This occurrence of the transverse expansion excludes the possibility of the stacking of both horizontal Bloch curves and Bloch rings.

All the observed motions are explained qualitatively on the basis of a vertical wall twist model. During the driven translation phase, momentum is stored in the form of vertical wall twist structures. The spontaneous unwinding of these wall twist structures, after the gradient pulse is over, causes overshoot. The induced annihilation of the remnant structure by the bias field pulsing causes creep.

The momentum does not seem to be conserved in the ion-implanted samples, suggesting the presence of a more complicated Bloch line annihilation mechanism.

## References


1.1 A. H. Bobeck, Bell Sys. Tech. J. 46, 1901 (1967).

1.2 A. H. Bobeck and H. E. D. Scovil, Scientific American 224, 78 (June, 1971).

1.3 A. H. Bobeck, P. I. Bonyhard, and J. E. Geusic, Proc. IEEE 63, 1176 (1975).

1.4 D. A. Hodges, Scientific American 237, 130 (September, 1977).

1.5 A. J. Perneski, IEEE Trans. MAG-5, 554 (1969).

1.6 I. Danylchuk. J. of Appl. Phys. 42, 1358 (1971).

1.7 A. H. Bobeck, R. F. Fisher and J. L. Smith, AIP Conf. Proc. 5, 45 (1971).

1.8 P. I. Bonyhard and J. L. Smith, IEEE Trans. MAG-12, 614 (1976).

1.9 W. Strauss, Proc. IEEE 58, 1386 (1960).

1.10 Hsu Chang, J. Fox, D. Lu, and L. L. Rosier, IEEE Trans. MAG-8, 2.4 (1972).

1.11 J. L. Archer, Digest of Intermag Conf., 11-1 (1977).

1.12 R. Frommer, K. Hirabayashi, S. Kohyama, and I. Nojima, ISSCC, 116 (1977).

1.13 U. F. Gianola, D. H. Smith, A. A. Thiele and L. G. van Uitert, IEEE Trans. MAG-5, 558 (1969).

1.14 A. A. Thiele, Bell Sys. Tech. J. 48, 3287 (1969).

1.15 A. A. Thiele, J. Appl. Phys. 41, 1139 (1970).

1.16 L. K. Shick, J. W. Nielsen, A. H. Bobeck, A. J. Kurzig, P. C. Michaelis, and J. P. Reekstin, Appl. Phys. Lett. 18, 89 (1971).

1.17 P. Chaudhari, J. J. Cuomo, and R. J. Gambino, IBM J. Res. and Develop. 17, 66 (1973).

1.18 M. H. Kryder, K. Y. Ahn, and J. V. Power, IEEE Trans. MAG-11, 1145 (1975).

1.19 C. H. Bajorek and R. J. Kobliska, IBM J. Res. and Develop. 20, 271 (1976).

1.20 P. Weiss, J. Phys. 6, 661 (1907).

1.21 H. Callen and R. M. Josephs, J. Appl. Phys. 42, 1977 (1971).

1.22 D. C. Fowlis and J. A. Copeland, AIP Conf. Proc. 5, 241 (1971).

1.23 T. W. Collins, J. Gazdag, and K. Ju, IEEE Trans. MAG-11, 1088 (1975).

1.24 N. L. Shryer and L. R. Walker, J. Appl. Phys. 45, 5406 (1974).

1.25 A. P. Malozemoff, Appl. Phys. Lett. 21, 190 (1972).

1.26 G. P. Vella-Coleiro, A. Rosencweig and W. J. Tabor, Phys. Rev. Lett. 29, 949 (1972).

1.27 J. C. Slonczewski, A. P. Malozemoff, and O. Voegeli, AIP Conf. Proc. 10 pt. 1, 458 (1973).

2.1 C. Kittel, Intro. to Solid State Phys., 2nd Edition (1956).

2.2 L. Landau and E. Lifshitz, Physik z. Sowjet Union 8, 153 (1935).

2.3 T. L. Gilbert, Phys. Rev. 100, 1243 (1955).

2.4 W. F. Brown, Jr., Micromagnetics, Interscience Pub., (1963).

2.5 J. C. Slonczewski, Int. J. Magn 2, 85 (1972).

2.6 J. A. Cape, W. F. Hall, and G. W. Lehman, J. Appl. Phys. 45, 3572 (1974).

2.7 A. A. Thiele, Phys. Rev. Lett. 30, 230 (1973).

2.8 A. A. Thiele, J. Appl. Phys. 45, 377 (1974).

2.9 H. Goldstein, Classical Mechanics, Addison-Wesley (1950).

2.10 A. P. Malozemoff and J. C. Slonczewski, IEEE Trans. MAG-11, 1091 (1975).

2.11 A. A. Thiele, J. Appl. Phys. 47, 2759 (1976).

2.12 A. P. Malozemoff and J. C. Slonczewski, AIP Conf. Proc. 24, 603 (1974).

3.1 G. P. Vella-Coleiro and W. J. Tabor, Appl. Phys. Lett. 21, 7 (1972).

3.2 A. H. Bobeck, I. Danylchuk, J. P. Remeika, L. G. Van Uitert and E. M. Walters, Proc. 1970 International Conf. on Ferrite, Kyoto.

3.3 H. Callen and R. M. Josephs, J. Appl. Phys. 42, 1977(1971).

3.4 G. J. Zimmer, L. Gal, K. Vural, and F. B. Humphrey, J. Appl. Phys. 46, 4976 (1975).

3.5 G. J. Zimmer, L. Gal, and F. B. Humphrey, J. Appl. Phys. 48, 362 (1977).

3.6 A. P. Malozemoff and J. C. Deluca, Appl. Phys. Lett. 26, 719 (1975).

3.7 J. A. Cape, J. Appl. Phys. 43, 3551 (1972).

3.8 G. P. Vella-Coleiro, F. B. Hagedorn, Y. S. Chen, and S. L. Blank, Appl. Phys. Lett. 22, 324 (1973).

3.9 F. H. de Leeuw and J. M. Robertson, J. Appl. Phys. 46, 3182 (1975).

3.10 G. P. Vella-Coleiro, A. Rosencweig and W. J. Tabor, Phys. Rev. Lett. 29, 949 (1972).

3.11 J. C. Slonczewski, Phys. Rev. Lett. 29, 1679 (1972).

3.12 J. C. Slonczewski, A. P. Malozemoff and O. Voegeli, AIP Conf. Proc. 10, 458 (1973).

3.13 A. A. Thiele, Phys. Rev. Lett. 30, 230 (1973).

3.14 A. A. Thiele, J. Appl. Phys. 45, 377 (1974).

3.15 R. Suzuki, M. Takahashi, T. Kobayashi, and Y. Sugita, Appl. Phys. Lett. 26, 342 (1975).

3.16 R. Wolfe and J. C. North, Bell Sys. Tech. J. 51, 1436 (1972).

3.17 O. Voegeli, B. A. Calhoun, L. L. Rosier and J. C. Slonczewski, AIP Conf. Proc. 24, 617 (1974).

3.18 T. L. Hsu, AIP Conf. Proc. 24, 624 (1974).

3.19 H. L. Hu, T. J. Beaulieu, D. W. Chapman, D. M. Franich, G. R. Henry, L. L. Rosier, and L. F. Shew, 23rd MMM Conf., 3A-1 (1977).

3.20 A. A. Thiele, A. H. Bobeck, E. Della Torre and U. F. Gianola, Bell Syst. Tech. J. 50, 711 (1971).

3.21 J. K. Galt, Phys. Rev. 85, 664 (1952).

3.22 J. A. Baldwin and F. Milstein, J. Appl. Phys. 45, 4007 (1974).

3.23 G. P. Vella-Coleiro, AIP Conf. Proc. 24, 595 (1974)

3.24 G. P. Vella-Coleiro, AIP Conf. Proc. 18, 217 (1973).

3.25 R. M. Josephs, Appl. Phys. Lett. 25, 244 (1974).

3.26 G. P. Vella-Coleiro, F. B. Hagedorn and S. L. Blank, Appl. Phys. Lett. 26, 69 (1975).

3.27 A. P. Malozemoff, J. Appl. Phys. 44, 5080 (1973).

3.28 R. M. Josephs and B. F. Stein, AIP Conf. Proc. 24, 598 (1974).

3.29 L. L. Rosier, D. M. Hannon, H. L. Hu, L. F. Shew, and O. Voegeli, AIP Conf. Proc. 24, 620 (1974).

3.30 A. P. Malozemoff and J. C. Deluca, Appl. Phys. Lett. 26, 719 (1975).

3.31 A. P. Malozemoff and J. C. Slonczewski, IEEE Trans. MAG-11, 1091 (1975).

3.32 G. P. Vella-Coleiro, J. Appl. Phys. 47, 3287 (1976).

3.33 G. P. Vella-Coleiro, Appl. Phys. Lett. 28, 743 (1976).

3.34 G. J. Zimmer, L. Gal, and F. B. Humphrey, AIP Conf. Proc. 29, 85 (1976).

3.35 F. C. Rossol, IEEE Trans. MAG-7, 142 (1971).

3.36 F. C. Rossol, J. Appl. Phys. 40, 1082 (1969).

3.37 G. P. Vella-Coleiro and T. J. Nelson, Appl. Phys. Lett. 24, 387 (1974).

3.38 T. M. Morris and A. P. Malozemoff, AIP Conf. Proc. 18, 242 (1974).

3.39 G. J. Zimmer, T. M. Morris, K. Vural and F. B. Humphrey, Appl. Phys. Lett. 25, 750 (1974).

3.40 F. B. Humphrey, IEEE Trans. MAG-11, 1679 (1975).

3.41 T. M. Morris, G. J. Zimmer and F. B. Humphrey, J. Appl. Phys. 47, 721 (1976).

3.42 P. J. Grundy, D. C. Hothersall, G. A. Jones, B. K. Middleton and R. S. Tebble, Phys. Status Solidi, A9, 79 (1972).

3.43 P. J. Grundy, G. A. Jones, and R. S. Tebble, AIP Conf. Proc. 24, 541 (1974).

3.44 R. W. Patterson, A. I. Braginski, and F. B. Humphrey, IEEE Trans. Mag-11, 1094 (1975).

3.45 A. P. Malozemoff, J. C. Slonczewski and J. C. Deluca, AIP Conf. Proc. 29, 58 (1975).

3.46 N. L. Shryer and L. R. Walker, J. Appl. Phys. 45, 5406 (1974).

3.47 F. B. Hagedorn, J. Appl. Phys. 45, 3129 (1974).

3.48 J. C. Slonczewski, J. Appl. Phys. 44, 1759 (1973).

3.49 A. Hubert, AIP Conf. Proc. 18, 178 (1973).

3.50 R. Wolfe, and J. C. North, Appl. Phys. Lett. 25, 122 (1974).

3.51 T. J. Beaulieu, B. R. Brown, B. A. Calhoun, T. Hsu and A. P. Malozemoff, AIP Conf. Proc. 34, 138 (1976).